BuMines OFR 53-86

PB86-209483

A mining research contract report
OCTOBER 1985

5

DUAL WAVELENGTH LIGHT SOURCES

Contract H0123031
Bethlehem Steel Corporation

Bureau of Mines Open File Report 53-86

BUREAU OF MINES
UNITED STATES DEPARTMENT OF THE INTERIOR

50272-101

REPORT DOCUMENTATION PAGE

1. REPORT NO. BuMines OFR 53-86

2.

3. Recipient's Accession No. PB86 209483/AS

4. Title and Subtitle
Dual Wavelength Light Sources

5. Report Date
Oct. 1985

6.

7. Author(s)
R. T. Boos, W. D. Egan, R. A. Elliott, and R. K. DeFreeze

8. Performing Organization Rept. No.

9. Performing Organization Name and Address
Bethlehem Steel Corp.
Research Department
Bethlehem, PA 18016

10. Project/Task/Work Unit No.
OAK-61-81063

11. Contract(C) or Grant(G) No.
(C)
(G) H0123031

12. Sponsoring Organization Name and Address
Office of Assistant Director--Mining Research
Bureau of Mines
U.S. Department of the Interior
Washington, DC 20241

13. Type of Report & Period Covered
Contract research,
Oct. 1982--Oct. 1985

14.

15. Supplementary Notes

Approved for release June 6, 1986.

16. Abstract (Limit: 200 words)

This report describes work done to develop a tunable, room-temperature diode laser source for a remote coal mine methanometer. A detailed evaluation showed that a broad area InGaAs/InP injection laser operating at approximately 1,650 nm could be suitable for a differential absorption light detection and ranging measurement of methane if the spectral bandwidth could be reduced by a factor of approximately 400. Consequently, an external grating cavity was designed and fabricated to reduce the bandwidth of the injection lasers. The optical design of an off-axis parabolic mirror grating cavity was developed using geometric optics to determine the physical parameters for the external cavity that would produce the desired spectral bandwidth of 0.2 cm^{-1}. The fabrication of this external resonator source is described, and its performance against the design criteria is evaluated. Apart from a smaller than desired methane absorption coefficient, the device met all design specifications. The low methane absorption coefficient was attributed to a larger than desired source linewidth, which was measured to be two to three times larger than the design value. An explanation of this excessive bandwidth based on coupled mode theory is presented. The unsatisfactory methane absorption coefficient of the external cavity diode laser source significantly detracts from its suitability for use in an instrument to remotely measure methane in coal mines.

17. Document Analysis a. Descriptors

Mining research

Methane	Remote sensing	Light sources
Coal mines	Infrared radiation	Injection lasers
Optical radar	Absorption spectra	Indium gallium arsenide lasers

b. Identifiers/Open-Ended Terms Mie scattering

c. COSATI Field/Group

18. Availability Statement

Release unlimited by NTIS.

19. Security Class (This Report) Unclassified

20. Security Class (This Page) Unclassified

21. No. of Pages 162

22. Price

(See ANSI-Z39.18)

See Instructions on Reverse

OPTIONAL FORM 272 (4-77)
(Formerly NTIS-35)
Department of Commerce

FOREWORD

This report was prepared by Bethlehem Steel Corporation, Research Department, Bethlehem, PA under USBM Contract number H0123031. The contract was initiated under the Mining Research Program. It was administered under the technical direction of the Pittsburgh Research Center with Charles D. Litton acting as Technical Project Officer. Oliver H. Snyder III was the contract administrator for the Bureau of Mines. This report is a summary of the work recently completed as a part of this contract during the period October 1982 to October 1985. This report was submitted by the authors in October 1985.

This report does not contain any patentable features.

Table of Contents

ABSTRACT 5

INTRODUCTION 7

LIDAR TECHNIQUES FOR REMOTE DETECTION OF GASEOUS CHEMICAL SPECIES 10

SPECTROSCOPIC CONSIDERATIONS 18

SOME CHARACTERISTICS OF 1.65 MICRON WAVELENGTH INJECTION LASERS 28

REQUIREMENTS OF A DIODE LASER DIAL METHANOMETER FOR COAL MINES 41

OPTICAL DESIGN OF A DUAL DIODE LASER SOURCE 51

AN OFF-AXIS PARABOLIC MIRROR EXTERNAL GRATING CAVITY DUAL DIODE LASER SOURCE 66

PERFORMANCE TESTS 96

CONCLUSION AND RECOMMENDATIONS 102

REFERENCES 108

APPENDIX A 130

APPENDIX B 135

APPENDIX C 137

APPENDIX D 140

APPENDIX E 146

Color Illustrations Reproduced
In Black and White

APPENDIX F 153

ABSTRACT

DUAL WAVELENGTH LIGHT SOURCES

This is a report on research directed toward the development of a coal mine methanometer. The project encompassed two tasks. The first was a study conducted to determine if room-temperature injection lasers could be used as the source for a DIAL methanometer for coal mine applications. As part of that study, prior DIAL measurements of methane were reviewed and the measurement technique explored in general. The absorption spectroscopy of methane was then examined in detail and found to contain an appropriate absorption feature near a wavelength of 1.65 μm provided the spectral width of the light source was approximately 0.2 cm^{-1}. The operating characteristics of broad area high optical output InGaAs/InP injection lasers were examined and a detailed calculation of the requirements for a diode laser DIAL measurement of methane in a coal mine was performed. By comparing the observed diode laser properties with the DIAL requirements, it was found that broad area InGaAs/InP injection lasers were suitable in most respects for coal methane measurements. The exception was the diode laser spectral bandwidth. It was found to be some 400 times too large.

The second task was the design and fabrication of an external grating cavity to reduce the bandwidth of the injection lasers. The optical design of an off-axis parabolic mirror grating cavity was developed using geometric optics to determine the physical parameters for the external cavity which would produce the desired spec-

tral bandwidth of 0.2 cm^{-1}. The fabrication of this external resonator source is described and its performance against the design criteria evaluated. Apart from a smaller than desired methane absorption coefficient the device met all design specifications. The effect of the reduced methane absorption coefficient is to increase the time required to make an accurate methane concentration measurement. The low methane absorption coefficient was attributed to a larger than desired source linewidth which was measured to be two to three times larger than the design value. An explanation of this excessive bandwidth based on coupled mode theory is presented. In summary, an external grating cavity for dual diode lasers was designed, assembled, and tested. It met all design goals for a DIAL coal mine methanometer apart from a too low methane absorption coefficient. This deficiency significantly detracts from its suitability for use in an instrument to remotely measure methane in coal mines.

1. INTRODUCTION

The presence of noxious and explosive gases in underground mine atmospheres has always posed a serious threat to the well-being of miners. Increases in mining mechanization, particularly since World War II, have enlarged the gas burden facing miners[1]. In the United States, this increased burden has stimulated federal mine-safety legislation[2]. These regulations imposed by legislative action have in turn reduced the productivity gained through mechanization.

Nearly two-thirds of all underground U.S. coal tonnage is extracted using continuous mining machines in room-and-pillar mining operations[1]. As a result of the Mine and Safety act of 1969[2] and various state laws, present practice in the room-and-pillar mine is to stop mining every twenty minutes to measure the concentration of methane gas at one foot from the working face. After the mining machine is withdrawn, temporary roof supports are installed to the working face so that a miner can approach the face and measure the methane concentration with a hand-held catalytic combustion methane detector and/or flame safety lamp[3,4]. When the measurement is completed, the temporary roof supports are removed and the mining machine begins mining again[5,6]. Obviously, this procedure reduces productivity and is in itself a safety hazard as temporary roof supports can well be dangerous.

It has been estimated that full utilization of **remote** methane measurements could provide up to a 5 percent improvement in room-and-pillar coal mining productivity[7]. Such a productivity increase would represent about 11,000,000 tons of coal annually in the U.S. alone[1]. The ability to make remote methane measurements would also be useful in other underground mines, such as in salt mines.

The need for a remote measurement of methane concentration at the working face of an underground coal mine was identified at Bethlehem Steel Corporation in the spring of 1977. Specifications for a methane measurement instrument were drawn up in 1978 at Bethlehem Steel Corporation's Homer Research Laboratories (HRL), and evaluation of remote gas sensing techniques was begun. That evaluation process included initiating a study of the potential use of LIDAR (light detection and ranging) methods at Stanford University. That 1978 study[8] concluded that remote methane detection could be achieved by differential absorption LIDAR (DIAL) techniques. At that time Raman-shifted neodymium glass, Raman-shifted Nd:YAG, and Erbium doped YAG (Er:YAG) were all considered as potentially feasible sources for the stated task. Er:YAG was selected as the simplest of these for experimental work, which was then carried out at HRL in the summer of 1979.

The work at HRL in 1979 demonstrated that methane could be remotely detected and measured in a laboratory, using the DIAL technique, an Er:YAG source, and Mie retroreflection from coal dust[7]. However, the Er:YAG laser is inherently a device of low conversion efficiency, with a theoretical upper efficiency limit of only a few percent[9]. Moreover, a flash lamp driven device (such as the Er:YAG laser used at HRL in 1979) requires high voltages and driving currents. Redesign to satisfy the Federal Code[10] in terms of safety hazards would clearly be difficult.

Fortunately, a different kind of laser source for a wavelength compatible with methane absorption (1.65 μm) became realizable at about the time the 1979 HRL study was completed. This alternative is a sophisticated form of semiconductor injection diode laser. Room-temperature injection diode lasers for the "long-wavelength" region from 1 μm to 1.7 μm have been reported only during the last few years[11-17]. Thus a study[18] was initiated by Bethlehem Steel Corporation at the Oregon Graduate Center (OGC) at the end of 1980 to determine the feasibility of using an injection laser as the source in a portable methanometer.

During that 9 month study, it was found that $In_{0.53}Ga_{0.47}As$ diode lasers could indeed be suitable as a methanometer source if their spectral output could be modified to match the requirements of a DIAL measurement. The study indicated the proper modification could be realized by mounting the semiconductor laser in an external diffraction grating tuned cavity and design parameters for such a cavity were specified. This report reviews the requirements for DIAL measurement of methane , describes the diode laser operating characteristics, optical design of the external cavity, implementation of the design, and performance testing of the dual wavelength light source.

First, fluorescence, Raman backscatter and differential absorption LIDAR techniques for remote detection of gaseous species are reviewed in Section 2 where it is argued that a DIAL system is best suited to the problem at hand. This is followed by a discussion of the spectroscopy of methane and other constituents of the coal mine atmosphere in Section 3 in order to determine the spectral region which is best suited for a diode laser based DIAL system. The characteristics of diode lasers emitting near 1.65 μm are reviewed in Section 4. The requirements that a diode laser based methanometer must meet, such as eye safety standards and accuracy, are discussed in Section 5. The optical design of a dual diode laser source to meet the spectral requirements discussed in Section 3 is outlined in Section 6. Section 7 is a description of the dual wavelength source which was ultimately constructed and its operating characteristics. The performance testing of the source is descrbed in Section 8. Section 9 consists of some concluding remarks and recommendations.

2. LIDAR TECHNIQUES FOR REMOTE DETECTION OF GASEOUS CHEMICAL SPECIES

The first uses of lasers for remote sensing were in radar type applications. Consequently, the acronym LIDAR for Light Detection and Ranging was applied to laser ranging systems. The first use of LIDAR, in 1963, located turbidity in the upper atmosphere[19]. Soon thereafter LIDAR sensing techniques took on many new tasks, such as remote pollutant detection. There exist currently three different means of measuring from a single location remote gas concentrations with LIDAR: fluorescence, Raman backscatter, and long path or differential absorption. These three methods have been thoroughly reviewed[20, 21].

All three techniques may be explained and compared by means of the fundamental LIDAR equation[21]:

$$P_r(R)=\left(\frac{\rho}{\pi}\right)KP_o\left(\frac{A}{R^2}\right)e^{-2\int_0^R \alpha(r)dr} \tag{1}$$

where P_r is the backscattered light signal from a target at range R, P_o is the transmitted power, K is the optical receiver system efficiency, (ρ/π) is the effective reflectivity of the target, A is the area of the receiving telescope, and α is the volume extinction coefficient of the atmosphere traversed by the transmitted and reflected light. Figure 1 shows schematically a typical single-ended LIDAR system. In the figure, light is transmitted to a remote location and is backscattered to the receiver. In the case of fluorescence and Raman backscatter, the return signal is scattered by the species to be detected; which is to say, ρ is proportional to the respective backscatter cross sections. When absorption methods are employed, atmospheric Rayleigh, Mie and/or localized retroreflectors scatter back the transmitted light.

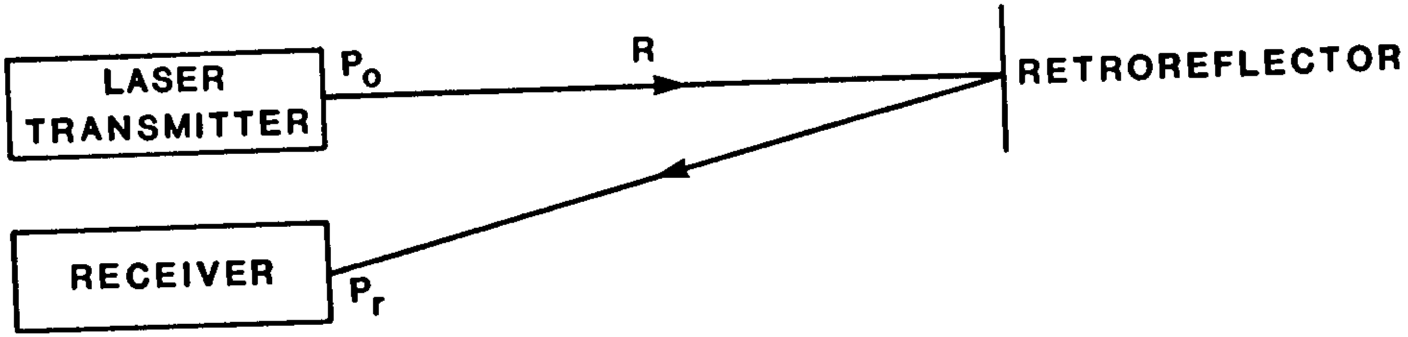

Figure 1. A monostatic LIDAR system.

Fluorescence techniques have little use at atmospheric pressures and temperatures. In the application of this method, transmitted laser light excites the remote species to be detected to a higher energy state and subsequently backscattered fluorescence is measured. However, at normal temperatures and pressures rotational state relaxation processes and quenching fluctuations [20] preclude sufficient signal levels (ρ small) and signal stability (ρ not well known), respectively.

Conversely, Raman methods have enjoyed some experimental field success. In applications, short wavelength laser light is transmitted to a remote chemical species and the backscattered Stokes radiation is detected. This technique has been used, for example, to measure the temperature and pressure of atmospheric water vapor[22]. Recent reviews of remote Raman methods may be found in the literature[23,24].

Indeed, Raman backscattering from methane is currently being pursued for potential coal mine applications by the USBM through its Pittsburg Research Center. In this scheme, 337.1 nm. light from a nitrogen laser is transmitted into a nitrogen and methane atmosphere. The Raman return signals are detected at 365.84 nm. and 373.82 nm., respectively. In practice, the ratio of the methane return signal to the nitrogen return signal is used to calculate the methane density. This system, if employed in a mine, would have the advantage of easily being adapted to other potentially hazardous gasses by a simple replacement of filters in the receiving optics. Additionally, it is advantageous that the Raman technique relies only on the species to be detected for backscattering; consequently, no other backscatter source need be present to create a return signal. Moreover, it is beneficial that Raman LIDAR systems require only a single frequency transmitter, as opposed to a dual frequency source for absorption LIDAR setups.

There are, however, a number of problems that would be encountered by any attempted implementation of such a technique in coal mines. These technical concerns have been outlined previously[25]. The principal probable problems are weak return signals, potentially explosion inducing high voltages (20 kV in the nitrogen laser), and ultraviolet transmitted light levels near safety limits for eye exposures.

In the absorption mode, LIDAR systems transmit light alternately on and off an absorption wavelength characteristic of and particular to the species to be detected. The return signal from the light transmitted off the absorption line provides a measure of the attenuation due to Mie and Rayleigh scattering along the path. The return signal from light transmitted at the absorption wavelength includes the effect of absorption by the species of interest. The difference in the two signals then yields the effect of absorption alone. Thus, in this mode, a sensitive measure of species concentrations is possible. This is the same as to say $\alpha_{on}-\alpha_{off}$ in Equation 1 can be large; and consequently, $P_{r_{on}}-P_{r_{off}}$ can be significant. However, in order for ρ to be large enough for a sufficient signal-to-noise ratio (SNR) at the receiver, it is often necessary for some retroreflector to be introduced into the absorption LIDAR path[26-28]. Fortunately for the potential use of absorption LIDAR in coal mines large amounts (10-200 mg/m^3) of coal dust are present near a working face during mining operations. Thus, the location and timing mandated by statute for methane measurements in coal mines would seem to ensure a high value of ρ in Equation 1. This large value of ρ coupled with the intrinsic sensitivity led Byer to recommend absorption LIDAR to HRL in 1978 as a means to remotely measure coal gas methane[8].

Absorption LIDAR schemes may be divided into two categories: path averaged and range-resolved. The first category yields the integrated species concentration over the entire light path of Figure 1. In this mode, no information about the spatial distribution of the gas is available. The second category gives the desired gas density as a function of one or more spatial coordinates. This distribution may be derived from light time of flight measurements or optical triangulation. To meet the statutory requirement of measurement one foot from the working face, the geometric range resolved method was chosen at HRL in 1978 for experimental work in 1979.

In the same year that LIDAR was first demonstrated, 1963, Schotland[29] measured atmospheric water vapor using range resolved DIAL and a temperature tuned ruby laser. During the last decade numerous reports of DIAL experiments have appeared in the literature. The laser systems employed have included CO_2[30-33], argon-ion[34], IR optical parametric oscillator[35], dye[36,37], dye+SHG[38], and cryogenically cooled lead-salt diode lasers (also known as tunable-diode-lasers or TDLs)[39-42] among others. Examples of DIAL review papers may also be found[26,43,44]. Two papers in particular give a theoretical and experimental treatment of DIAL[26,44].

The fundamental equation for DIAL is given by Equation 1 with:

$$\frac{\rho}{\pi} = \left(\frac{c\tau}{2}\right)\left(\frac{\beta}{4\pi}\right) \tag{2}$$

for temporal ranging and

$$\frac{\rho}{\pi} = \left(\frac{\beta \Delta R}{4\pi}\right) \tag{3}$$

for spatially resolved ranging, where c is the speed of light, τ is the laser light pulse duration, β is the backscatter coefficient at R, and ΔR is the geometrically determined sample depth as shown in Figure 2. The spatial resolution required for methane measurements in coal mines is approximately one foot since law requires measurements be made approximately but not less than 12 inches from the face. Thus in temporal rang-

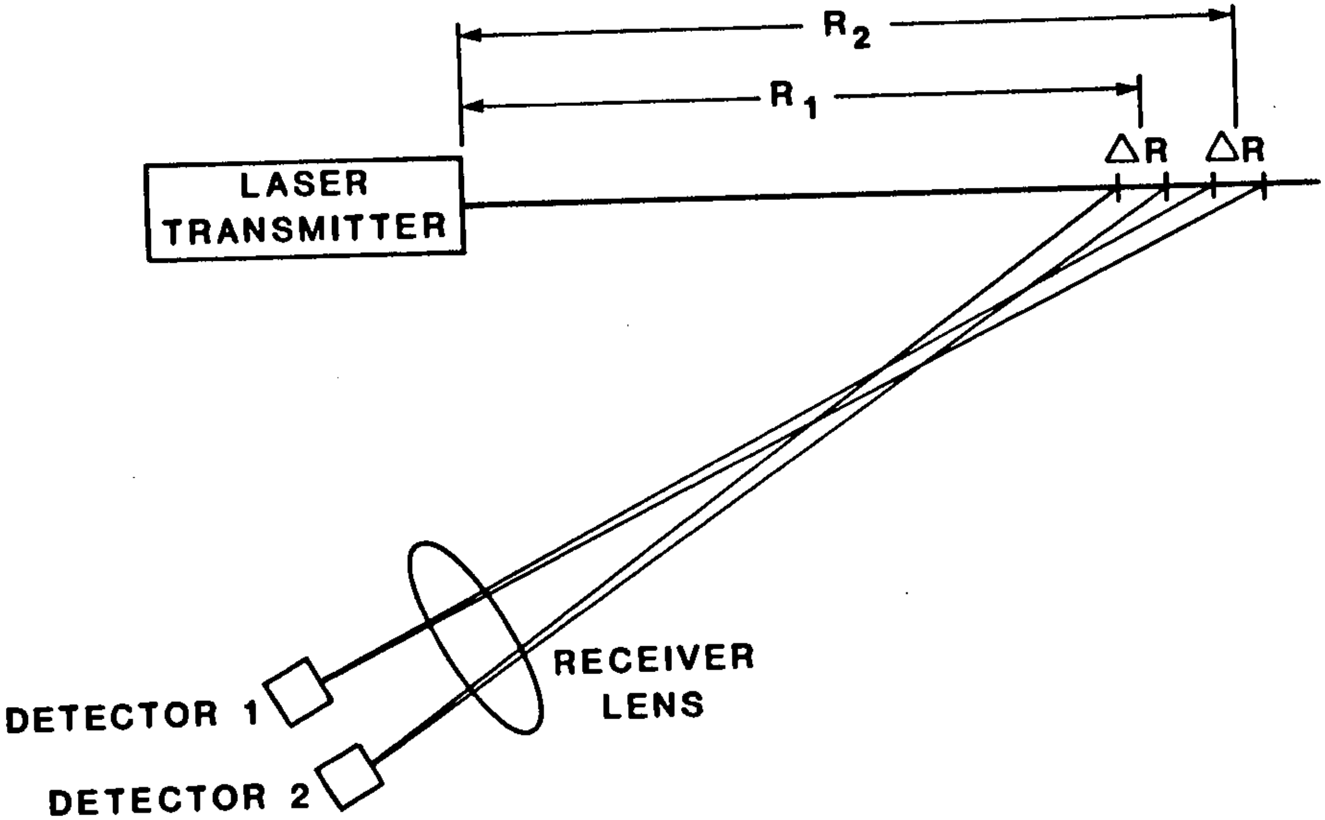

Figure 2. A spatially range-resolved DIAL system.

ing

$$\frac{c\tau}{2} < 1 \text{ foot} \tag{4}$$

is required. This requirement implies a laser pulse duration of less than 2 ns and is the ranging contemplated for the USBM Raman work described above. With a geometrically determined sample depth, there is no restriction on laser pulse duration; and consequently, smaller detector electronic bandwidths are possible. This latter ranging method was chosen by HRL for the 1979 experimental work mentioned previously. This latter technique is also the one that the 1981 OGC report[18] considered for use with diode lasers.

Hence for the work described here, the basic DIAL equation is given by:

$$P_r(R)=\left(\frac{\beta\Delta R}{4\pi}\right)KP_o\left(\frac{A}{R^2}\right)e^{-2\int_0^R \alpha(r)dr} . \tag{5}$$

In this equation

$$\alpha=\alpha_R+\alpha_{MIE}+\alpha_{ABS} \tag{6}$$

where α_R and α_{MIE} are the Rayleigh and Mie scattering coefficients of the coal mine atmosphere and $\alpha_{ABS}=N\sigma_{ABS}$ is the molecular absorption coefficient due to a molecular density N with an absorption cross-section σ_{ABS}. In practice, Equation 5 must be inverted to solve for N. This will be discussed in detail below. There have been several reports during the last decade of successful detection of methane by DIAL methods. The overlap of methane absorption lines with He-Ne and Er:YAG emissions was noted in 1965 and 1972, respectively[45,46]. Soon thereafter LIDAR techniques were applied. Murray and co-workers at Stanford Research Institute used a DF laser and long-path techniques to demonstrate measurement at 3.7 μm[47-49]. Baumgartner and Byer used a tunable IR optical parametric oscillator to detect methane in the open atmosphere at 3.39 and 1.66 μm[50]. Grant et al. at the Jet Propulsion Laboratory have developed He-Ne systems for use along gas delivery pipe lines and at garbage dumps[51-53]. Rosengreen and Altpeter have reported on upconversion of CO_2 light in $AgGaS_2$ and $AgGaSe_2$ for detection of CH_4 in the 3 to 3.5 μm range[54]. Recently, Chan et al. reported using InGaAsP LEDs to measure absorption in methane at 1.33 μm and 1.66 μm by a method analogous to DIAL[55].

In 1975, White and Watkins proposed[56] the Er:YAG laser as a remote sensor of methane. Later they conducted long-path absorption experiments with the same device[57]. In 1979, Egan, DeFreez, Boos, and Byer demonstrated the first geometrically range resolved DIAL measurement of methane[58,59]. In their experiments, Er:YAG laser light was Mie backscattered from remotely situated coal dust suspended in a methane and air mixture simulating a working coal mine face. Recently, a transportable Er:YAG DIAL-MIE backscatter methanometer, built for Bethlehem Steel Corporation (BSC) following the 1979 design, has been successfully demonstrated at a USBM above ground mine simulator and in a BSC under ground working coal mine[60]. The goal of the present project has been to design and build a dual wavelength diode laser light source capable of replacing the Er:YAG source in that methanometer[61,62].

3. SPECTROSCOPIC CONSIDERATIONS

One of the first tasks in the present study was to determine which line or lines of the methane absorption spectrum were most suitable for a diode laser DIAL methanometer. That determination had to be based on the absorption characteristics of the various methane lines, and on the compatibility of the line wavelengths with the technology of diode lasers. Further, it needed to be based on the absorption characteristics of any other relatively abundant naturally occurring atmospheric constituent or any abundant coal gas component.

Three criteria determine the suitability of absorption lines for a diode laser DIAL methanometer. First, the line or lines must be within the spectral region accessible to high power diode lasers exhibiting reasonable efficiency and lifetime at or near room temperature[5]. This requirement restricts consideration to injection diode lasers in the near IR[63]. Second, the line or lines must be of appropriate absorption strength, so that the DIAL measurement process is not impaired either by lack of sensitivity or by excessive attenuation. Based on the experimental work performed at HRL in 1979, an appropriate absorption was determined to be between 10^{-22} to 10^{-21} cm/molecule. Third, the absorption line or lines must have an effective overlap with other coal mine atmospheric constituents of much less than 10^{-22} cm/molecule. For this criterion, it was assumed that interference from sources other than coal gas, such as diesel exhaust, could be ignored.

The first criterion above limits the spectral region that needs to be examined to the range from 2500 to 12,500 cm^{-1} (ie. wavelengths from 4 μm down to 800 nm.)[63]. Further, the room temperature condition mentioned above highly favors the shorter wavelength portion of this region[64]. Hence the near infrared (NIR) spectral region holds the most promise for a diode laser DIAL methanometer.

In 1980, as part of a foregoing project[18], the most comprehensive source of methane absorption parameters, the 1978 AFCRL Atmospheric Absorption Line Parameters Compilation[65,66], was explored. The analysis yielded three methane absorption regions of potential interest. A total of 1741 absorption lines were identified within these three bands and tabulated below in Table I. In the table, the band assignment was given following the notation of Herzberg[67].

Table I AFCRL Methane Absorption Regions

Band Label	Wavelength Range (μm)	Wavenumber Range (cm^{-1})	Assignment
I	3.16-4.00	3167-2500	ν_3
II	2.34-2.42	4270-4136	$\nu_1+\nu_4$
III	1.64-1.70	6106-5891	$2\nu_3$

Absorption lines with a strength in the range mentioned in the second DIAL criterion above occur in all three bands noted in Table I. However, band I is undesirable because of the requirement of room temperature laser operation. Further, not all bands are equally desirable in other respects, such as the possibility of interference from other atmospheric constituents.

In addition to the problem that no diode lasers operate in band I at ambient temperatures, the band has other major drawbacks. For example, it encompasses nearly 3100 H_2O vapor absorption lines, some with strengths up to 2 x 10^{-21} cm/molecule. Room temperature air at 100% humidity has an H_2O molecular concentration[68] of some 6 x 10^{17} cm^{-3}. Thus it appears that water vapor alone is enough to preclude band I from use, since the present need[5] is for methane detection down to a concentration of some 3 x 10^{16} cm^{-3}.

Table II below shows naturally occurring components of air[69,70]. Table III shows the constituents of coal gas[71]. Of the constituents listed, the AFCRL atmospheric absorption tapes show only H_2O and CO as methane's competitors in band II. CO competition is negligible for the distance range of the present application, since this species does not normally exceed 1 ppm in either the atmosphere or in coal gas.

Table II Naturally Occurring Constituents of Air

Constituent	Listed in AFCRL Tape	percent	ppm	Absorption NIR Bands I or II
N_2		78.1		No
O_2	Yes	20.9		No
CO_2	Yes	0.03		Yes
Ar		0.9		No
Ne			18	No
He			5	No
Kr			1	No
Xe			0.09	No
H_2			0.5	No
CH_4	Yes		2	No
N_2O	Yes		0.5	Yes
H_2O	Yes	Varies	Varies	Yes

While some H_2O lines in band II have a strength approaching 10^{-21} cm/molecule, these have a spectral density smaller than the more intense lines of band I. Also it is possible to find a few methane lines in regions where they are surrounded by water vapor lines of strengths not exceeding 10^{-26} cm/molecule. Consideration of the usual coal gas constituents poses only one other possible problem for band II: that of a conceivably significant abundance of ethane. However, C_2H_6 has no strong absorption spec-

Table III The Composition of Coal Gas

Constituent	Listed in AFCRL Tape	Maximum Amount Present (Volume %)
CH_4	Yes	99
C_2H_6		1.6
C_3H_8		0.05
C_4H_{10}		0.02
C_5H_{12}		$<$ 1 ppm
CO_2	Yes	14.8
O_2	Yes	0.5
N_2		36
H_2		0.02
He		0.05

tra[67] above 3200 cm^{-1}. Thus band II could be used if an appropriate diode laser were available.

It may be noted that until recently no semiconductor diode laser has been available in the spectral region corresponding to band II. However a review of the plots of band gaps and compatible lattice constants in the III-V compound family [63,72] shows that GaSb or InAs could be a binary substrate for lattice matching to AlInAsSb, InGaAsP or InAsPSb quaternary alloys with a bandgap appropriate for band II. A group at the State Rare Metal Research Institute in Moscow has reported work with $Al_xGa_{1-x}As_ySb_{1-y}$ lasers that are matched to GaSb substrates[73], but these particular devices provide wavelengths no longer than 1.8 μm. Also, some work on DH InGaAsSb lasers with an emission wavelength near 2μm has been reported[74]. To this point, work in the United States has concentrated on shorter wavelengths, although reduced Rayleigh scattering in optical fibers for longer wavelengths may drive future research in that direction.

Band III is one of the better known methane NIR absorption bands[75,76]. The search of the AFCRL data revealed some 150 band III absorption lines of appropriate absorption strength. Competition in this band is provided only by a scattering of H_2O and CO_2 lines, none of which has strength appreciably exceeding 10^{-24} cm/molecule. Thus band III has desirable spectroscopic properties for a DIAL methanometer based on the absorption characteristics described above and the technology of diode lasers. At the time of the selection several groups had reported epitaxial growth of room temperature injection diode lasers in the wavelength range of 1.6 to 1.7 μm[12,14,13,15]. The devices were made with ternary or quaternary alloys in the $In_xGa_{1-x}As_yP_{1-y}$ system lattice matched to InP. It however remained to be seen whether DIAL measurements of band III methane lines were compatible with the performance characteristics of this type of diode laser.

First it was necessary to examine the methane absorption lines of band III in greater detail. The emission of a moderate to high power pulsed diode laser typically has a full width half maximum (FWHM) spectral bandwidth of several wavenumbers[63]. So, computer-calculated light transmittance curves were generated for the P, Q, and R branches of the $2\nu_3$ methane absorption band, assuming a 2 cm^{-1} laser bandwidth. A copy of the source program used in generating the curves may be found in Appendix A.

The P, Q, and R branches correspond to the spectral sub-regions 5890-5995, 5998-6005, and 6010-6107 cm^{-1} respectively. The necessary line absorption strength information was digitally filed from the AFCRL tape at increments of 0.1 cm^{-1} between 5890 cm^{-1} and 6107 cm^{-1}. Transmittance curves were then generated around local transmission minima (i.e. absorption maxima) for a supposed CH_4 concentration of 3.2×10^{19}

molecules/cm^2. That number was chosen to model a potential coal mine DIAL measurement situation: 0.1% CH_4 assumed over a 40 ft. path with 2% CH_4 postulated for the 1 foot of path nearest the working face.

The local minima in the transmittance curves so generated for the P, Q, and R branches of the $2\nu_3$ band in no case fell below 95% in the entire range. Even though it is necessary to know the noise limitations of a proposed DIAL detection system, to determine the optimum absorption cross-section[26], it is apparent that the cross-sections are too small if a 0.1% methane concentration is to be detectable.

Curves were subsequently generated for similar parameters except for the substitution of a 1 cm^{-1} laser bandwidth and a 0.2 cm^{-1} bandwidth. Figures 3 through 5 show that a source with a 0.2 cm^{-1} (FWHM) bandwidth would have a transmission of only some 85% when tuned on to one of the stronger absorption lines. The peak absorption seen in Figure 5 on the R4 line corresponds to an absorption coefficient of approximately 0.15 cm^{-1} atm^{-1}. This absorption strength would offer large light transmission (85%) over 40 feet and reasonable discrimination (15%) over the 1 foot nearest the working face.

It should be noted here that for Equation 5 to be valid the DIAL laser source bandwidth must be equal to or less than the absorption line width[77]. For methane lines broadened in atmospheric pressure air the linewidth is approximately[70,78,79,80] 0.2 cm^{-1}. Thus to use Equation 5 without situation dependent correction factors the source bandwidth must be less than or equal to 0.2 cm^{-1}.

On the other hand, further reduction in the source bandwidth could lead to difficulties. If the laser line were narrower than the absorption line and tuned to its center the intensity of the returned light signal could be low due to absorption over the

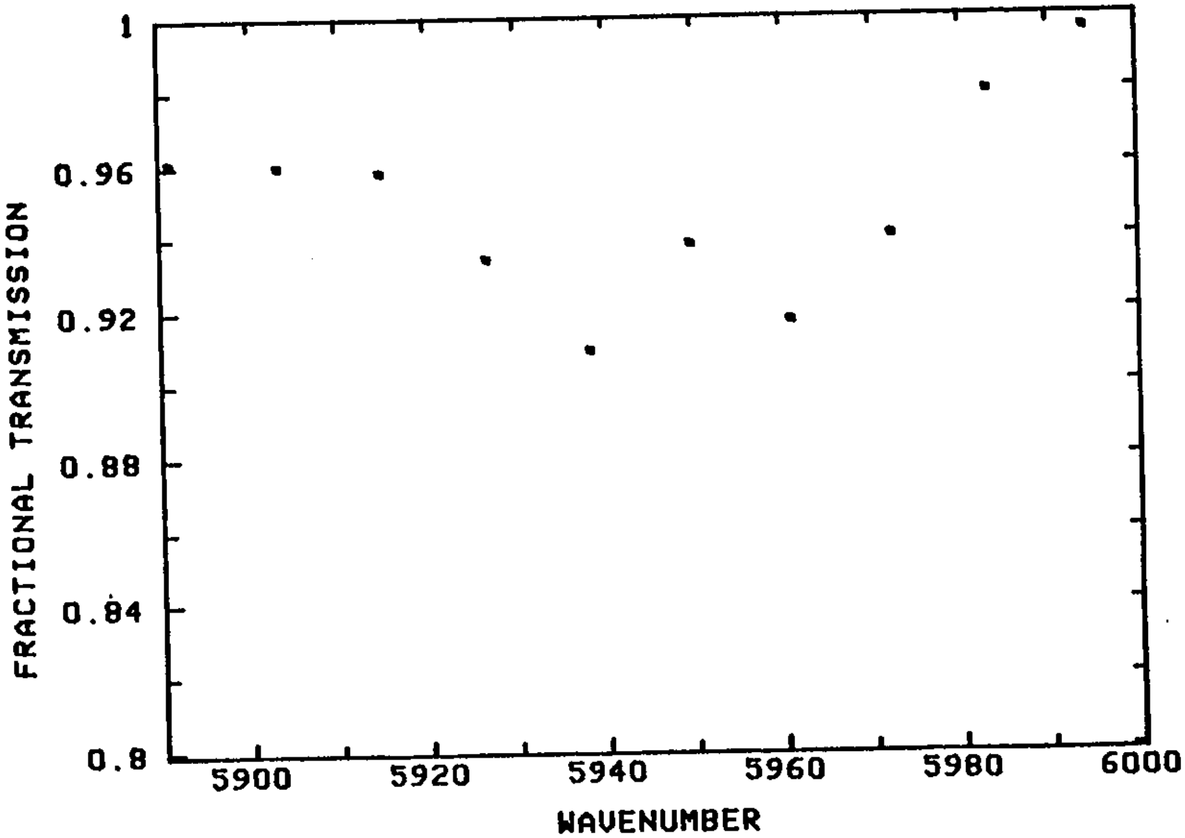

Figure 3. Transmittance through 1.2 cm-atm of CH_4 in the P branch of $2\nu_3$ at a spectral bandwidth of 0.2cm^{-1}.

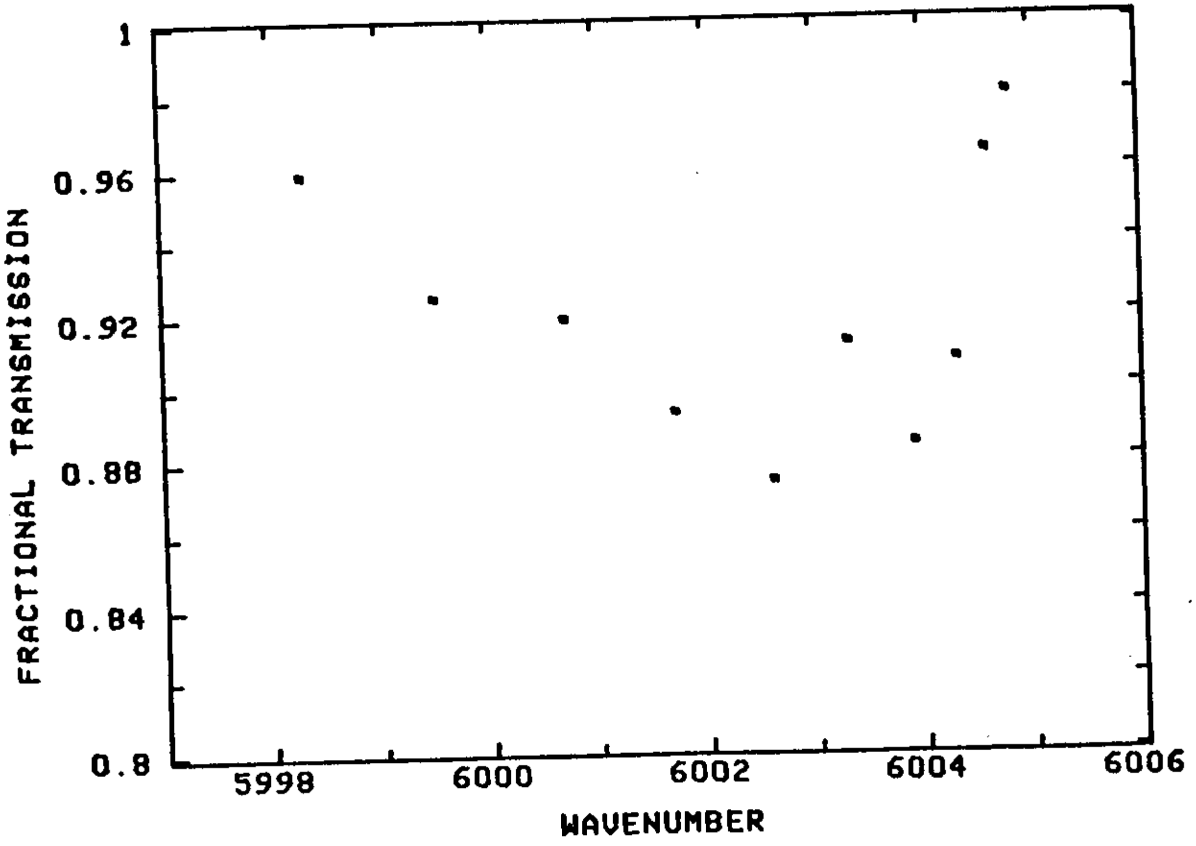

Figure 4. Transmittance through 1.2 cm-atm of CH_4 in the Q branch of $2\nu_3$ at a spectral bandwidth of $0.2cm^{-1}$.

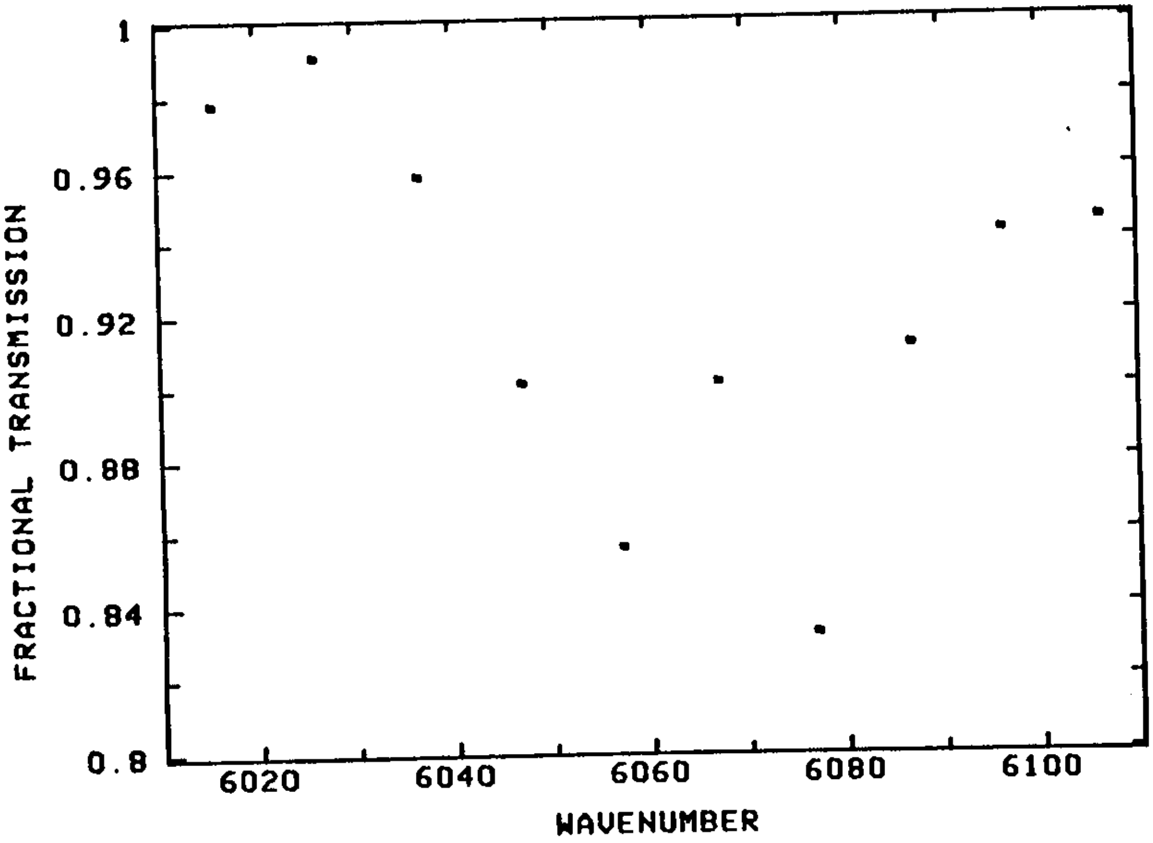

Figure 5. Transmittance through 1.2 cm-atm of CH_4 in the R branch of $2\nu_3$ at a spectral bandwidth of 0.2cm^{-1}.

40 foot distance while tuning instabilities could result if the laser were to be tuned to the edge of an absorption line due to the steepness of the line edges. Moreover, speckle noise would be promoted if the coherence length of the laser output became comparable to or less than that of the envisaged sample volume $\left(\text{coherence length} = \frac{1}{\text{bandwidth in wavenumbers}}\right)$. Thus a spectral resolution of less than, say, 0.05 cm^{-1} would be a handicap.

As Figures 4 and 5 show, the Q and R branches of band III both offer methane lines of appropriate strength for a laser bandwidth of 0.2 cm^{-1} FWHM. However, the Q branch lines have typical separations of only 1 cm^{-1} or so, while those of the other two branches have line separations of about 10 cm^{-1}. The Q branch line proximity could cause difficulties for tuning during the off-line segment of the DIAL process.

In summary, the spectroscopy of methane has been examined to study the applicability of injection diode lasers in a DIAL detection process. The $2\nu_3$ band has been found to be spectroscopically suitable with the Q and R branches therein showing the most favorable absorption strengths. This observation then leads to examination in detail of injection semiconductor laser properties at the band III wavelength in the next section. In particular, the diode lasers used for this project are discussed.

4. SOME CHARACTERISTICS OF 1.65 MICRON WAVELENGTH INJECTION LASERS

There has been considerable interest in recent years in double-heterostructure (DH) semiconductor lasers having an output wavelength longer than that of GaAs ($\lambda \approx 0.9 \mu m$). In all room-temperature injection devices, these lasers have been formed of III-V compound materials. Usually, these have used a quaternary $In_xGa_{1-x}As_yP_{1-y}$ light emitting layer with x and y chosen[81] to match the $a_0 = 5.87$ Angstrom lattice constant of InP. The wavelength range thus possible is interesting for room-temperature sources[14,82,83], for detectors[84-86], and for fiber optic communication with minimum loss and/or dispersion[87], in addition to other applications.

$In_xGa_{1-x}As_yP_{1-y}$ lattice matched to InP has a room-temperature long-wavelength limit of $\lambda \approx 1.65 \mu m$ for the ternary composition $In_{0.53}Ga_{0.47}As$. This alloy has been studied for a diversity of applications including both photoconductive[88] and photovoltaic [86,89,90] types of optical detectors and microwave FET's[91]. Moreover, room-temperature lasing has been obtained in $InP/In_{0.53}Ga_{0.47}As/InP$ structures by three different techniques of layer deposition. The three methods are molecular beam epitaxy (MBE)[14], liquid phase epitaxy (LPE)[13], and vapor phase epitaxy (VPE)[83].

Remote measurements using NIR DIAL require pulsed and high peak power light sources owing to detector dark current limitations[26]. In fact, in the next section it will be shown that P_o of Equation 5 should be greater than 100 mW for a successful DIAL coal mine methanometer. In the realm of injection lasers, 100 mW of light output implies either broad area[63] or phased array devices[92]. Only recently has there been a report[93] on the construction of InGaAsP phased array devices. Thus in the spring of 1981 efforts were started at OGC to locate sources and secure samples of broad area diode lasers capable of high light power pulsed operation in the 1.65 μm spectral region.

Only two of the numerous attempts to secure diode lasers were successful. During 1981 and 1982, B. I. Miller of AT&T Bell Laboratories, Holmdel graciously supplied $In_{0.53}Ga_{0.47}As$ lasers to this project. These devices[14] have been used throughout the course of this project and their properties are described in the following sections. All the properties described represent experiments on several devices and some measurements were conducted on hundreds of lasers. Some of the material presented below was previously reported by DeFreez et al.[17].

The other source of lasers was Cornell University. In return for support of a student Professor Lester Eastman agreed to attempt the MBE growth of some laser material. Unfortunately none of the lasers produced by the Cornell group proved to be of use to this project. Three bars each consisting of several lasers were delivered. The first samples had low threshold currents and light output powers up to about 200 mW. The lasing wavelength at room temperature was however 1.678 μm which is too far from the strongly absorbing $2\nu3$ R branch for practical tuning. The second Cornell sample lasers had unsatisfactory electrical characteristics while the third batch failed to lase at all. As a result only the Bell Lab lasers will be discussed in the balance of this report.

The MBE process[14,94] used to grow the lasers described here started with an n-type InP substrate of (100) orientation. On this substrate, a 1 μm thick $n \approx 10^{18}cm^{-3}$ Ge-doped InP buffer and cladding layer was grown at a substrate temperature of 450 °C to provide a smoother foundation for the GaInAs active layer. The substrate temperature was raised to 510 °C for growth of a lattice-matched $Ga_{0.47}In_{0.53}As$ layer and then lowered to 450 °C for growth of the ≈5 μm thick top InP cladding layer. The latter layer was subsequently doped p-type by Cd diffusion with a duration intended to place a p-n junction at the InP/InGaAs interface.

Plating and sintering was used to create metallic contact layers over both faces of the large-area sandwich, which was then ready for isolation into individual lasers. The end facets were created by (011) cleavage. The sides were partially string sawn and then broken to fashion separate lasers. The lengths of the lasers thus created varied from 300 to 650 μm. The widths varied from 130 to 175 μm. Figure 6 is a scanning electron microscope (SEM) micrograph of an individual laser.

Figure 7 is a SEM micrograph of part of an end facet. The figure shows one feature common to all such micrographs taken, one unusual feature, and rounded artifacts extraneous to the laser. As in all other SEM photos taken, the InGaAs active region is shown as a dark horizontal band of approximately 0.65 μm thickness. This is the thickness that was planned in the MBE deposition[14]. Figure 7 also shows several diagonal dark lines. Only one other facet photographed showed showed such lines. These lines appear to be inclined at a 63° angle to the junction plane. When correction is made for viewing direction, the diagonals are found to lie along the intersection of the $(11\bar{1})$ planes with the end facet (011) plane.

It would thus appear that, in cleaving this facet, some jog planes were created as occasional interruptions of the (011) facet surface. Any such interruption that passes across the end of the active region can be expected to weaken the spatial coherence of the laser output and be a source of non-radiative carrier recombination. This latter circumstance could lead to catastrophic failure at high injection levels. Indeed, the reason this device was used for SEM viewing was its catastrophic failure at a high drive current.

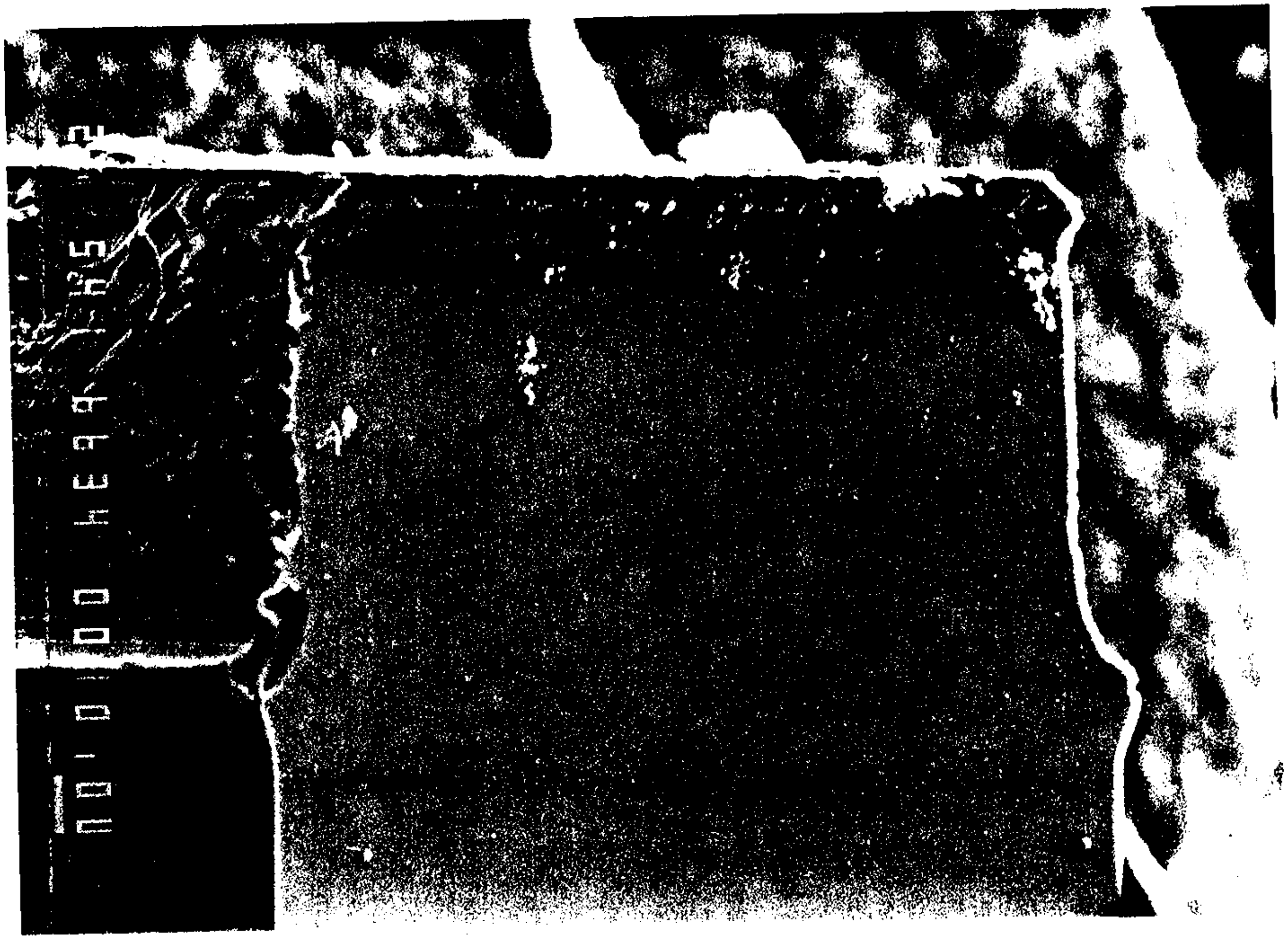

Figure 6. SEM micrograph of a broad area InGaAs/InP laser. The InP substrate, InP cladding layer, InGaAs active region, and top InP cladding layer are visible.

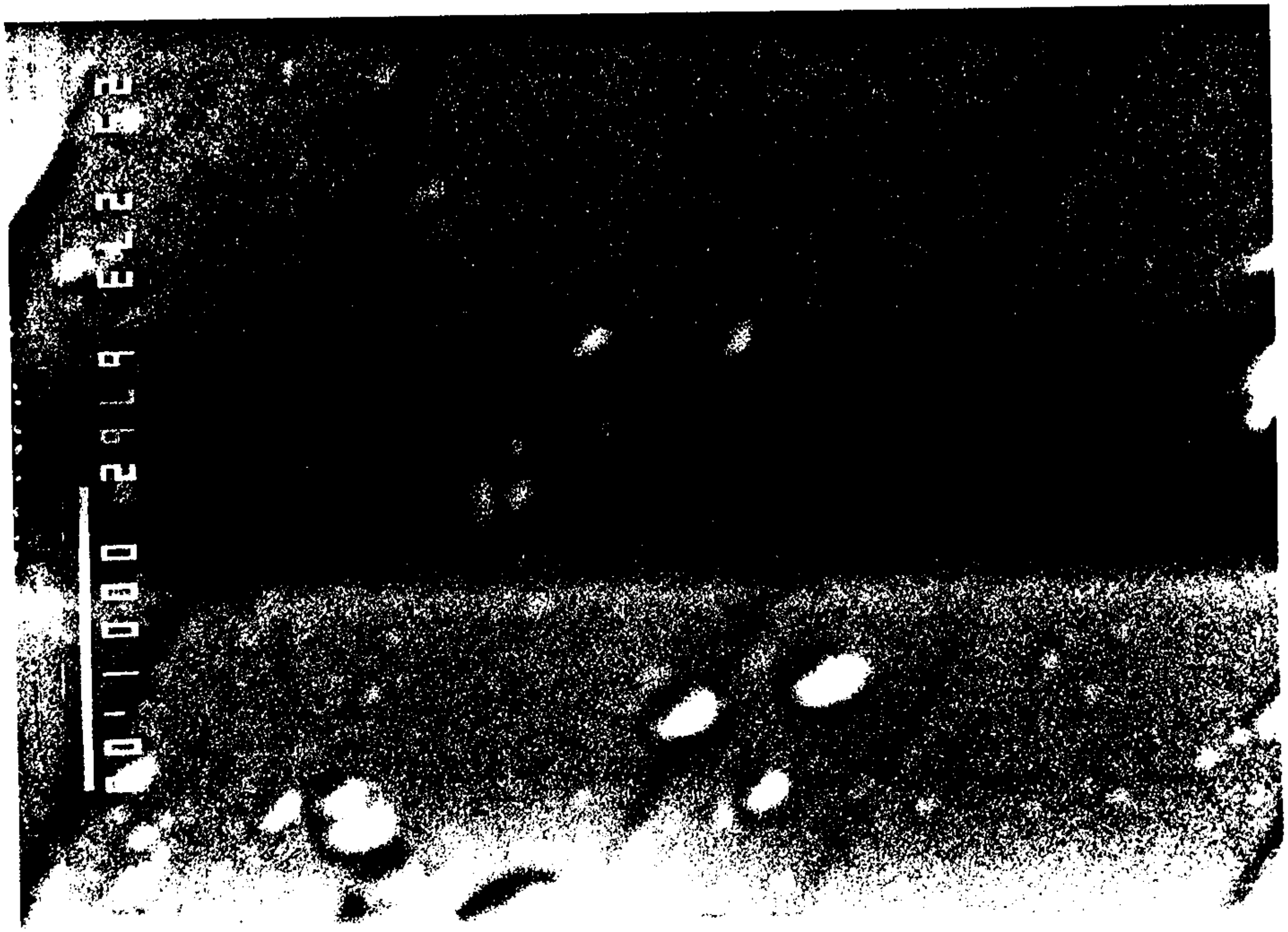

Figure 7. SEM micrograph of part of an InGaAs/InP laser facet. The two light areas are the InP cladding layers and the dark region is the InGaAs active region.

The spectral output for 15 of these lasers was measured at T$\approx$293 K with low duty cycle high current pulses. The pulse repetition frequency (PRF) was between 100 and 500 Hz resulting in a duty factor of $<10^{-4}$ using 150 ns pulses. Owing to the low duty cycle, average input power was low, but peak input power reached as high as 10 W. The drive current used for the spectral runs was from 1.5 to 3 times lasing threshold. The various lasers measured had threshold currents ranging from 1.7 to 4.7 Amps, which is equivalent to an area and thickness normalized threshold of 4 to 10 kA/cm$^2\mu$m.

The spectral response curves showed from 4 to 8 maxima in each case. As would be expected for the pulsed mode operation, the various spectral maxima represent multiple longitudinal mode operation[95]. Figure 8 shows the extreme case of 8 modes spanning the range 1.626 to 1.651 μm. The spectral width shown is greater than 20 nm. Of the various lasers measured while in contact with a room temperature heat sink, none had modal wavelengths outside the limits of those in Figure 8. The spectral curves were obtained by synchronous detection of the output with a germanium photodiode and a Jarrell-Ash Mark X 0.275 m monochromator.

The active region of a DH injection laser, the laser type used on this project, is cladded with material of lower index of refraction than that of the active region itself. The low index cladding forms a dielectric waveguide[96] for the laser light and thus increases operating efficiency[97]. When the guided wave has its E field in the plane of the waveguide, it is said to be a transverse electric (TE) mode[97]. Conversely, when the guided wave has its H field in the plane of the waveguide, it is called a transverse magnetic (TM) mode.

Most recent analyses of the properties of InP/InGaAsP/InP lasers have concentrated on the behavior to be expected with TE mode polarization[98-100]. However, the

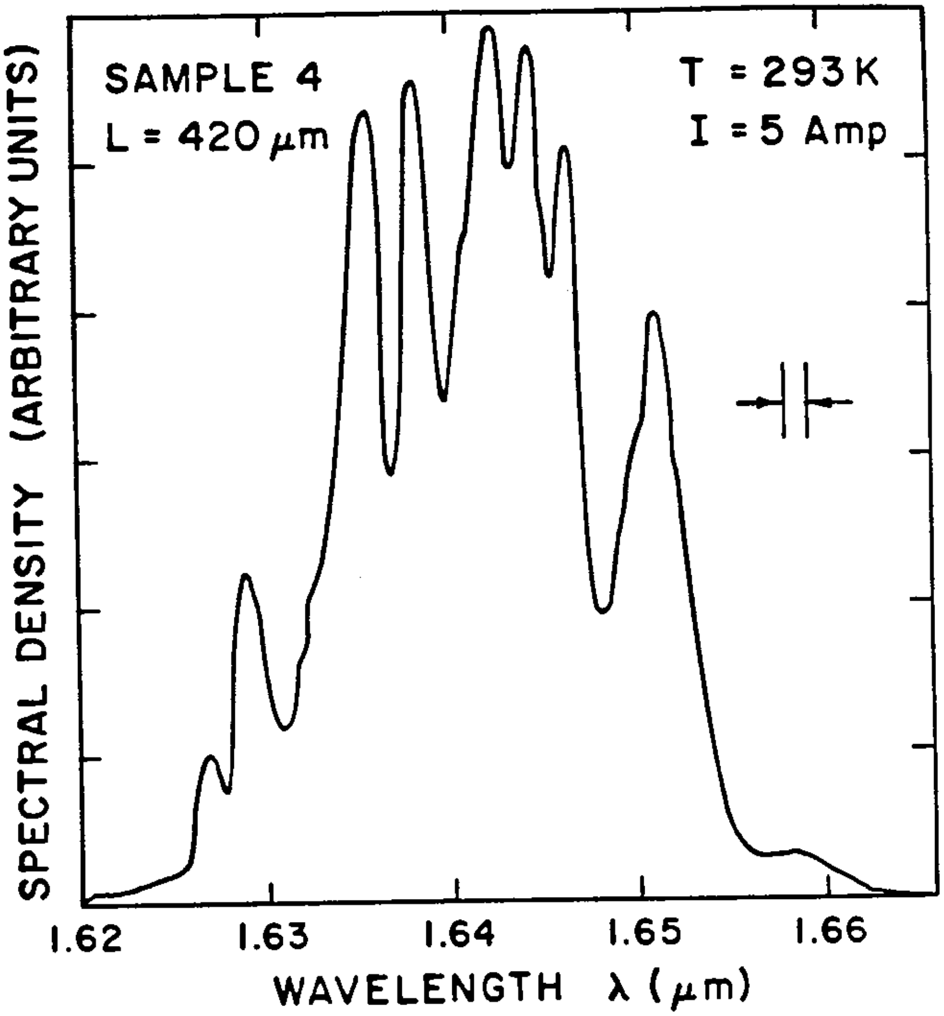

Figure 8. Optical output vs. wavelength for a broad area InGaAs/InP laser. The laser is operated in a low duty cycle with a 150 nsec optical pulse.

lasers of this project were found to be TM polarized. Under the pulsed room-temperature operation described above, the ratio of TM to TE polarization is much greater than 1. No Attempt was made to determine the phase relationship between the TM and TE components of the light output. Figure 9 shows the ratio of TM to TE emission plotted versus drive current for one device. The figure was generated by passing the light from the diode laser through a rotating Nicol Prism and and plotting the ratio of the extrema of the AC current produced in a Ge photodiode versus laser drive current. In the figure, the onset of TM polarization coincides with the lasing threshold. Below threshold, the ratio is slightly greater than 1.

The semiconductor laser monograph literature[101,63,97] has tended to treat only TE polarization for DH lasers, since this is the mode usually seen. That mode is usually dominant because of the higher facet reflectivity for TE modes[102,99,103]. TM-mode dominance thus implies that the gain minus internal absorption losses for such modes is greater than for the TE modes by an amount sufficient to compensate for the higher reflection losses. It will be shown below that this unusual polarization is advantagous for use in an external grating tuned cavity.

Far-field beam divergence measurements were made on 15 of the diodes. The divergence was measured perpendicular to the active region by rotation of the diode laser relative to a fixed Ge photodiode. In each case the far-field distribution appeared to be TM_0, although the active layer is thick enough to support the TM_1 mode as well[96]. Numerical values for the FWHM angular divergence were calculated by least-squares fitting of the data to Gaussian functions, and were all in the range from 62° to 70°. This large divergence is consistent with an active layer thickness in the range 500-700 nm, based on the work of Butler and Kressel[104], and others[106,98], and on the noted similarity of TE and TM mode behavior with respect to angular divergence[97].

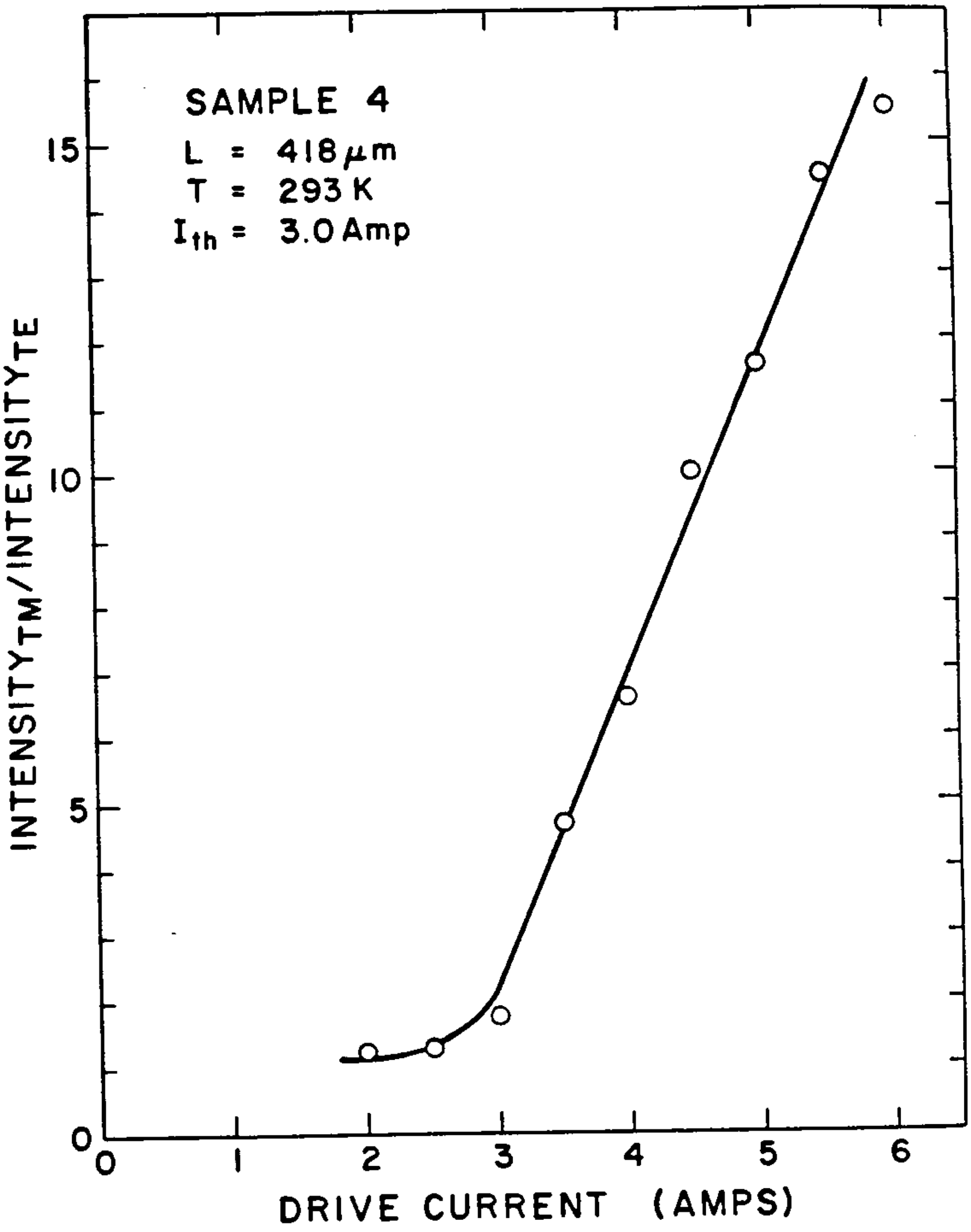

Figure 9. Optical output polarization ratio vs. drive current for a broad area InGaAs/InP laser. The laser is operated in a low duty cycle with a 150 nsec optical pulse.

An output-beam imaging system, using an IR vidicon, monitor, and associated electronics and optics, was set up to examine the diode laser near field spatial distribution. Figure 10 shows one example of the results obtained. The figure was formed by reproduction of a photograph taken directly from the television monitor. The horizontal streaking is an artifact of the television raster. Note that this laser has a filamentary output, with four dominant areas of lasing activity. Such filamentary lasing is often characteristic of broad area lasers because of mode self-focusing[63]. The brighter filaments correspond to regions of smallest threshold current density, since observations while the current pulse amplitude was progressively reduced showed the lasing output more and more confined to the brightest of these regions.

There has been interest recently in the operating lifetimes of InGaAsP/InP injection lasers. and it has been noted that the InGaAsP devices have a potentially longer operating life than their AlGaAs counterparts[63]. The InGaAsP potential for long lifetimes is caused by a number of factors. The dark line defects common to AlGaAs devices have been found to be scarce in InGaAsP structures at both room[107] and elevated[108] temperatures. Long term facet oxidation has been found to be a source of degradation in InGaAsP lasers. However, the degradation rate is about two orders of magnitude smaller[109] than for AlGaAs lasers when operated at room temperature with an optical output of $\approx$1MW/cm^2. In fact, the change in the threshold current for InGaAsP diodes has been measured to be less than 1% when operated for 1000 hours in a CW mode at room temperature[110]. Also, catastrophic dark line defects, common to AlGaAs laser facets, are not generated in InGaAsP devices below 100 MW/cm^2 of light output[111]. The diodes of the present project operating at 100 mW of output power, have a power density of $\approx$0.1 MW/cm^2.

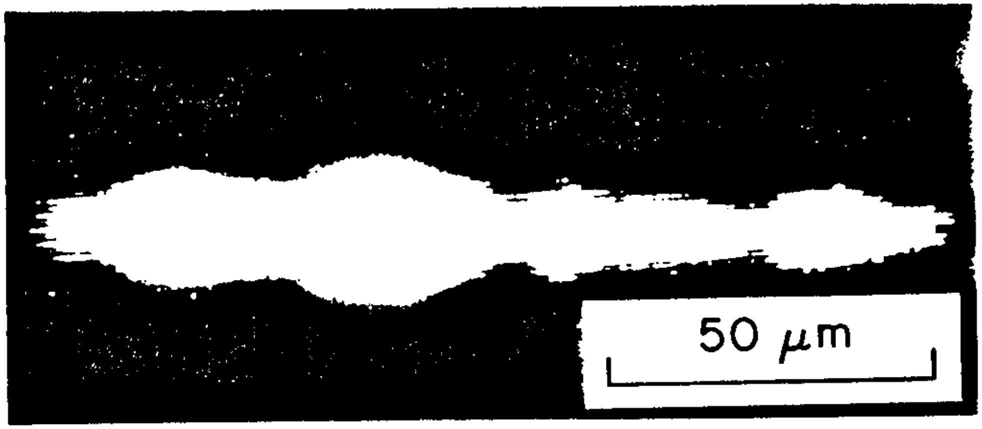

Figure 10. Near field spatial distribution of optical intensity of a broad area InGaAs/InP laser. The laser is operated in a low duty cycle with a 150 nsec optical pulse.

During this project, no long term laser degradation has been observed for the drive currents and output powers used. A life test was conducted on one sample. It was pulsed at 6 Amps and 400 Hz PRF with 160 ns pulses. The diode was observed to stay within ±15% of its average output for 10^8 sequential pulses. with no sign of any downward trend. The diode was then pulsed at 9 Amps, resulting in a 60% increase in the output power. After operation for 10^8 more pulses there was no apparent degradation. Additionally, many devices have been run intermittently over much longer periods, weeks to months, at a 10 kHz prf with no sign of degradation.

However, during the project, several devices catastrophically failed at injection current densities of about 20 kAmps/cm^2. No attempt was made to identify the mechanism associated with this failure mode although the failure symptom is facet damage. Figure 11 shows the facet of one such device. In the figure, the horizontal band, labeled "A", was caused by localized melting at high drive currents. In light of recent work reporting 100 MW/cm^2 thresholds [11] for optically induced facet damage in the InGaAsP device family, it is likely that the observed melting is caused by nonradiative carrier recombination.

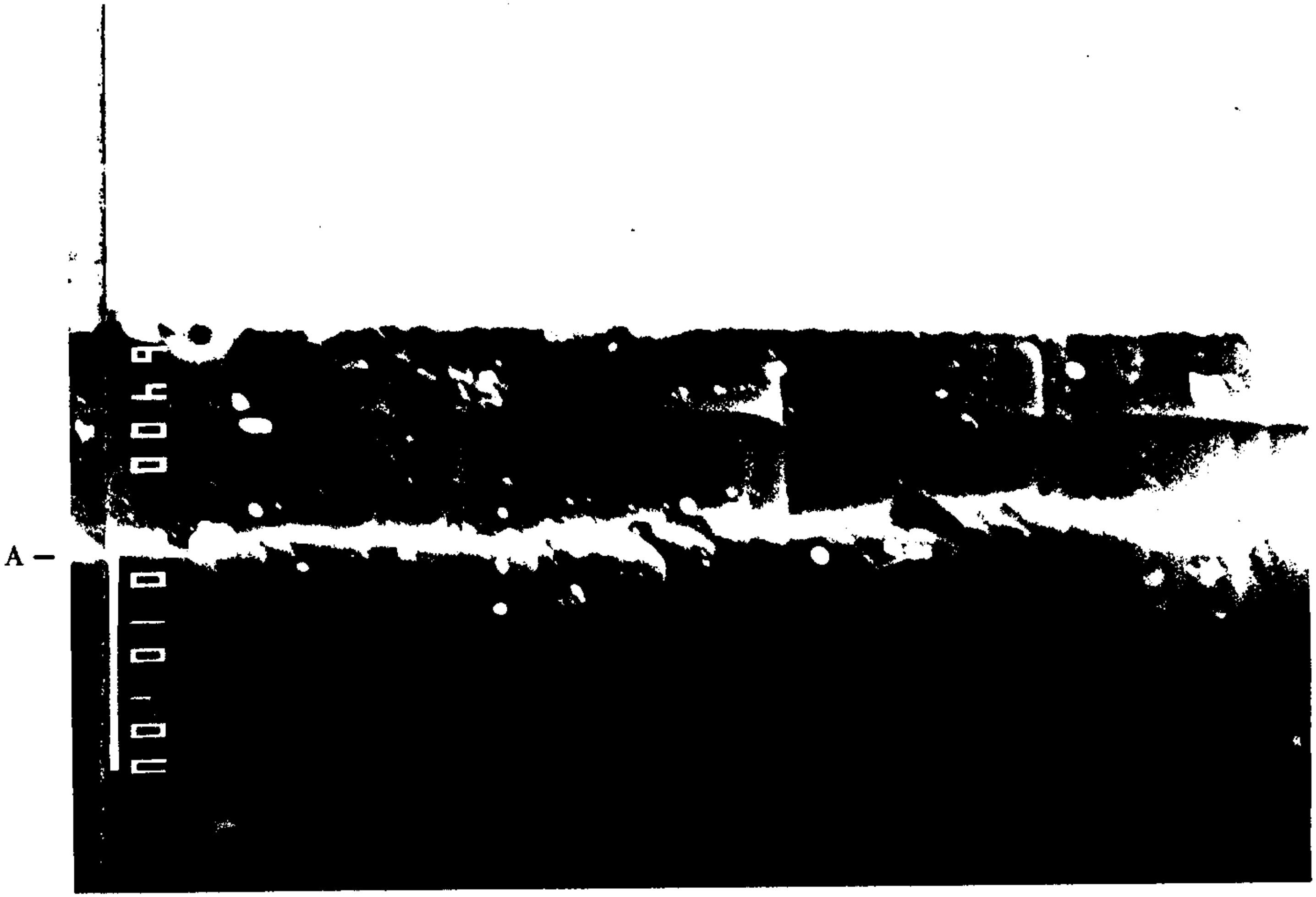

Figure 11. SEM micrograph of facet of InGaAs/InP laser after catastrophic failure.

5. REQUIREMENTS OF A DIODE LASER DIAL METHANOMETER FOR COAL MINES

Federal law[112] also specifies several particular requirements for portable methane detectors. In addition to general requirements about such matters as durability, practicality of operation, and serviceability underground that will not be discussed here, the law lays out specific performance requirements for indicating detectors. Indicating detectors are defined as devices "that will show, within certain limits of error, on an adequate scale, the percentage of methane in a gassy atmosphere" and are the devices appropriate to this report. Specifically, an indicating detector must indicate concentrations of methane as low as 0.25% and should be capable of indicating concentrations as high as 4% with a minimum upper capability of 2%. The indications for the various percentages must be within the limits of error shown in Table IV. The law further specifies that during tests of the instrument made at several concentrations within the range of the detector neither the average of 10 readings nor more than 2 readings for each concentration may exceed the limits of error given in Table IV. The implications of the law on such system properties as optical output power and detector sensitivities will be discussed below. First, however, the maximum amount of safe laser emission near the 1.65 μm wavelength must be calculated.

An eye and skin safety calculation was carried out using the 1980 ANSI Standard[113] and again using the Bureau of Radiological Health regulations[114]. The two approaches yielded equivalent results and the explicit calculation using the ANSI Standard is presented in Appendix B. That calculation assumes a 100 ns pulse duration at a pulse repetition frequency of 10 kHz and gives an allowable peak optical power per pulse of 4.3 watts. The use of these pulse parameters is motivated by the lifetest data mentioned above and the calculations of laser power and pulse repetition frequency

Table IV Allowable Variations in Scale Reading

Methane in Mixtures (%)	Minimum Indication (%)	Maximum Indication (%)
0.25	0.10	0.40
0.50	0.35	0.65
1.00	0.80	1.20
2.00	1.80	2.20
3.00	2.70	3.30
4.00	3.70	4.30

below. The allowable peak optical power indicated by the safety calculation is much larger than that achieved to date with diode lasers operating with a narrow spectral output in pulsed mode. Thus safety is not a limiting factor for a diode laser DIAL methanometer. The required optical power is calculated next.

An analysis of the optical output requirements must start with the fundamental DIAL equation for the Mie backscattered signal (ie. Equation 5):

$$P_r(R)=\left(\frac{\beta_{\mathrm{Mie}}\Delta R}{4\pi}\right)KP_o\left(\frac{A}{R^2}\right)e^{-2\int_0^R \alpha(r)dr} \qquad (5)$$

where P_r is the backscattered light signal from a target at range R, P_o is the transmitted power, K is the optical receiver system efficiency, $\frac{\beta_{\mathrm{Mie}}}{4\pi}$ is the effective reflectivity of the Mie scatter volumes, A is the area of the receiving telescope, and here $\alpha \equiv \alpha_{\mathrm{ABS}}$, is the volume absorption coefficient of the atmosphere traversed by the transmitted and reflected light. Not all the above parameters are well known. In particular, β_{Mie} and K can only be approximated. However, experiments conducted at HRL in 1979 provide data relevant to the Mie backscatter coefficient of airborne coal dust.

In those experiments, $\approx$ 2.5 watts of 1.65 μm radiation was directed onto a coal dust cloud with a concentration of approximately 40 mg/m^3 and the backscattered portion was detected at a distance of 16 feet from the scattering volume. The returned optical power, P_r, detector responsivity, R_D, detected voltage, V_r, and the amplifier gain, g, follow the relationship:

$$P_r = \frac{V_r}{gR_D} \, . \tag{7}$$

Since the experiments suggested $V_r \approx 100$ mv for $g = 10^7$ V/A and a detector responsivity $R_D \approx 0.4$ A/W, P_r must approximately equal 2.5 x 10^{-8} watts. It should be noted here that there was no observed wavelength dependence of the returned signal on the wavelength tuning of the Er:YAG laser during these experiments. Thus, for the given distance and coal dust level

$$P_r = 10^{-8} \, P_o. \tag{8}$$

Based on these results, the value of β_{Mie} is constant over a wavenumber range of few cm^{-1} range near 1.645 μm and is approximately 15 km^{-1}, calculated from Equation 5 using the reasonable assumption of K $\approx$ 0.1. Recent experiments in a working mine[60] show that the coal dust concentration at the active face may be as high as 100 to 200 mg/m^3 and thus that β_{Mie} may be as large as 75 km^{-1} at these dust levels. To further investigate the optical output requirements, an analysis of the various noise sources and their relative sizes must be made.

The signal-to-noise (S/N) power ratio of the returned signal in Equation 5 is given by[115]:

$$S/N = \frac{\overline{i_s^2}}{\overline{i_{SN}^2}+\overline{i_B^2}+\overline{i_D^2}+\overline{i_A^2}} \tag{9}$$

where $\overline{i_s^2}$ = the averaged squared signal current; $\overline{i_{SN}^2}$ = the averaged squared shot noise current; $\overline{i_B^2}$ = the averaged squared background current; $\overline{i_D^2}$ = the averaged squared detector dark current; and $\overline{i_A^2}$ = the averaged squared amplifier noise current. Standard expressions[115] for the various currents and their calculated numerical values are provided in Appendix C. It was ascertained there that

$$\overline{i_{SN}^2} : \overline{i_B^2} : \overline{i_D^2} : \overline{i_A^2} \approx 10^{-28} : 10^{-32} : 10^{-19} i_d : 10^{-31} \Delta\nu. \tag{10}$$

It has been shown [116] that $\overline{i_A^2}$ can be reduced by orders of magnitude with current mode operational amplifiers so that noise source will not be considered further. It can also be seen from Equation 10 that $\overline{i_B^2}$ is orders of magnitude less than $\overline{i_{SN}^2}$ and thus may be ignored in the present context. To know more about the remaining two noise sources, $\overline{i_{SN}^2}$ and $\overline{i_D^2}$, a numerical value must be attached to i_d, the detector dark current.

The magnitude of the detector dark current depends on a number device parameters and on the method of operation. When current mode operational amplification is used[116], the best detection sensitivity is achieved at zero detector bias or for small reverse voltages. It is known from load line analysis that linear operation is also achieved for near-zero bias. Thermally driven carrier generation-recombination is the source of dark noise near zero bias and its magnitude is given by

$$\overline{i_D^2} = \frac{4\, K_B\, T\, \Delta\nu}{R_D} \tag{11}$$

where R_D is the detector shunt resistance. Substitution of a typical value $\approx 10^6\ \Omega$ for a typical small area commercial Ge detector[117] gives a value for $\overline{i_D^2}$ some 60 times that of

$\overline{i_{SN}^2}$, the quantum detection limit. Recently, extensive work has gone into the development and improvement of detectors for the 1.1 to 1.7 μm range. That work has been spurred by the growth of optical fiber technology, and the desire to operate fiber optic systems at wavelengths of minimum absorption and dispersion[87, 118]. In efforts to develop new germanium avalanche photodiodes, dark current densities near 10^{-3} Amp/cm^2 have been reported[119, 120] for room temperature large reverse bias operation. These current densities are slightly lower than those of the best commercially available devices and those of the HRL methanometer. However, these kinds of devices cannot be expected to show decreased noise at zero bias since the generation-recombination noise source is the same as that of previous germanium devices.

Detectors using alternative materials to germanium have been in active development. They are based on the quarternary $In_xGa_{1-x}As_yP_{1-y}$ system of direct-gap III-V semiconductors. This recent work on detectors[84, 86, 90, 121, 122- 124, 85, 125, 126] parallels the work, and is based on much of the same technology, as the laser diode source development in that quarternary system. In particular, Pearsall reported[86] production of new InGaAs/InP photodiode structure with a dark current density of 3 x 10^{-7} Amps/cm^2 at room temperature and a 1 volt reverse bias. The novelty of this device arises from physical separation of the photon absorption and depletion regions. Such a separation would not be possible below the direct bandgap threshold in a semiconductor such as germanium (ie. for $\lambda > 1.5$ μm). By placing the depletion region in the high bandgap ($\lambda \approx 0.9 \mu$m) InP portion, generation-recombination of carriers is minimized thus reducing the dark current and the generation-recombination noise associated with it. Thus a back biased dark current of 3 to 4 orders of magnitude smaller than in the best Ge devices is achieved. Pearsall also notes that the photon quantum efficiency is nearly 100% for $\lambda = 1.65$ μm when the light is incident on the epitaxial side. That is a different situation from germanium for which the useful absorption decreases dramatically below the 1.5 μm bandgap. Thus, with this type of detector, near shot noise limited operation is obtainable under the conditions described above and in Appendix C.

Due to the technical developments discussed above, high sensitivity back-side illuminated GaInAsP/InP detectors have recently been introduced to the commercial market. A typical such device[127] has a sensitivity of -55 dBm at a 10^{-9} bit error rate (BER) and a bandwidth of 5 MHz. A BER of 10^{-9} is equivalent[115] to a signal to noise ratio (SNR) of 11:1 and 5 MHz is the bandwidth appropriate to a 100 ns optical pulse. Thus, this detector can detect 3 x 10^{-9} watts of optical power near 1.6 μm with a signal to noise ratio of 11:1. Using Equation 8, an optical output power of 100 mW would yield a SNR of 3.5:1 for a single pulse of light backscattered from 40 mg/m^3 of coal dust at a distance of 16 feet or from 200 mg/m^3 at 35 feet.

Having obtained the value for the theoretically possible voltage SNR, the needed ratio for a DIAL measurement must now be ascertained. The federal requirements for a portable methane detector are displayed in Table IV. It may be seen from the table that the allowed fractional errors in the measured methane concentration vary from ±0.6 at 0.25% CH_4 to ±0.075 at 4% CH_4. The law[112] further requires for approval that a methane monitor must fall within the indicated errors in at least eight out of ten trials.

In Appendix D the inversion of the fundamental DIAL expression, Equation 5, is derived. Equation D.17, therein, shows the completed inversion and is given by

$$\overline{C} = \frac{C'(r_2 - r_1)}{2(R_1 - R_2)} \frac{\ln\left(\frac{V_{r,on}(R_2)}{V_{r,on}(R_1)}\right) - \ln\left(\frac{V_{r,off}(R_2)}{V_{r,off}(R_1)}\right)}{\ln\left(\frac{V_{on,1}}{V_{on,2}}\right) - \ln\left(\frac{V_{off,1}}{V_{off,2}}\right)} . \qquad (12)$$

in the notation of the appendix. Appendix D also contains a detailed derivation of the error propagation inherent in the DIAL measurement. A simple expression for the allowable standard deviation in the measured voltages as a function of the standard deviation in the gas concentration and the amount of absorption in the sample volume during the on line portion of the DIAL process is given in Equation D.28:

$$\frac{\sigma_V}{V} = \frac{1}{2}\,\frac{\sigma_{\overline{C}}}{\overline{C}}\left|\ln\left(\frac{V_{r,on}(R_2)}{V_{r,on}(R_1)}\right)\right|. \qquad (13)$$

The quantity inside the absolute value bars is just the volume absorption coefficient times the sample volume length, i.e., $\alpha_{ABS}\,(R_2-R_1) = \alpha\,\overline{C}\,(R_2-R_1)$. Thus

$$\frac{\sigma_V}{V} = \frac{\sigma_{\overline{C}}\alpha\,(R_2-R_1)}{2} \qquad (14)$$

where $\alpha \approx 0.15$ (cm atm)$^{-1}$ for a 0.2 cm^{-1} source bandwidth (see Section 3). Evaluation of Equation 14 using the most restrictive condition in Table IV, $\sigma_{\overline{C}} = 0.0015$ atm, and $R_2-R_1 = 60$ cm yields a voltage SNR of 150:1 to obtain the desired $\sigma_{\overline{C}}$.

Further consideration is needed however in light of the statutory stipulation that an indicating methane monitor must satisfy the requirements laid out by Table IV in eight out of ten trials. The failure probability in 10 trials can be calculated from the binomial distribution. Let p be the probability of failure in one trial then the probability of two or fewer failures is $(1-p)^{10} + 10p(1-p)^9 + 45p^2(1-p)^8$. Fewer than two failures in ten trials will occur 99% of the time if $p \leq 0.048$. Now if the source of error in the methane measurement is random with a zero mean normal distribution the probability of a failure in a single measurement $p = 0.0454$ if the standard deviation is one half the allowed margin for error. This means that the SNR calculated above must be doubled to 300:1. Comparison of this SNR with the single pulse SNR of 3.5:1 derived above reveals the need for a signal to noise improvement ratio (SNIR) of approximately 90:1. Signal averaging techniques can be used to improve the SNR.

One method of averaging often used with low duty cycle signals is the so-called boxcar method. Boxcar averaging yields a SNIR[128]

$$\mathrm{SNIR} = \left[\frac{2N}{5}\right]^{1/2} \tag{15}$$

where N is the number of pulses to be integrated. This method of integration is best used for large instantaneous signal low duty cycle averaging. Further enhancement to the SNIR beyond that of Equation 15 can be produced in this mode through preintegration techniques when sufficiently large instantaneous signals are available. However, in the present context the returned optical signal is not large relative to noise sources, so preintegration techniques are not feasible. Moreover, boxcar averaging is a nonlinear integration process that favors the last signals received and thus can introduce systematic errors in a non-stationary process. It will be seen below that the DIAL measurement process when averaged over many pulses is typically non-stationary. It will also be shown below that a SNIR greater than that of Equation 15 can be achieved by a digital signal processing method.

In recent years, there have been several investigations into the various sources of error in the DIAL measurement accuracy[28, 129, 130-133] and into the signal processing techniques needed to minimize the errors[27, 134, 135-138]. DIAL return signals are randomly affected by turbulence induced fluctuations in the absorber concentration, scintillation, beam wander, speckle, and the angle of arrival and by electronic noise. Differential reflectivity and differential background extinction are also sources of systematic error in DIAL measurements.

It was shown in Section 3 that differential background extinction due to any of the normal constituents of air or coal gas is satisfactory for DIAL measurements in the wavelength region of the $2\nu_3$ overtone of methane. Furthermore, the differential reflectivity from coal dust aerosols typical to coal mines was observed to not affect the backscattered light over a few wavenumber region near the 1.65 μm wavelength of an Er:YAG laser. So, the last two potential sources of systematic error are not a problem for a diode laser DIAL methane measurement at 1.65 μm in coal mines. The various sources of potential random signal errors must now be considered in turn.

The signal fluctuations caused by atmospheric turbulence and electronic noise may be classified by the degree of temporal correlation that they possess between on- and off-line portions of the DIAL process. Electronic noise between signal channels in a DIAL system is uncorrelated and may be reduced through averaging techniques by the factor $N^{-1/2}$ where N is the number of samples averaged. Thus a SNIR of $N^{1/2}$ is possible for signals affected by such noise. Beam wander and angle of arrival variations should be neglible because of the short ($\approx$ 10m) path length for a coal mine measurement. Scintillation effects should also be neglible [129] for a receiver aperture radius

$$R \geq (\lambda L)^{1/2} \tag{16}$$

where λ is the laser wavelength and L is DIAL total path length. $(\lambda L)^{1/2}$ is a transverse coherence length and is equal to approximately 4 mm for a 10 m path length and a wavelength of 1.65 μm. Last, speckle effects should be nonexistent since the bandwidth gives, as shown in Section 3, a longitudinal coherence length less than the length of the scattering volume.

The effects of turbulence on the two returned signals of a DIAL process are correlated for periods of up to 10 milliseconds since the atmosphere is "frozen" for such periods[130, 139]. Thus, fluctuations of the returned signals because of methane concentration variations are correlated during this time interval. It has been shown by Menyuk and Killinger[137] that when the returned light pulses during the on- and off-line parts of the DIAL process arrive within the correlation time of the atmosphere subsequent signal averaging over many pulses diverges from the $N^{1/2}$ improvement mentioned above for independent measurements. They found that the SNIR was less than $N^{1/2}$ if the signals were averaged as

$$C = \text{constant x} \ln\left[\frac{<V_{i,1}>}{<V_{i,2}>}\right] \tag{17}$$

where $< >$ represents time averaging. On the other hand, they found that the SNIR was greater than $N^{1/2}$ for signals averaged as

$$C = \text{constant x} \ln\left[<\frac{V_{i,1}}{V_{i,2}}>\right]. \tag{18}$$

They attribute these properties to high correlation between the on- and off-line pairs and residual correlation over many pulses because of the non-stationary nature of the absorber concentration. Here it will be assumed that a SNIR of at least $N^{1/2}$ can be achieved for a coal mine DIAL process with the latter signal processing method. Thus a 10 kHz data collection rate over a period of less than 1 second is sufficient to achieve a SNIR to meet the SNR requirements derived earlier in this section. This assumes that the source properties presented in Section 4 can be modified to match those required by this derivation.

6. OPTICAL DESIGN OF A DUAL DIODE LASER SOURCE

Although not all the properties of high optical power diode lasers described in Section 4 match well with those source requirements developed in Sections 3 and 5 most properties of broad area $In_{0.53}Ga_{0.47}As/InP$ diode lasers are suitable for a coal mine DIAL methane measurement. The achievable optical output power, $\approx$ 100 mW, was shown to be sufficient in Section 5. The measured lifetimes at pulse repetition frequencies of 10 kHz represent a potentially long period of service in a methanometer. The PRF is sufficient to obtain the necessary SNIR in less than one second. Also, the TM polarization characteristic described in Section 4 is, the polarization needed for operation in an external grating cavity. Furthermore, the operating wavelength of $In_{0.53}Ga_{0.47}As/InP$ lasers is near the $2\nu_3$ absorption band of methane. However, the typical spectral bandwidth at this wavelength, as shown in Figure 8 is much greater than the $\approx$ 0.05 nm width required for sufficient absorption to make the DIAL process feasible. Thus, a method is needed to control the bandwidth and wavelength while maintaining the other diode laser properties.

All lasers consist of a gain medium and a resonator cavity for electromagnetic wave feedback with the cavity defined by mirrors. For simple diode lasers the mirrors are facets cleaved parallel to the crystal planes of the as grown semiconductor. To modify the spectral properties of a laser it is necessary to modify its internal characteristics ,i.e., the gain medium or resonator cavity. External resonator diode lasers in which the crystal facet mirrors are replaced by external reflectors have been used to modify the spectral[140-149] properties normally observed. The intrinsic properties of diode lasers in external cavities or near reflecting surfaces, such as lenses, optical fibres, or optical disks have been thoroughly studied[150-157]. The most recent review paper[158] on diode lasers coupled to external resonators was published in 1979.

Almost all published accounts of **continuous** wavelength tuning and bandwidth control of diode lasers have reported on antireflection (AR) coated devices [140-143,145,148] in external cavities. The few exceptions[159,160] have involved low power single stripe devices in complicated temperature and current controlled servo-loops. By AR coating the diode laser, its original facet reflectivity is nullified and thus the cavity can be extended to some external optical element. This allows access to the cavity and it is then possible to insert a wavelength controlling element such as an etalon, birefringent filter, or grating. In the present project an external 600 l/mm grating blazed for operation at $\approx 1.6\ \mu m$ was substituted for one facet mirror after the facet was AR coated with a SiO coating. The grating, by selectively feeding back only a narrow spectral bandwidth of optical power to the active volume of the diode, forces the laser to oscillate in a limited spectral region. It should be noted here that in at least one previous case[161] the facet reflectivity was nullified by lapping the facet at Brewster's angle. However, this method produced localized mechanical damage to the laser and severely degraded its lifetime.

It has been shown[162,163] that a dielectric film with index of refraction given by

$$n_f = \left(n_L n_{ext}\right)^{1/2} \tag{19}$$

and thickness given by

$$t = \frac{\lambda}{4n_f} \tag{20}$$

where n_L is the effective index of refraction in the laser, n_{ext} is the external index, $n_{ext} = 1$ for air, and λ is the vacuum wavelength of the laser radiation, gives a theoretical air-laser reflectivity of near zero. Thus by this coating technique a diode's emission may be decoupled from its normal oscillator modes and its spectral output may be controlled by substitution of a variable dispersion external cavity. The results for a SiO coating are shown in the next section.

The resulting bandwidth of an external grating cavity may be obtained from the standard grating equation as shown by Heckscher and Rossi[143] and is given by

$$\Delta\lambda = \frac{\lambda d}{2 f \tan(\theta)} \tag{21}$$

where d is the active region thickness, f is the laser to grating collimating optics focal length, and θ is the grating angle of incidence for a grating in a Littrow mount. This formula was derived using geometric optics. Substitution of numerical values appropriate to the present project, $\lambda = 1.65\ \mu m$, $d = 0.65\ \mu m$, $f = 25$ mm, and $\theta = 30$ degrees as calculated from the grating equation[162] for a 600 l/mm grating, yields a bandwidth of $\Delta\lambda = 0.04$ nm. It is demonstrated in Section 7 that the bandwidth achieved during this project has never equaled that predicted by Equation 21. Therefore, it is important to ascertain if this formula holds under a more sophisticated analysis of the spectral bandwidth.

A better estimate of the bandwidth to be expected from an external grating cavity can be achieved using coupled-mode theory of guided electromagnetic waves[164]. Many recent developments [165-167] in coupled mode theory have been driven by the interest in coupling the optical output of diode lasers to various types of waveguides, for example to optical fibers or thin films. Since a diode laser active region is itself a waveguide, it is appropriate to think of the coupling of the returned light from an external grating to the diode laser as a diode laser to waveguide problem. A revised estimate of the achievable spectral bandwidth is calculated in Appendix E using coupled-mode theory.

The derivation presented in Appendix E yields an expected bandwidth of 0.1 nm. This spectral width is 2.5 times that calculated by the generally accepted geometric optics method and is, as shown in Section 7, closer to that observed in experiments. It should be pointed out that this wider bandwidth reduces the absorption that may be achieved slightly below that calculated in Section 3.

The degree to which an external grating can control the wavelength and bandwidth depends on the efficiency of the AR coating in suppressing residual modes of the diode laser cavity and on the reflective efficiency of the grating. It is known[168] that a diffraction grating is effective only for light polarized perpendicular to its grooves. In a narrow bandwidth external grating diode laser cavity the grating grooves must be in the plane of the active region to ensure that the small dimension of the junction acts as a slit that rejects all but the desired part of the spectrally dispersed fed-back light. Because of this alignment, the fed-back light is then polarized perpendicularly to the active region plane, that is it is TM polarized. If the diode laser is intrinsically TM polarized, the returned optical power couples with the laser gain medium better than does TE polarized light. It was shown in Section 4 that the lasers used in this project are TM polarized which is advantageous for use in an external grating cavity.

It was shown in Section 5 that a significant signal to noise improvement ratio (SNIR) could be achieved for the DIAL process when the on- and off-line portions of the process were temporally separated by less than the decorrelation time of the atmosphere, ie. less than 1 to 10 ms. Double pulse DIAL systems have been used to take advantage of the improved SNIR. These systems have either used the combined output of two laser cavities operating at separate wavelengths[135] or have used a movable wavelength control element in a single cavity[58]. The former scheme suffers from duplication of all cavity components while the latter is necessarily slow because of mechanical inertia. For an external grating resonator diode laser system, a second diode laser may be placed adjacent to the first in the cavity. This second laser will be located at a slightly different angle to the grating relative to the angle of first laser and will oscillate at a different wavelength. So, the on- and off-line portions of the DIAL process could be initiated by alternate electrical drive pulses to the two diodes. This pulse scheme, with a 10 kHz interlace rate, was implemented for this project and its mechanical and electronic construction are described in Section 7.

A final point about external resonator diode lasers: it is necessary to calculate the angular positioning stability required for the grating to maintain the wavelength of the light fed-back to the diode laser active volume within the bandwidth calculated in Appendix E. It is clear from a simple trigonometric argument that the angular stability for small angles must be given by the ratio of the effective slit half-width to the focal length of the collimator optics

$$\Delta\theta < \frac{\mathrm{d}}{2\mathrm{f}} \tag{22}$$

where the symbols are those defined following Equation 21. Numerical substitution yields $\Delta\theta < 25$ microradians.

Although exotic alternatives such as holographic optical elements are conceivable as the diode laser to grating coupler, common sense engineering suggests that refractive lenses or mirrors are more appropriate. Mirrors for use in the near infrared can be classified in turn into two categories: dielectric film and metal.

Work with refractive optics at the wavelength in question is both unusual and difficult. The difficulty arises from the low index of refraction of glasses, $n \approx 1.4$, at 1.65 μm wavelength. So, it is necessary when using glasses to have either more, or more powerful, optical elements to duplicate the effects achieved at visible wavelengths. During this project, several optical design and fabrication businesses were contacted regarding design and construction of a lens system to couple a 1.65 μm wavelength diode laser to a diffraction grating. Only one company, Research Optical Systems Group, Inc., (ROSG) was willing to bid on design and fabrication of such a device.

The pre-design plans from ROSG called for a five or six element glass lens system or a three or four element silicon lens system. The former would suffer from only 83-86 % optical throughput because of reflection and scattering from the large number of optical surfaces involved and would also be bulky. The latter would be difficult to align since silicon is opaque to visible radiation. Implementation of either design would have been prohibitive due to engineering and tooling costs. The large number of problems associated with refractive optics made reflective optics more attractive for this project. Hence, it was decided to design a reflective laser-grating coupling system.

Since the coupling of the diode laser to a grating is from a finite conjugate point to an infinite conjugate, the mirror shape that would seem to give minimum optical aberration is parabolic. Furthermore, an unobstructed optical path from the diode laser to the grating requires an off-axis parabola. The focal length, f, needed to give adequate bandwidth, as discussed in the above, along with the the lateral dimension of the mirror needed to capture most of the rapidly diverging light emitted by the diode laser (see Section 4) necessitate a drastically curved parabolic surface.

Dielectric thin film coatings are commonly used to achieve high reflectivity in the NIR. However, these coatings are difficult to fabricate on surfaces of much curvature. All the commercial coating houses contacted during the project declined to become involved in a job of this nature.

Metal mirrors are the other possibility for reflective optics in the NIR. In particular, aluminum mirrors are both light weight and have a reflectance of over 96% at a wavelength of 1.65 μm at normal incidence^{169}. At other than normal incidence the reflectance increases and at any angle the reflectance is much greater than the total transmission for a multi-element refractive collimator. On this basis, an aluminum off-axis paraboloid of revolution was chosen as best for this project. Furthermore, for ease in aligning the mirror to the rest of the external cavity components, it was decided to use a right-angle off-axis paraboloid. That is to say, the axis of rotation of the paraboloid would be perpendicular to the axis of the diode laser emission.

The required dimensions, such as focal length and angular swing, for a right angle paraboloid may be determined with the help of Figure 12. The figure shows a cross-section parallel to the axis of revolution of the paraboloid. The restricting conditions on parameters displayed in the figure are as follows. The diode laser is located at (F,0,0) where F is the focal length of the paraboloid. $\alpha_1-\alpha_2$ must equal the beam divergence of the diode laser to gather most of the light emitted. $\frac{\alpha_1+\alpha_2}{2} = 90$ degrees so that the paraboloid is right angle off-axis. The positions along the y axis where the laser half-angle points intersect the parabola are y_1 and y_2. The apparent width of the diffraction grating as seen from the parabola is given by y_2-y_1. That is $y_2-y_1 = D\text{Cos}\theta$ where D is the width of the grating and θ is the angle of incidence of light on the grating which is $\approx$ 30 degrees for a 600 l/mm grating. The width of the grating used for the present work is approximately 58 mm. Simultaneous solution of the expressions for α_1 and α_2 gives $\alpha_1 = 125$ degrees and $\alpha_2 = 55$ degrees. Substitution of the polar formula for a parabola into the above equations and solution for f, the focal length of the parabola, yields f = 17.8519 mm.

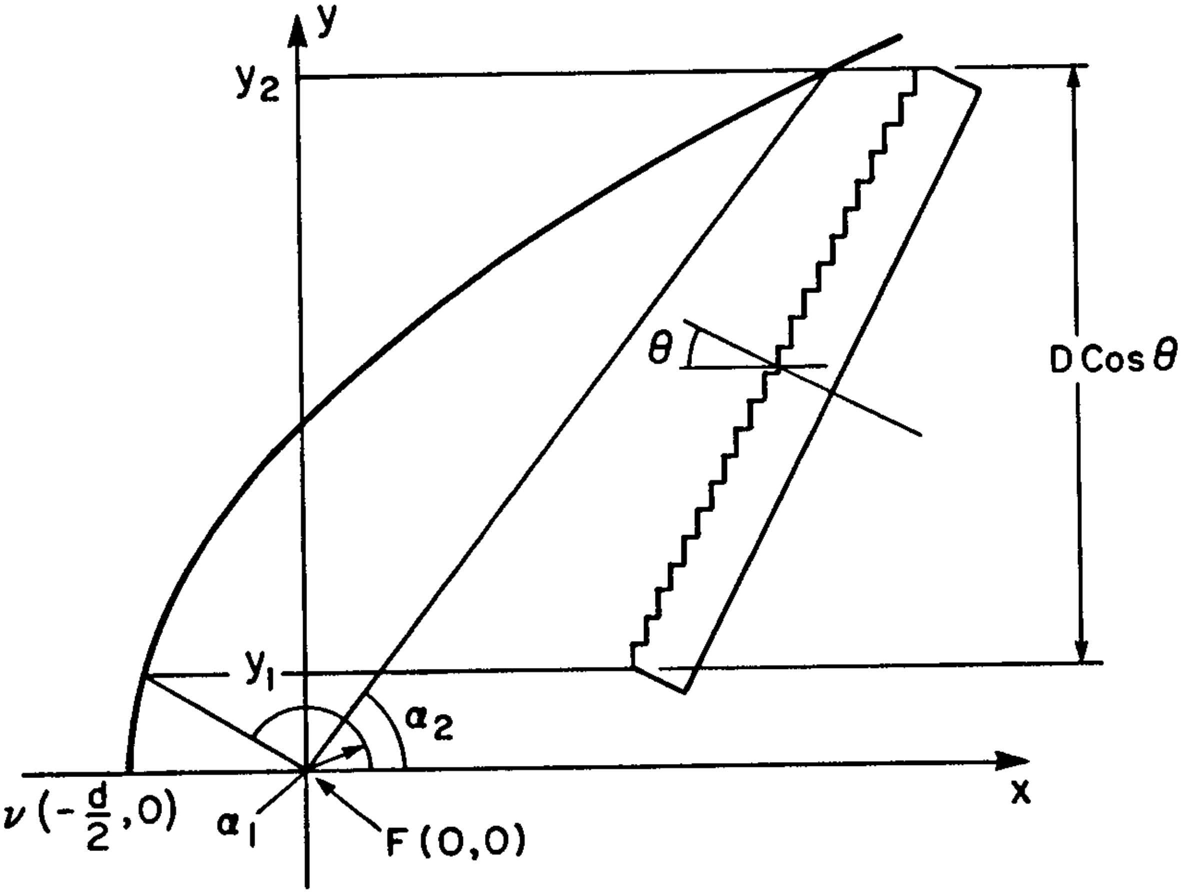

Figure 12. Cross-section of the external grating cavity parallel to optic axis of parabolic mirror.

Before proceeding with construction of an off-axis parabolic mirror the optical aberrations that would be present in the folded external cavity as shown in Figure 12 were determined. The cavity is optically equivalent to a folded Ebert-Fastie[170] monochromator modified to use off-axis parabolic mirrors in a Littrow configuration[171] as originally suggested by Welford[172] where the normal monochromator entrance and exit slit function is accomplished by the small dimension of the laser active region. Ebert-Fastie-Welford (EBW) monochromators are now widely used and their optical properties have been thoroughly studied[173,174]. It has been shown [171] that EBW devices are third order aberration free near the optic axis.

To determine how critical the placement of the diode laser in the right angle cavity of Figure 12 would be in determining its optical aberrations, a computer ray tracing program was written to simulate the cavity. The program name is CAVITY and Appendix F contains the basic language source listing of this program as written for the OGC Prime computer. The program carries out its calculations using geometrical optics ray tracing; no diffraction effects are introduced into the calculations. No aberration effects are introduced for the diffraction grating since gratings in a Littrow configuration are anamorphic[171,175].

The program can perform three functions. First, it can display, with graphical assistance from the OGC Prime Graphics Editor, the simulated off-axis parabolic cavity with optical rays shown. There may be as many rays as are convenient for the program user. Furthermore, the rays may be initialized by either direct specification of their origin and initial direction or a two dimensional Gaussian angular probability distribution with two independent full-width half maximum angles may be specified for a given origin. Figure 13 shows a typical ray-trace output. In the figure, the rays leave from the focal point of the paraboloid with angles perpendicular to the active region of

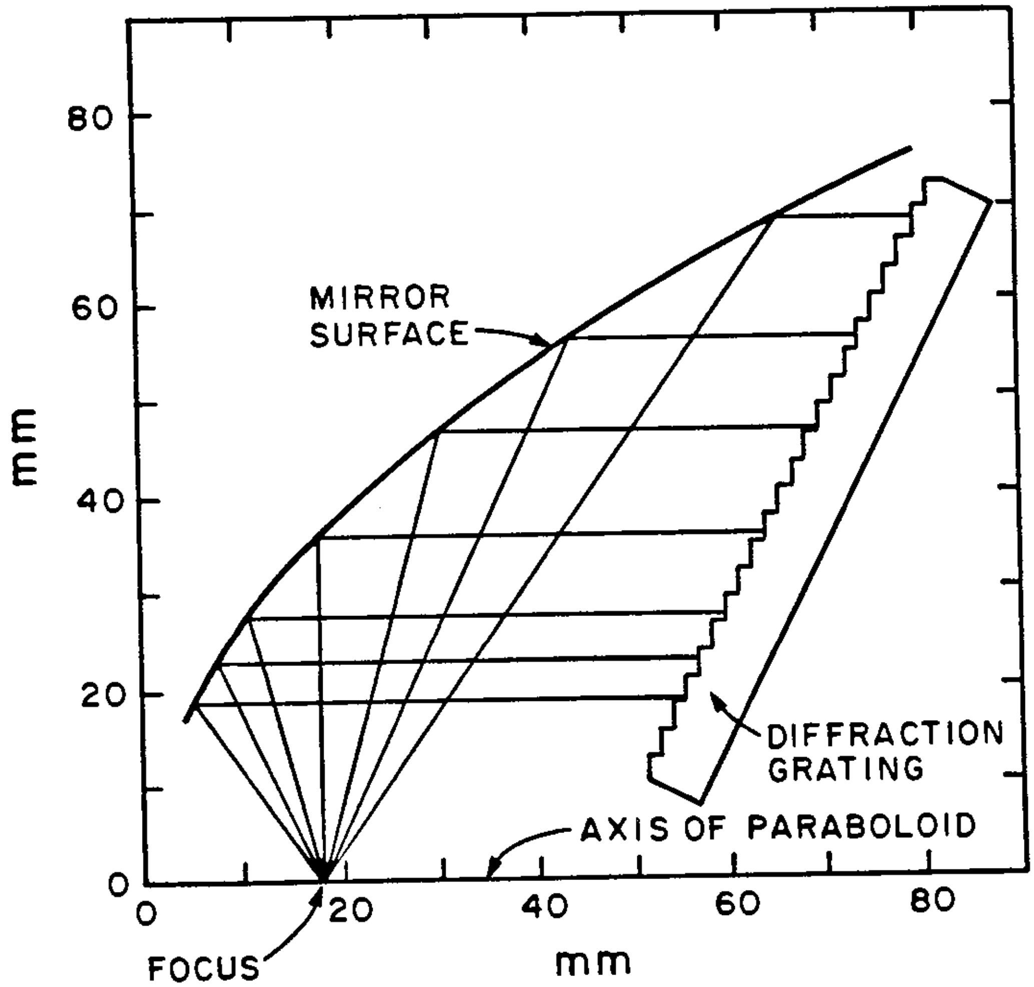

Figure 13. Graphic output from ray trace program CAVITY for the off-axis parabolic external grating diode laser cavity.

±35,±25,±15, and 0 degrees and in the plane of the junction.

Second, the program can calculate and display spot diagrams of the light returned to the diode laser facet. For this latter type of display it is advantageous to be able to determine the spot diagram for laser facets that have been rotated in the plane of Figure 13 or translated. This capability is integral to the program. Here, the Gaussian angular probability distribution provisions of the program may be used to simulate the beam divergence of the diode lasers as described in Section 4. Moreover, the program creates, when used in this mode, statistical data in separate Prime disk files on the beam size perpendicular and parallel to the active region.

Figures 14 and 15 show spot diagrams as generated by CAVITY. The figures represent the returning light spot for 100 rays initially launched from (F,0,0) with Gaussian angular probability distributions both perpendicular and parallel to the active layer. Full width half maximum angles of 70 and 50 degrees, respectively, were used to generate the diagrams. In Figure 14, the laser facet has been translated 15 μm orthogonal to the axis of the paraboloid and away from it, i.e., away from the focal point. In Figure 15 the translation direction is the same but the distance is 5 μm. From these figures it is easily seen that the spot size generated by the returning rays rapidly changes and so alignment along this direction is critical for optimal coupling of the returned light to the diode active layer. A spot diagram generated with the diode laser at the focal point of the paraboloid produced a spot radius several orders of magnitude smaller than the wavelength indicating that the system is aberration free when the diode laser is properly positioned. These calculations show that placement of the diode laser along this direction must be within $\pm 1\mu$m for the aberration induced spot size to be less than the active region thickness. Similar diagrams with the ray origin at (F,±0.050mm,±0.050mm) yield spot radii less than the active region thickness. The

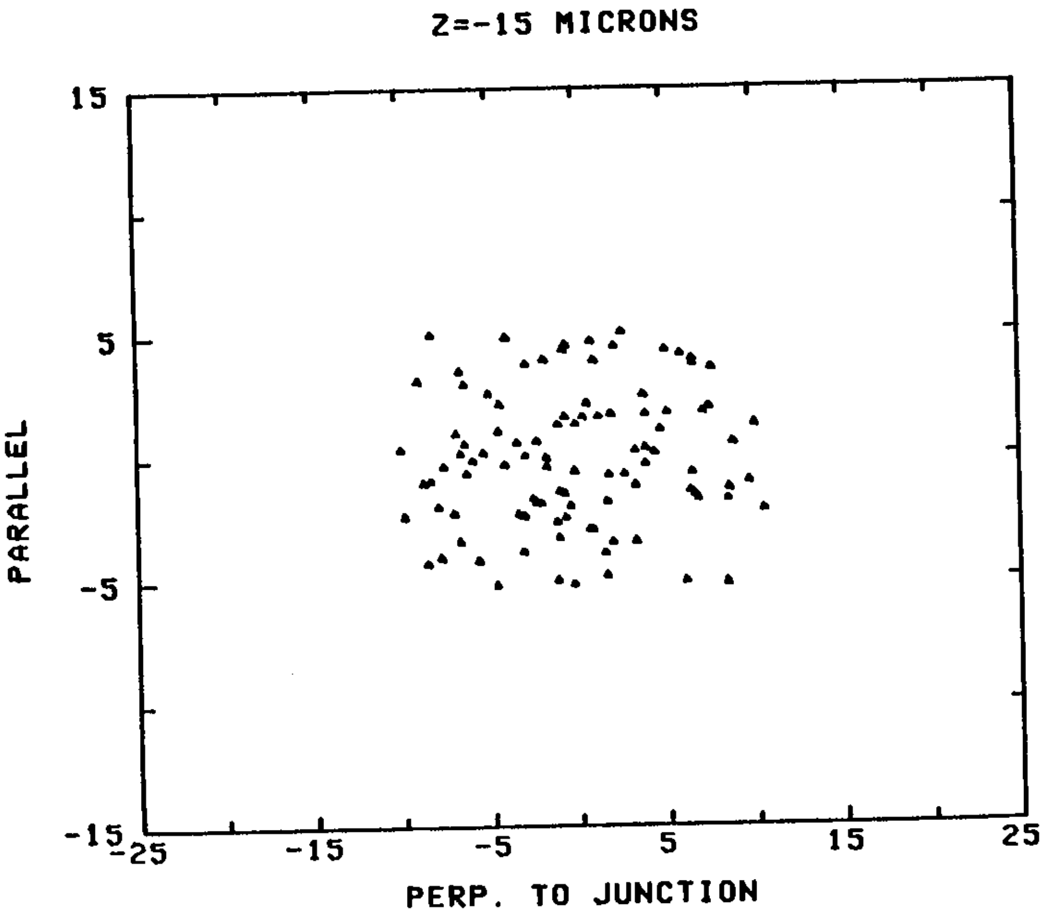

Figure 14. CAVITY generated spot diagram in the plane of the diode laser facet for Gaussian angular probability optical output distributions perpendicular and parallel to the active region. The diode laser is 15 μm from the optic axis of the parabola. The axes units are μm.

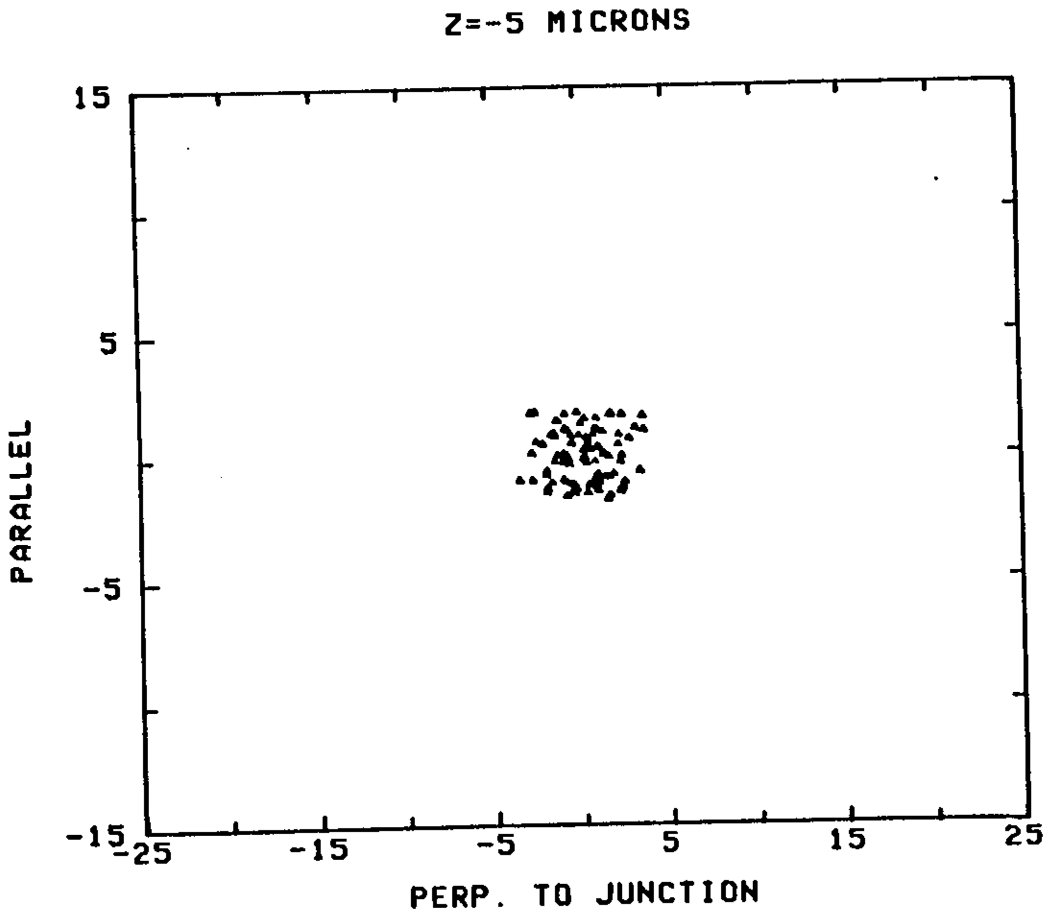

Figure 15. CAVITY generated spot diagram in the plane of the diode laser facet for Gaussian angular probability optical output distributions perpendicular and parallel to the active region. The diode laser is 5 μm from the optic axis of the parabola. The axes units are μm.

external grating cavity diode laser is therefore optically aberration free under the restricted use described here.

Last, the program when operated in the Gaussian angle mode creates a spot diagram in the plane of the grating. Figure 16 is a graphical representation of that diagram. It may be seen from the figure that the illumination at the grating is not uniform and thus diffraction effects are not simply dependent on the grating width. This will be discussed more fully in the next section.

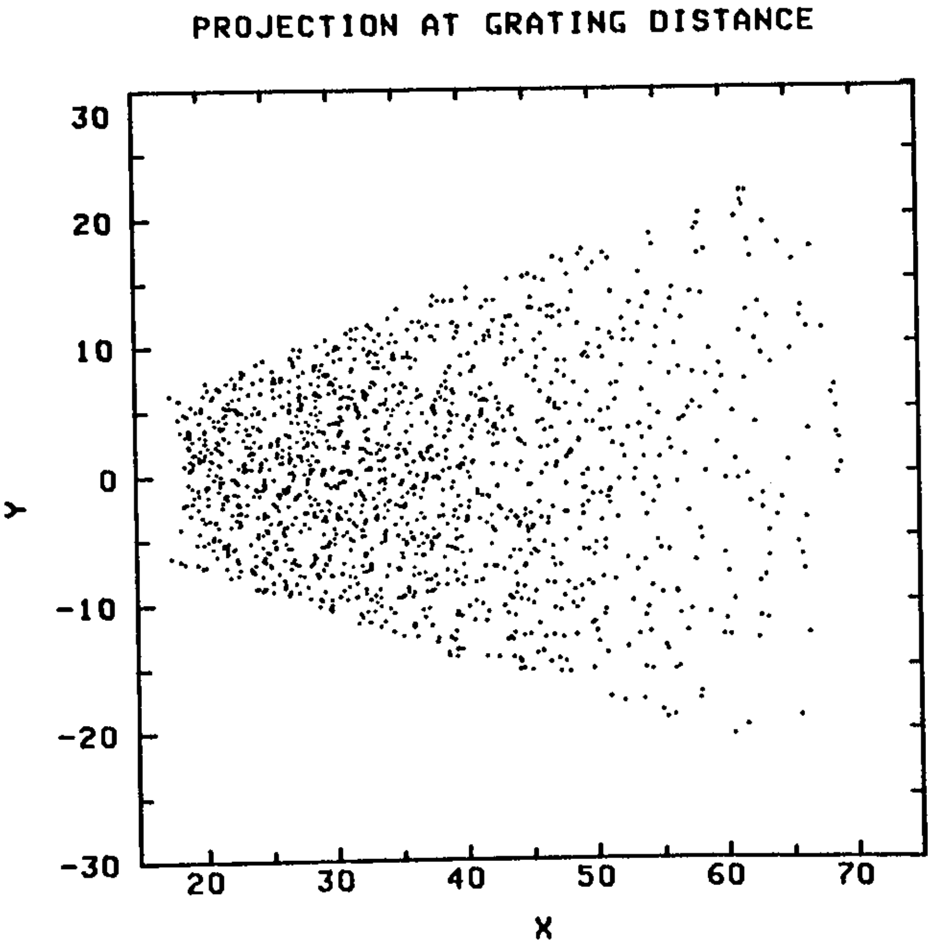

Figure 16. CAVITY generated spot diagram in a plane orthogonal to the optic axis of the parabolic mirror and at the position of the grating. The axes units are mm.

7. AN OFF-AXIS PARABOLIC MIRROR EXTERNAL GRATING CAVITY DUAL DIODE LASER SOURCE

The preceeding sections have presented the requirements for the optical design of an external grating cavity diode laser source for a DIAL methanometer. This section describes the construction and performance of such a source. Figure 17 shows the physical realization of the off-axis parabolic cavity described in Section 6 and schematically shown in Figure 13. The cavity includes a diamond-machined off-axis parabolic mirror, a diffraction grating mounted on a gimbal mount, a motorized micrometer for positioning the grating, a mount for two diode lasers, and a XYZ translation stage for positioning of the two diode lasers in the cavity. Each of the cavity components is described below.

Figure 18 gives a view of the off-axis parabolic mirror. The drastic curvature of the diamond machined surface is evident from the figure. Figure 19 is a reproduction of the technical specification drawing for the mirror given to Pneumo Precision, Inc. for machining in March 1983. The drawing was computer generated using the OGC Prime Graphics Editor. Included with the drawing are several technical requirements. In particular, the mirror is fabricated in aluminum with a 17.852 mm focal length as was suggested in Section 6. The surface figure is specified as $\lambda/2$ at a wavelength of 633 nm which is equivalent to $\lambda/5.2$ at 1.65 μm; the RMS surface roughness is specified to be 150 Angstroms or less.

The finished mirrors were tested against the specifications in tests at Pneumo Precision and at OGC. The focal length and surface figure were examined at Pneumo Precision using optical interferometric techniques and shown to meet specifications. Acceptance tests conducted at OGC included measurements of the mirror reflectivity and total integrated scattering. Reflectivity at 45° incidence with 633 nm He-Ne laser light

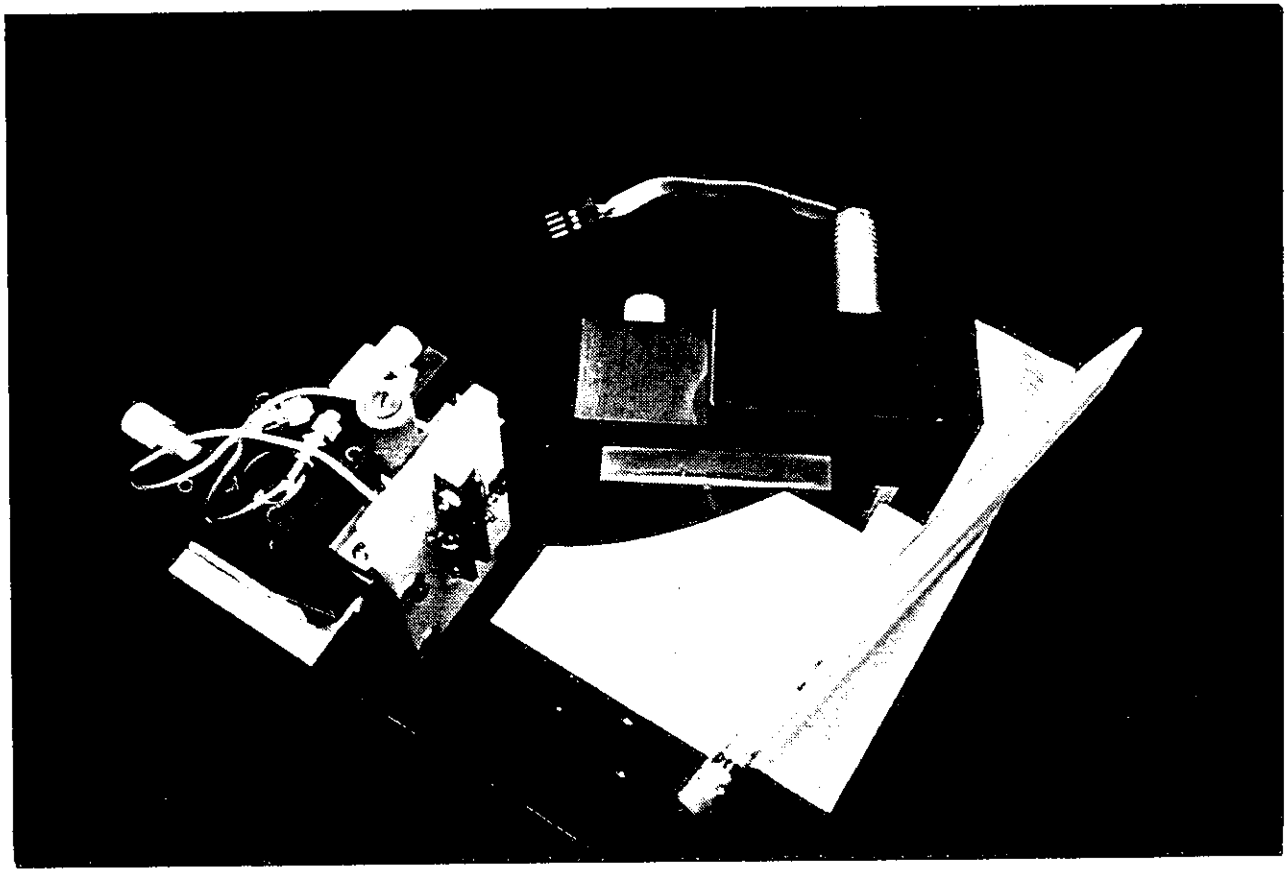

Figure 17. The dual diode laser external off-axis parabolic mirror grating cavity source. Shown are the off-axis parabolic mirror, the grating and its positioner, and the dual diode laser mount and its positioner.

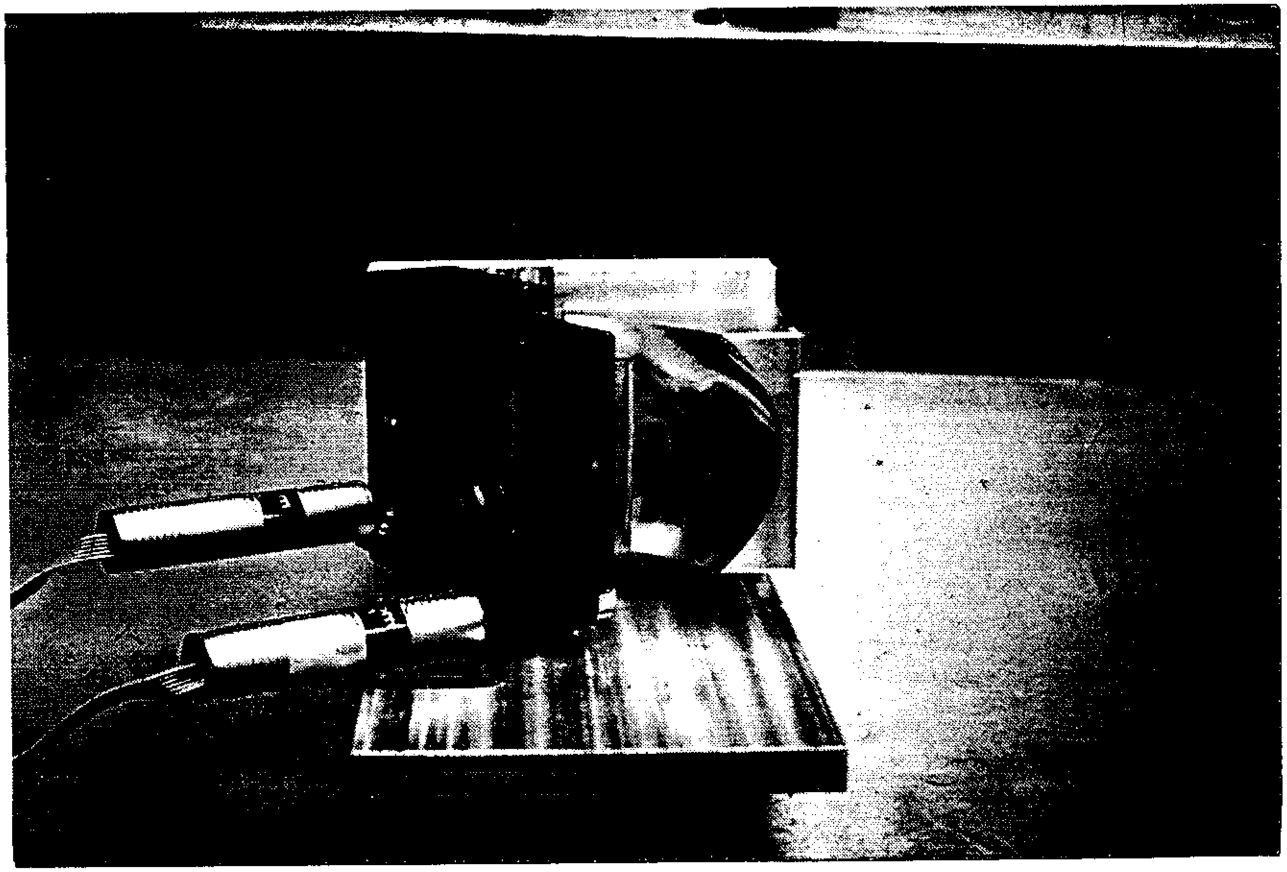

Figure 18. The off-axis parabolic mirror with the diamond-machined surface presented.

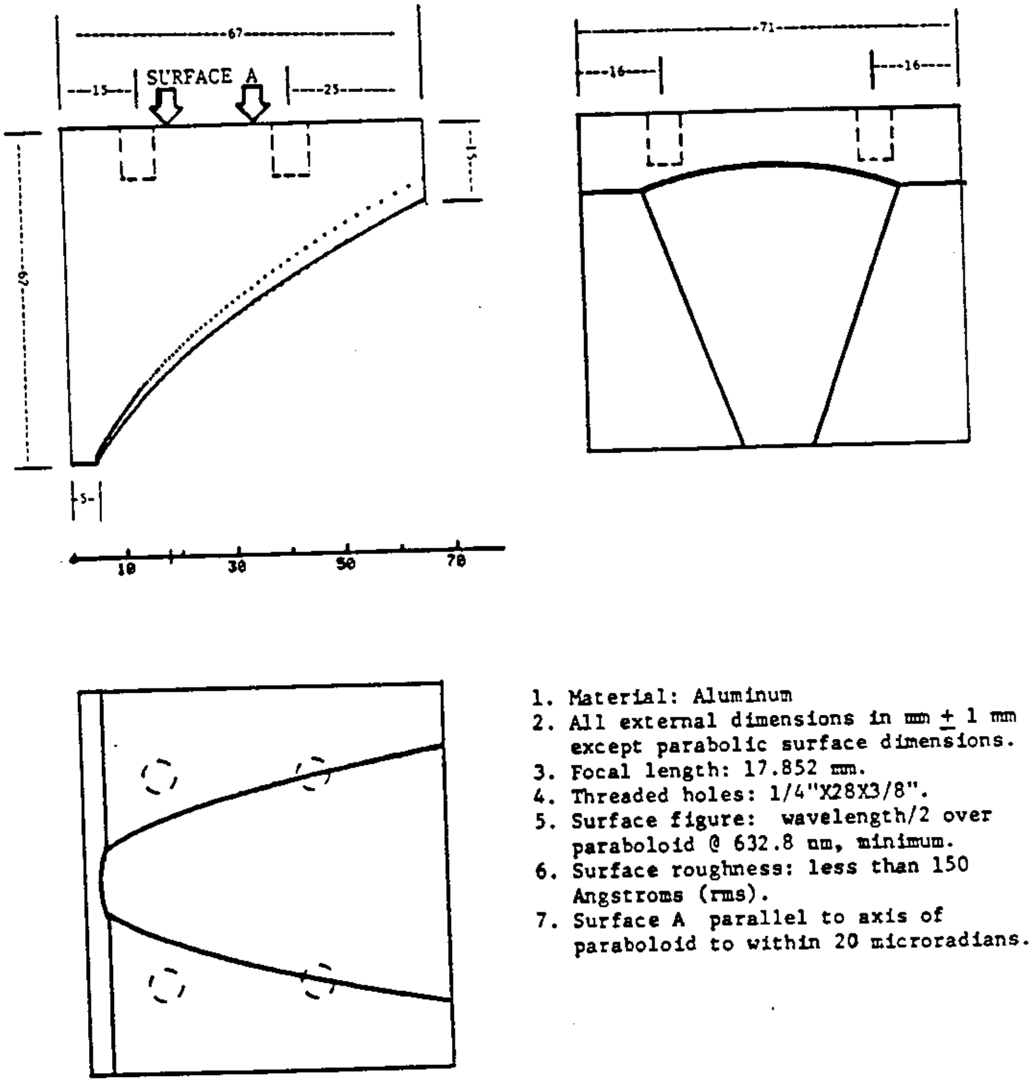

1. Material: Aluminum
2. All external dimensions in mm ± 1 mm except parabolic surface dimensions.
3. Focal length: 17.852 mm.
4. Threaded holes: 1/4"X28X3/8".
5. Surface figure: wavelength/2 over paraboloid @ 632.8 nm, minimum.
6. Surface roughness: less than 150 Angstroms (rms).
7. Surface A parallel to axis of paraboloid to within 20 microradians.

Figure 19. Technical specification drawing for mirror of Figure 18.

was measured to be 87% for the sum of the specularly reflected spot and the scattered light. Figure 20 shows a trace of light output versus angular position for one location on the mirror. In the figure, the small fluctuations to the sides of the center spot are scattered light and represent less than 5% of the total reflected light at 633 nm. The total integrated scattering (TIS) is inversely proportional to the square of the wavelength through the relation[176]

$$\mathrm{TIS} = \left[\frac{4\pi\delta\cos(\theta)}{\lambda}\right]^2 \tag{23}$$

where δ is the RMS surface roughness, λ is the wavelength, and θ is the angle of incidence. Using Equation 23 and the measurement at 633 nm the TIS at 1.65 μm is calculated to be less than 1%. Coupled with the 87% reflectivity mentioned above and the higher reflectivity of aluminum at 1.65 μm, a specular reflectivity of 96% is calculated. The RMS surface roughness, calculated from the measured values for TIS, angle of incidence, and wavelength, is 160 Angstroms, which is within the measurement uncertainty of the 150 Angstrom specification.

The diffraction grating is a 600 l/mm replica fabricated with aluminum on epoxy on glass. It is blazed at $29^\circ\,41'$ for use in the first order at 1.6 μm in a Littrow configuration. Nominal reflectivity at 1.65 μm into the first order is 70%. The grating holder is an Ardel Gimbal 20-25 series mount.

There are three means by which the grating and gimbal mount could be automatically rotated and electronically controlled to ensure proper wavelength selection. The first method involves using piezoelectric translators attached to manual micrometers. This technique suffers from the high voltages ($\approx$ 1 kV) necessary to drive piezoelectric stacks over distances on the order of 1 μm. The second method involves use of micro-

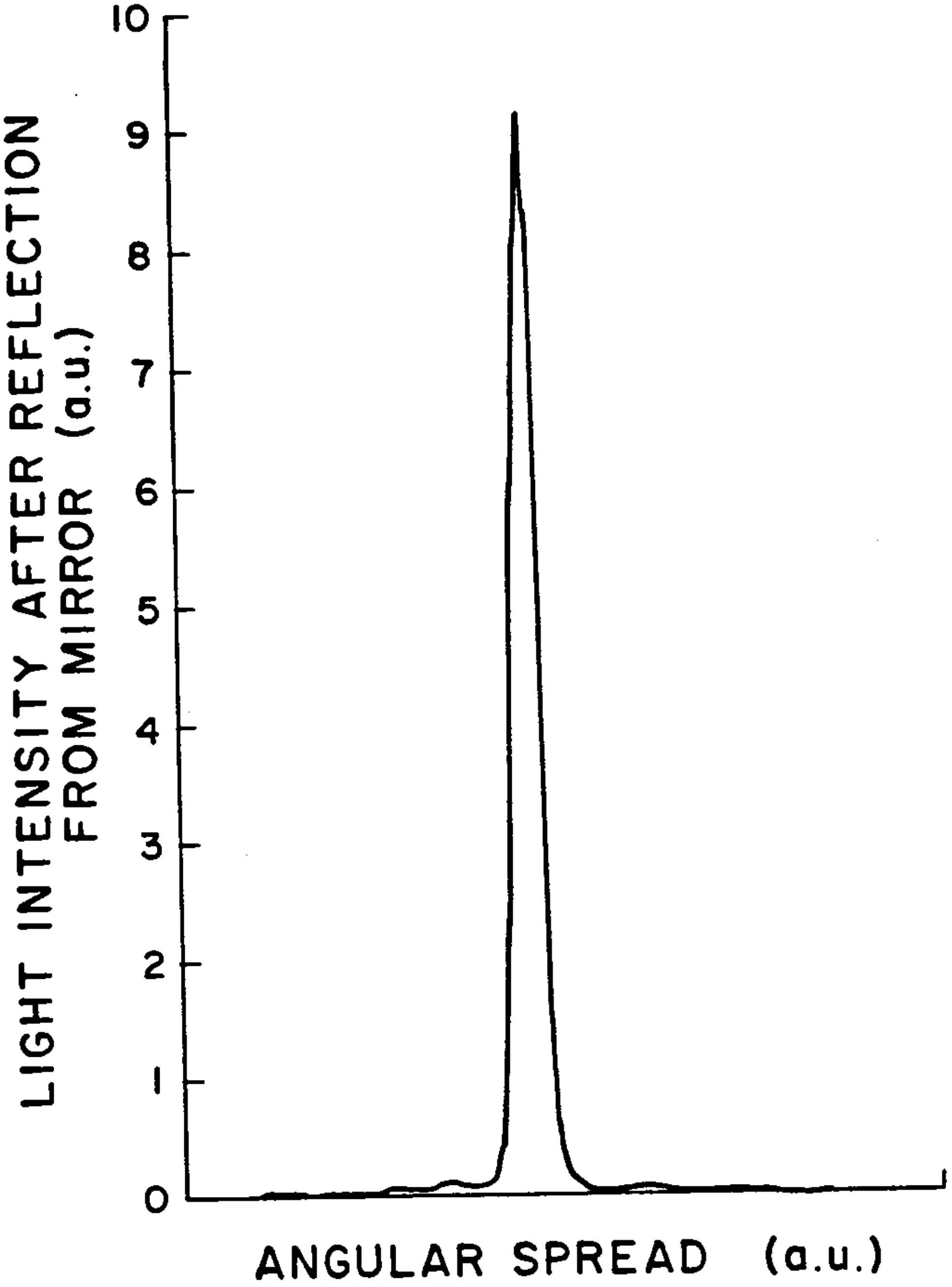

Figure 20. Light reflected from surface vs. scattered angle for the mirror of Figure 18.

stepped stepper motors. The stepper motor technique is similar to that using DC motors with optical shaft encoder readout however the stepper motors are typically more bulky. The third method, and the one used for this project, entails use of DC motor driven micrometers with optical shaft encoder position readout.

The motorized micrometer shown in Figure 17 is an engineering run Ardel Kinamatic MotorMike^{TM} Model 17213 with position readout capability. Position readout is achieved via TTL level electrical pulses from an optical shaft encoder and has a linear travel precision of 0.1 μm with a backlash limited accuracy of approximately 3 μm. A 0.1 μm position precision is equivalent, through the 1 inch lever angle of the gimbal mount, to a 4 microradian angular position precision. Such precision is six times the angular resolution required as determined by Equation 22.

Double pulse LIDAR measurements, with an interpulse temporal separation of less than 1 ms, were shown in Section 5 to be advantageous from a signal processing standpoint. In Section 6, the concept of using two diode lasers in the same external grating cavity was introduced as a means of achieving a short interpulse period where the two lasers were placed at slightly different angles to the diffraction grating thus producing slightly different lasing wavelengths. The external cavity displayed in Figure 17 contains two such diode lasers in a brass mount.

Figures 21 and 22 are perspective drawings of the dual diode mount. Figure 23 is a close-up photograph of part of the same mount. In the figures, two lasers are shown to be positioned with their p contacts adjacent and contacting a gold strap conductor. The strap has approximate dimensions of 25 μm by 300 μm by 1 cm and was machined at OGC from 25 μm thick commercial Au foil with a frequency doubled Nd:YAG laser. The n contacts of the lasers rest on gold plated diamond heat sinks[177-181]. Diamond heat sinks were chosen for this application because of their flat surface (cleaved planes)

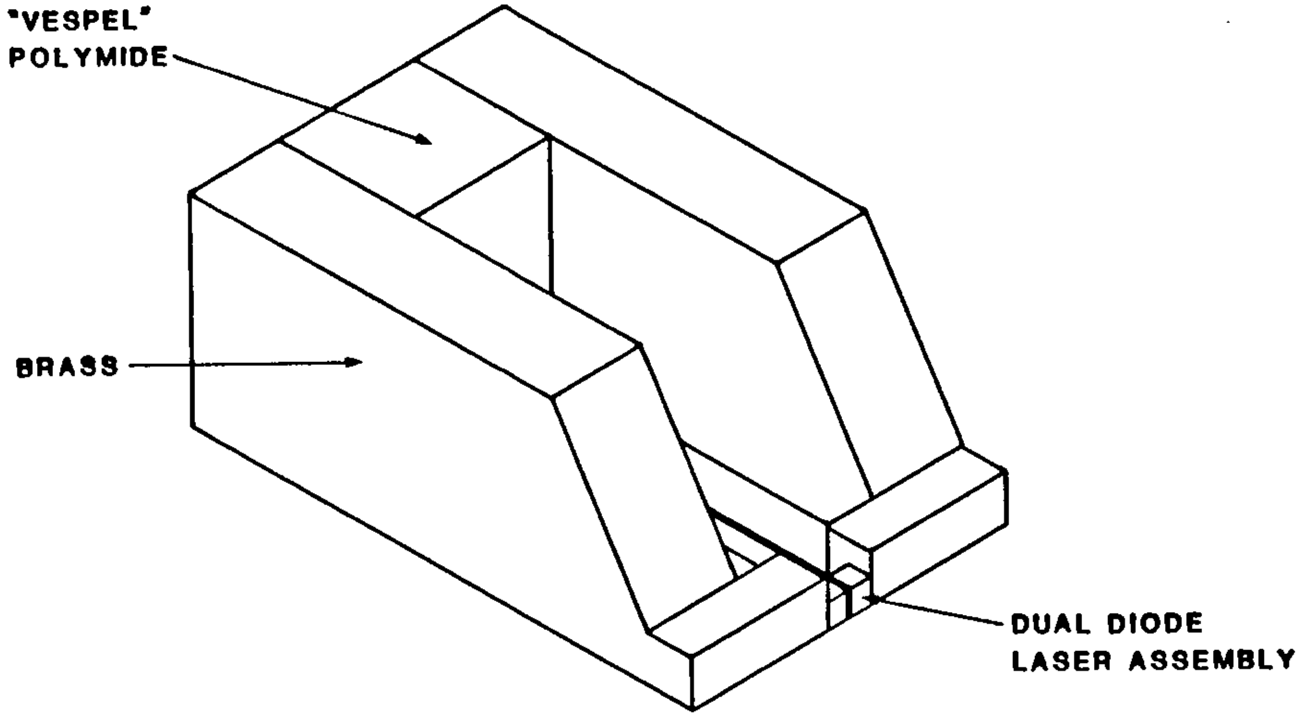

Figure 21. Perspective drawing of the dual diode laser mount.

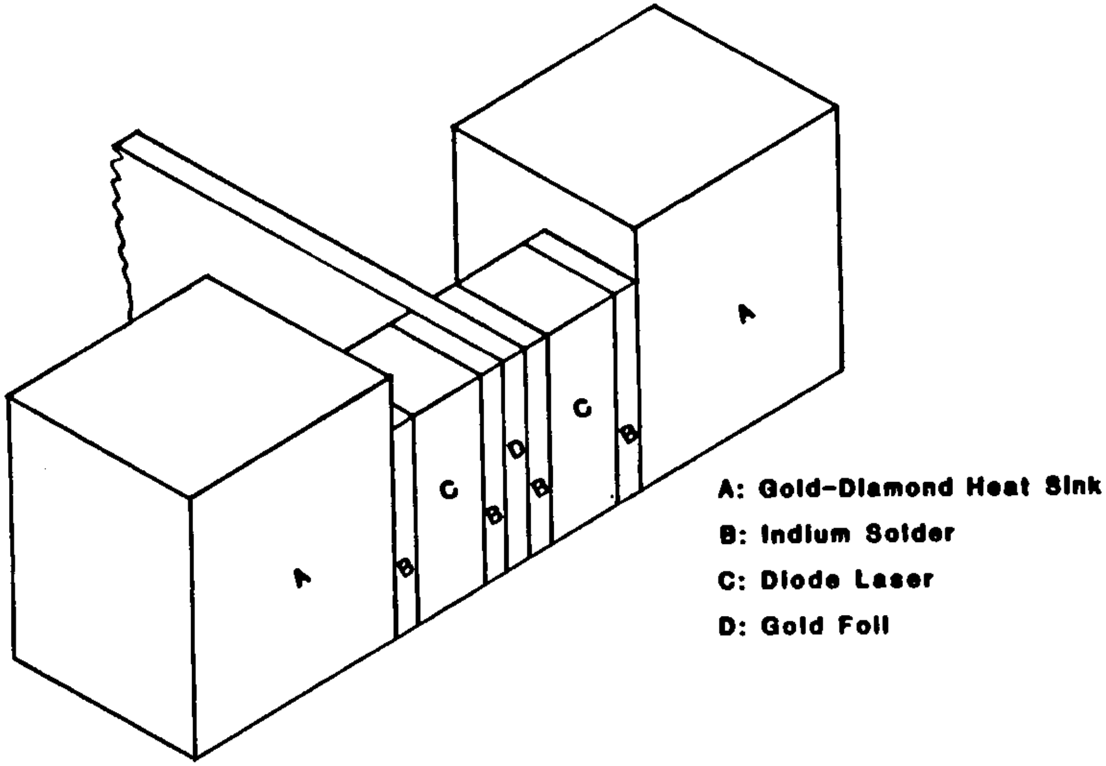

Figure 22. Detail drawing of the dual diode laser mount. Shown are the diode lasers and their heat sinks and indium bonding pads.

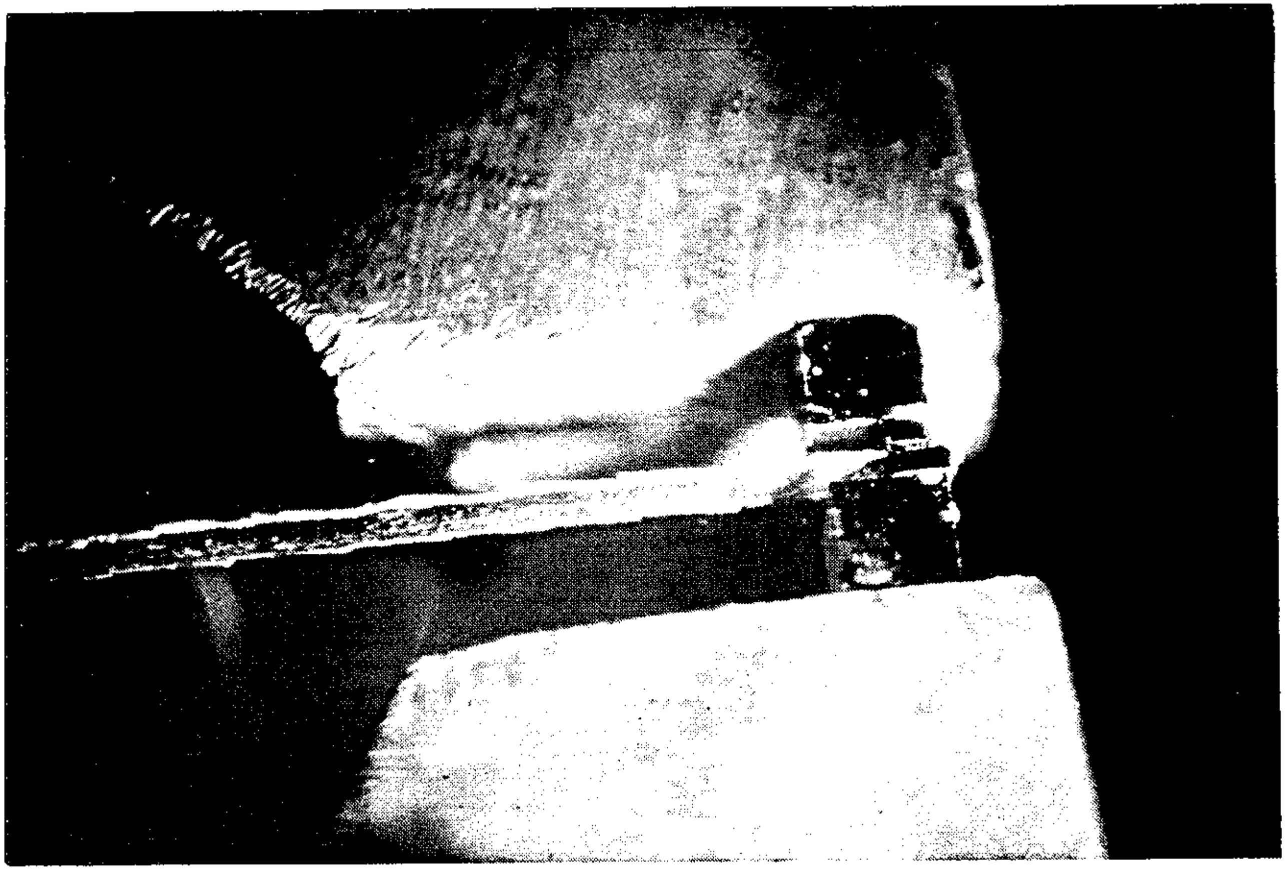

Figure 23. Photograph of that portion of the dual diode mount shown in Figure 22.

and parallel faces ($< 10'$) and because the thermal conductivity of Type IIa diamond[178] is five times that of copper at room temperature. The lasers were hand positioned in the mount using a special function jig which featured an integral optical flat to ensure optical alignment of the diodes.

The aberrations in an off-axis parabolic grating cavity were discussed in Section 6. It was shown there that placement of the diode laser, regarding optical aberrations, was critical only along the the optic axis of laser. The positioning stage shown in Figure 17 is a Klinger, Model MR-50, micropositioning device featuring manual micrometer adjustment in a plane parallel to the axis of rotation of the paraboloid and manual differential micrometer adjustment orthogonal to the axis. The former adjustments have a sensitivity of 1 μm while the latter has a sensitivity of 0.1 μm. This precision is necessitated by the aberration requirements discussed in Section 6 and is achieved with an enhanced version of the standard MR-50. Before the diode lasers were mounted in the dual diode mount and installed in the external cavity, they were AR coated to decouple their light output from their normal cavity modes.

Dielectric thin films are often used for antireflection coatings on semiconductor devices. A dielectric film with the index of refraction and thickness prescribed by Equations 19 and 20 of Section 6 has a theoretical air-laser reflectivity of near zero. There are many methods[182, 183], including thermal evaporation, sputtering, plasma deposition, and chemical vapor deposition, by which such a coating might be applied to a diode laser. However, most AR coatings for light emitting diodes and diode lasers that have been reported in the literature[184-187, 140, 142, 156] have used coatings thermally or e-beam evaporated from SiO, although e-beam evaporation of ZrO_2, [143] and sputtering of Si_3N_4[188] among other techniques have also been successful. Because of the large amount of information available about thermally evaporated SiO and its properties, this method of creating AR coatings was used on the present project.

The physical properties of evaporated SiO coatings have been well studied[189-192]. The index of refraction of SiO rapidly evaporated (> 10 Angstroms/second) under vacuum conditions of less than 1 x 10^{-5} torr has been shown to be approximately 1.85 with negligible absorption near a wavelength of 1.65 μm. The effective index of refraction for the diode lasers used in the present project has been previously shown[18] to be 3.52. Since the square root of 3.52 is 1.88, SiO can be seen, through Equation 19, to be a good AR material for these lasers.

There are two methods to achieve an optimum index-thickness combination for a single layer film. One method is to calculate [163,193,194] the optimum index and thickness from the properties of the particular diode laser using guided wave theory and then to create those properties for the coating. This method requires complete knowledge and strict control of the coating process and has recently been put into use to sputter Si_3N_4 onto laser facets[188]. The second, and much simpler, method [186] uses a substance with approximately the right index of refraction as given by Equation 19 and then monitors the reflectivity looking for a minimum as the coating thickness increases. This technique was used on this project.

The SiO AR coatings were deposited from a Drumheller oven, Electronic Space Products, Inc. (ESPI) Part No. ESPI KVAC-477, using evaporation grade SiO, ESPI K4698C, at a background pressure of 10^{-7} to 10^{-6} torr. Figure 24 shows the setup for monitoring the reflectivity in real time. In the figure, the current pulser drives the diode laser at a point below lasing threshold so that the diode emits only spontaneous emission. The light pipe shown in the figure carries light from the vacuum chamber to a Ge detector and preamp outside the chamber. The resultant signal was synchro-

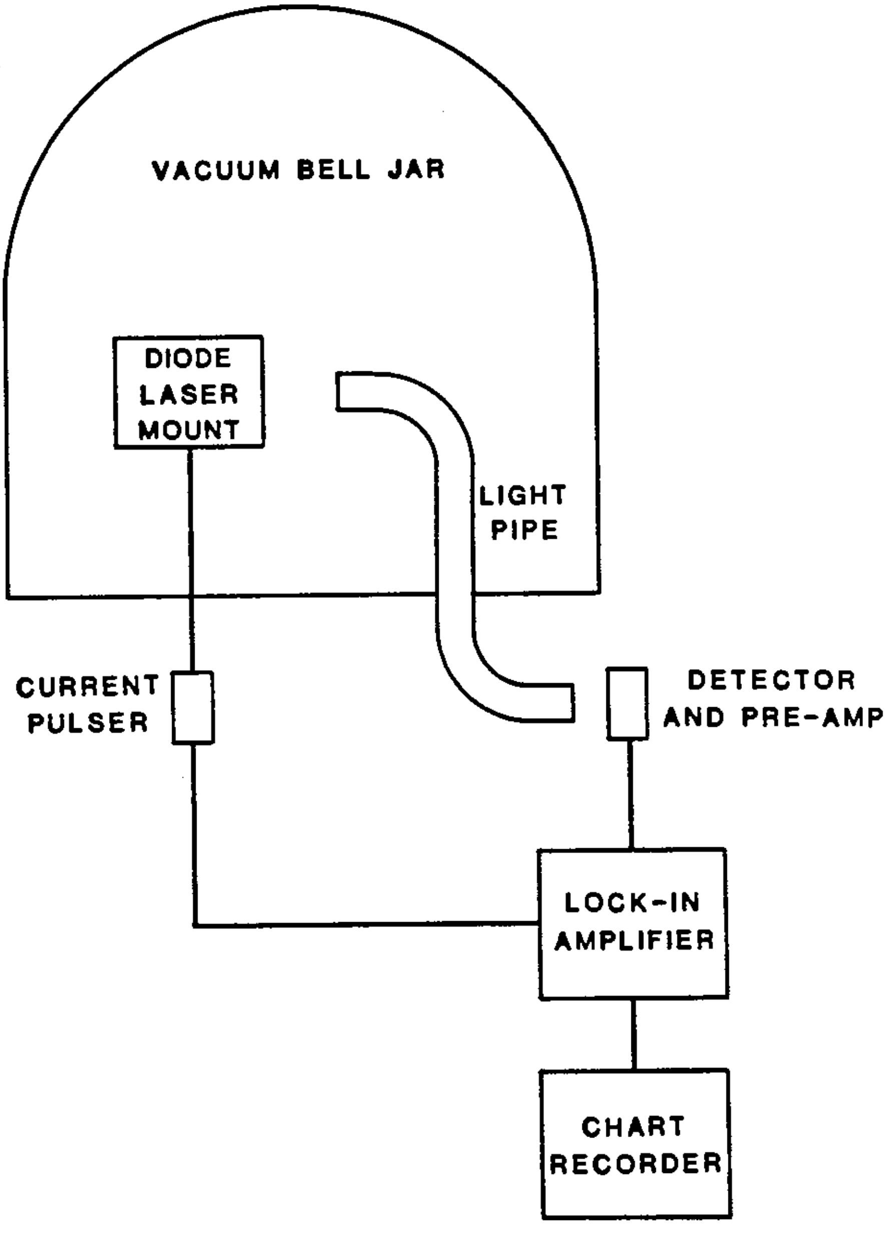

Figure 24. Setup for in situ monitoring of the antireflection coating thickness during deposition.

nously detected with a lockin amplifier, EG&G 5101, at the pulse repetition rate. The output from the lockin amplifier was recorded with a stripchart recorder. As the SiO coating was deposited the amount of light escaping the diode laser facet varied thus giving a record in real time of the coating efficiency.

Figure 25 shows the recorder output for a test AR coating deposited on a Laser Diodes Labs Model LCW-5 continuous wave 5 milliwatt optical output diode laser. The recorder plot is light output versus time. For this run a sine-wave generator was substituted for the pulser since the lockin amplifier intrinsically responds more efficiently to such a modulation signal. In the figure, each peak in light output indicates an odd multiple of quarter wavelengths for the coating thickness, while the troughs indicate a half wavelength thickness. The coating rate is approximately 16 Angstroms/second. The overall trend downward with time is caused by increased scattering and absorption in the coating. The after-coating reflectivity may be estimated from

$$I_A = I_o\left(1-R_A\right) \tag{24}$$

and

$$I_B = I_o\left(1-R_B\right) \tag{25}$$

where I_A and I_B are the laser light outputs after and before coating, respectively, I_o is the light intensity inside the facet, and R_A and R_B are the facet reflectivities after and before coating. Equation 25 may be divided into Equation 24 to solve for R_A using $R_B \approx 0.32$ for the LDL laser and the $\lambda/4$ peak in the figure. The resultant value of R_A is 0.10 and would have been lower had not the device already had a commercial $\lambda/2$ coating on its output facet.

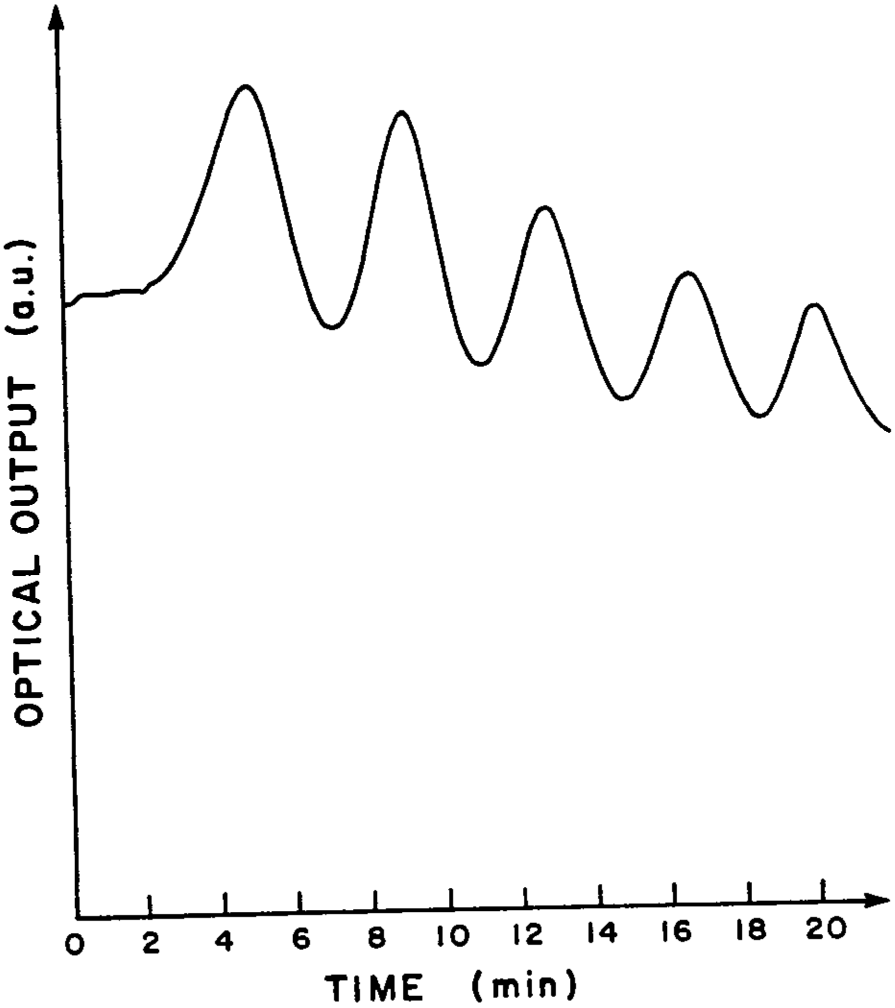

Figure 25. Optical output vs. time during deposition of a SiO antireflection coating on a Laser Diode Labs Model LCW-5 diode laser. The evaporation process was stopped at a 3 λ coating thickness.

Figure 26 shows an example of a chart recorder trace for an AR coating applied to one of the diode lasers used in the present project. In this case, the evaporation process was terminated at a coating thickness of $\lambda/4$ to achieve minimum absorption and scattering. Calculation of the residual reflectivity in the manner presented above yields $R_A \approx 1$ %. After the coating was applied to the laser, which had a lasing threshold of 2 Amps before coating, it did not lase at currents greater than 6 Amps. Figure 27 shows a typical before- and after-coating light output versus drive current curve. In the figure, the lower curve is the light output from the uncoated facet after AR coating. The effect of the AR film on the lasing threshold is obvious from the figure.

The first attempts at AR film deposition were not as successful as those represented in the figures above: the early films tended to peel from the diode laser facet along lines parallel to the active region. The probable cause of this defect was determined to be anisotropic stress[195] in the SiO film. Rotation of the evaporation angle of incidence to the laser facet from normal to 40 degrees off-normal eliminated the peeling problem. Subsequent film depositions exhibited another defect in which the films peeled off in narrow bands on the output facet along the facet intersection with the epitaxial layer interfaces. This type of defect occurred during prolonged operation in the external cavity and was attributed to localized heating at the interfaces, possibly due to nonradiative carrier recombination at those sites. Careful chemical pre-cleaning of the diode laser facets along with argon glow discharge sputtering of the facet just before evaporation eliminated this coating defect.

The cleaning and sputtering process was conducted as follows. After mounting of the diode lasers in their dual diode mount, the mount was ultrasonically washed in electronic grade acetone. After the washing was completed the mount was dried in a nitrogen jet. The mount was then placed in the evaporator and exposed for several minutes

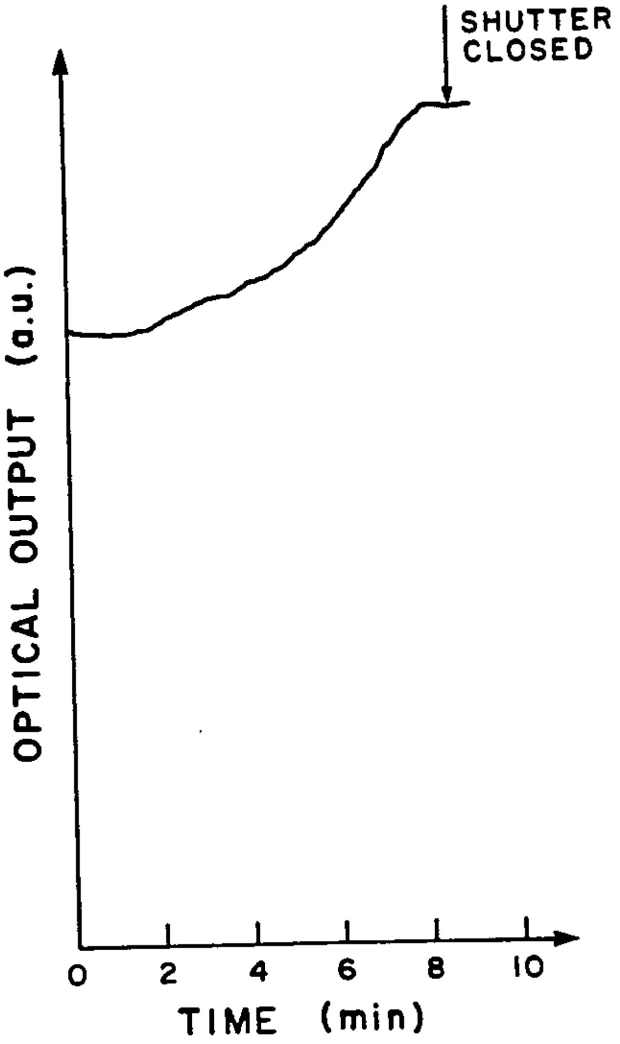

Figure 26. Optical output vs. time during deposition of a SiO antireflection coating on an InGaAs/InP diode laser. The evaporation process was stopped at a $\lambda/4$ coating thickness.

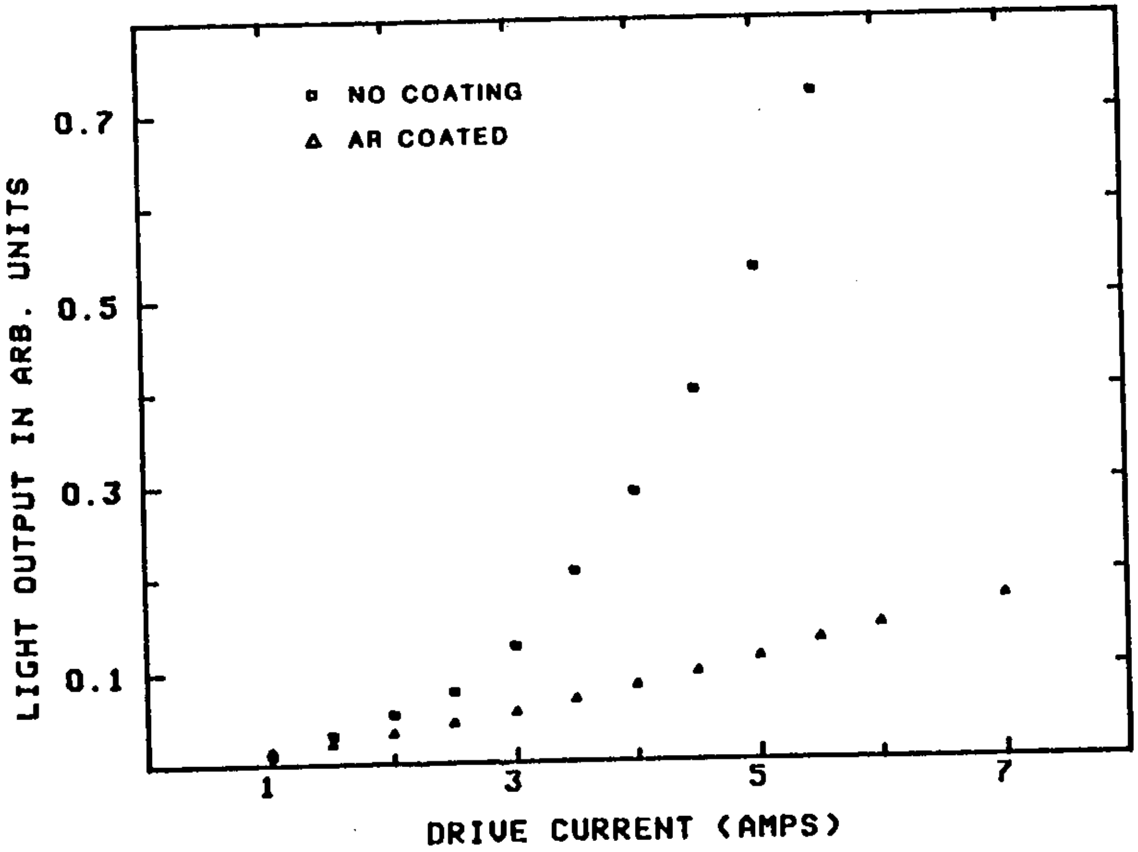

Figure 27. Optical output vs. drive current for an InGaAs/InP diode laser before and after coating with SiO.

to Hg discharge- generated ozone to break down[196] any residual hydrocarbons from the acetone wash. Then the vacuum chamber was evacuated to a background pressure of 500 mtorr of argon and glow discharge sputtering[197] of the facet was achieved by placing the diode laser mount near the aluminum anode of a 2 mAmp/cm^2 current density discharge for several minutes. The discharge and subsequent film deposition were conducted in the presence of 200 mW of argon ion 514.5 nm laser light focussed on the facet. The laser light helped to keep the facet clean by heating it and by providing photons to the surface with energy greater than the binding energy of water vapor and hydrogen, the most common contaminants in high vacuum environments.

We now describe the electronic attributes of the dual diode laser cavity's wavelength controller and its current pulser. First, the wavelength controller will be described by paraphrasing and summarizing its manual, "Dual Diode Cavity Wavelength Controller: Instrumentation for Automatic Laser Tuning" where a definitive description of the controller, including hardware schematic diagrams and software code may be found. Second, the dual diode laser pulser will be discussed.

The purpose of the wavelength controller is to cause automatic positioning of the grating angle relative to the external cavity so that maximum absorption in methane is achieved. The control process is designed to be a turn-key operation that is enabled whenever the diode laser electronics are turned on. Figure 28 is a block diagram of the physical layout of the controller and its associated hardware. The hardware used in the controller consists of two circuits: the MotorMike (MM) motor control box and the analog signal board. Both of these connect to an Intel SBC 80/20 single-board computer.

The motor control box allows both forward and backward movement of the MM which positions the diffraction grating. It uses two of the TTL-compatible outputs from

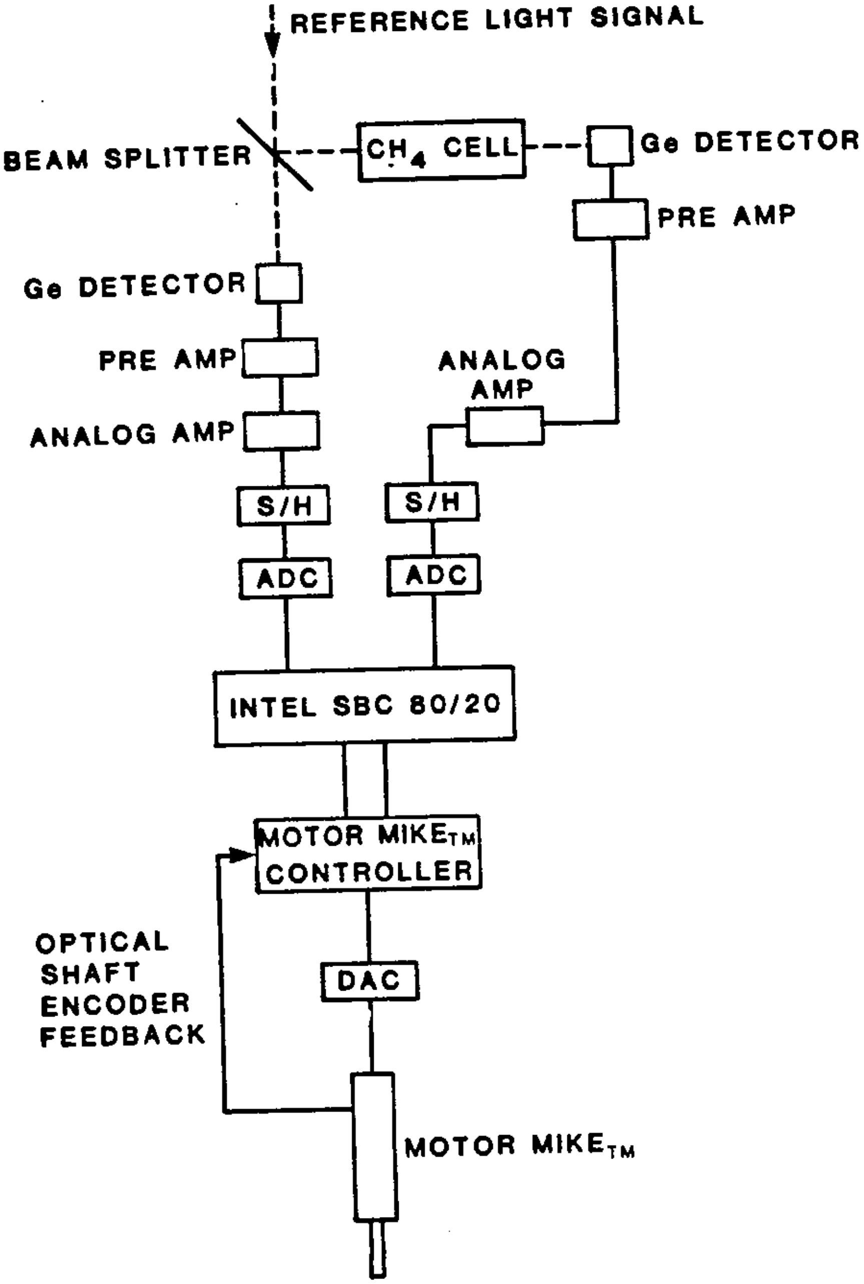

Figure 28. The wavelength controller and its associated hardware.

one 8255 Programmable Peripheral Interface (PPI) which is on board the 80/20. One output bit determines the motor direction while another bit turns the motor on and off.

The second circuit consists of analog signal conditioning amplifiers along with sample-and-hold (S/H) and analog-to-digital conversion (ADC) chips. This circuitry is constructed on a separate module which plugs onto one of the PPI edge connector ports. Two identical circuits are located on the module. The first circuit is for the reference optical signal and the second is dedicated to the signal from the optical power that has passed through a methane cell.

The signals are then conditioned. First, the reference and methane cell germanium photodiode (Judson Infrared Model J-16) output is amplified using commercial preamps (Judson Infrared Model 700). The output from the preamps is then conditioned by a two-stage amplifier. The first stage is AC-coupled and noninverting with a gain of 12. This gain, coupled with that of the preamplifier, allows only a small portion of the optical output power to be used for this measurement. The next stage has a gain of 3 and includes an offset adjustable input. The offset allows the operator to calibrate a zero signal value while the light to the photodetectors is blocked.

The conditioned signals then go to sample-and-hold chips. These chips, as well as the following analog-to-digital converters, are controlled by the outputs from a dual monostable pulse generator which in turn is controlled by the TTL output of signal B from the diode laser pulser. The monostable pulse generator pulse widths are independently adjustable. This allows the operator to set the S/H-ADC operation to occur at the maximum for each photodetector pulse thus compensating for any difference in the time constants of the two channels. The rising edge of the pulse causes the S/H amplifiers to start sampling and sets up the ADCs. The falling edge of the pulse then causes the S/Hs to hold the peak value and simultaneously starts the conversions by the ADCs. The signal pulse from the optical detectors and their preamps and amps occurs about 2 microseconds after the laser fires. After the ADC, the computer, which has been interrupted by the same TTL output B from the laser pulser, acquires the digital data.

The controlling software is written in assembly code and is stored in EPROMs. A complete listing of the software code is available in the controller manual. The code is located by functional blocks on separate EPROMs as follows. The first block contains power-up and interface chip initializations. The second block includes several mathematical and setup routines called by the main operating system. The third EPROM includes several routines. One routine does 64 ADCs for each laser and then returns the ratio of the sums. Another scans the MM over a predetermined wavelength range seeking the minimum transmission through the methane cell. Other routines on this EPROM back up the MM to a predetermined point for rescanning of wavelength and output to a monitor raw signal values from each laser.

The main operating program contains the following functions:

1. Back up the MM 1024 counts (5.7 nm or 21 cm^{-1}).
2. Scan forward 2048 counts (11.5 nm) moving the MM 3 or 4 counts (≈ 0.02 nm) each time saving the position where the minimum transmittance through the methane reference cell occurs.
3. Back up 128 counts beyond where the minimum was found.
4. Scan forward 256 counts, moving about 2 counts each time and again determine the location of minimum transmittance.
5. Compute a threshold value above the minimum value which will be looked for on the final scan. This has been implemented as 1/16 of the difference between the maximum and minimum ratios found during the first two scans but may be arbitrarily set.

6. Back up 64 counts beyond the most recently found minimum.
7. Scan forward, moving 1 count each time, until the threshold value is found.

The schematic diagrams for the dual diode current pulser are shown in Figures 29 and 30. Figure 29 shows the pulser timing circuitry. Figure 30 displays one channel of the current driver.

The timing circuitry shown in Figure 29 has several notable features. The pulse repetition frequency may be set with the pulse rate potentiometer for interpulse periods of 0.1 to 1 ms. Another potentiometer controls the pulse width with a range of 100 to 300 ns available. An external enable (ground to disable) connector is provided to remotely turn the pulser on or off. Other external connection signals include a square wave synchronization signal at the PRF rate and TTL level pulse outputs, A and B, coincident in time with the laser current pulses. These three synchronization pulses allow for timing of external devices. Use of Pulse B was described above.

The diode driver shown in Figure 30 also has several notable features. The laser diode may be driven with a 0 to 10 Amp current pulse by varying the laser diode power voltage from 0 to $\approx$ 40 volts. This 4 Ω effective dynamic resistance compares favorably with the commercial diode laser pulsers, Laser Diode Labs (LDL) Model LPC-23C, used in the early parts of this study. The LDL pulser had an effective resistance of $\approx$ 30 Ω thus needing $\approx$ 300 volts to drive the a diode laser with 10 Amps. The improvement achieved is due to the use of low on-impedance FETs, IRF521, instead of SCRs as in the LDL devices. The rise time of the current pulse is approximately 15 ns when the diode laser is mounted at the pulser output and slightly longer when an external BNC cable connects to the laser. The driver has external connections that supply the current pulse waveforms using a single American Laser Systems Model 711 inductive current probe. Current to the dual diode laser mount is also supplied through external BNC

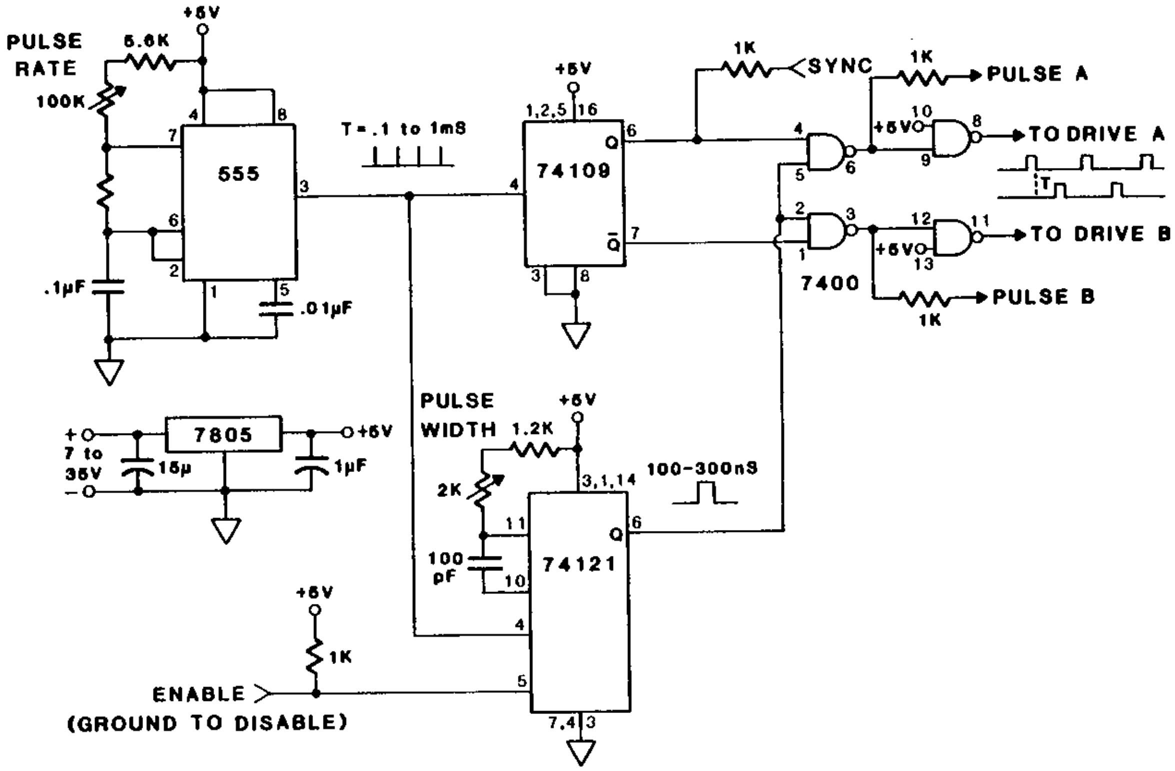

Figure 29. Timing circuitry for the dual diode laser pulser.

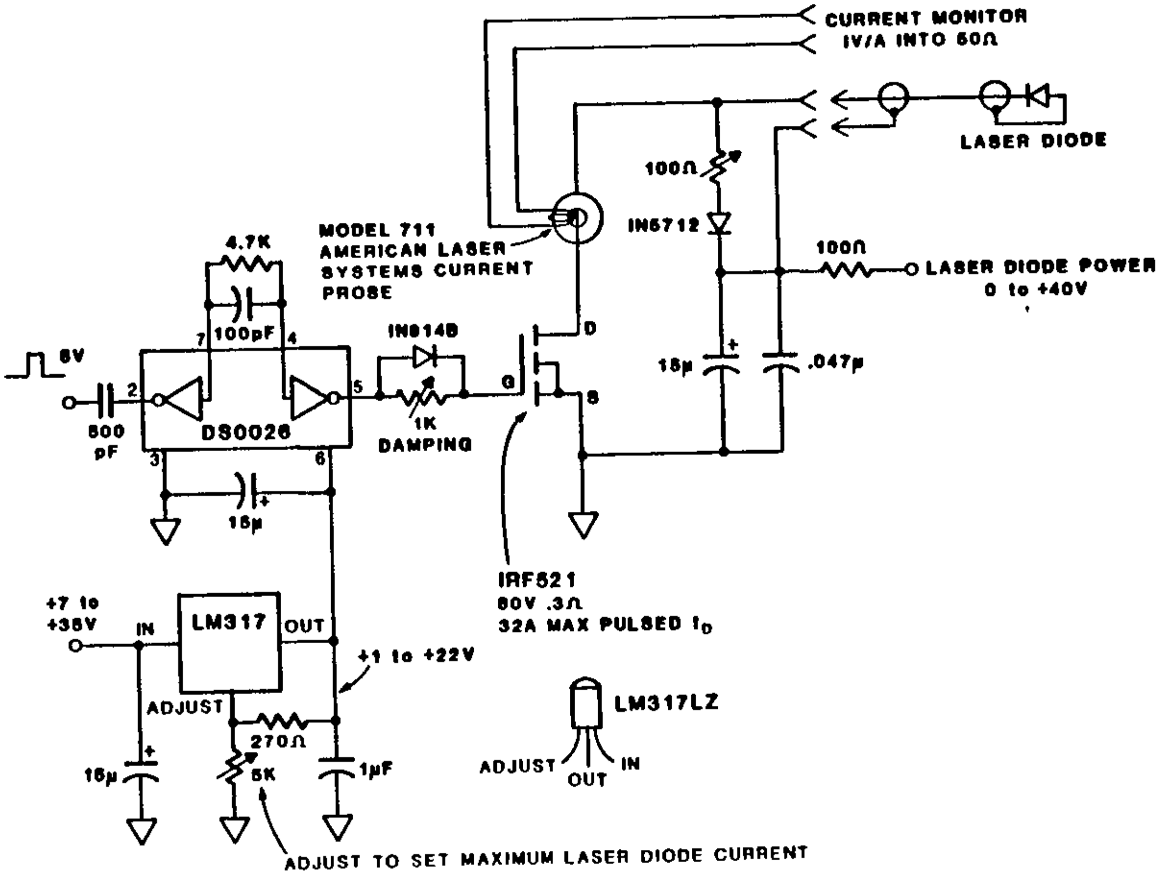

Figure 30. One current driver channel of the dual diode laser pulser.

connections.

The optical output characteristics of the dual diode laser source will now be described. Specifically, the wavelength bandwidth and tunability of the optical output will be discussed. The automatic tuning of the diffraction grating to an absorption maximum in methane will also be demonstrated.

Figure 31 shows the tuning range accessible by the dual diode external cavity. The figure was generated by focussing the light output from one diode laser in the dual cavity onto the slit of a Jarell-ash Mark-X 0.27 m spectrometer and scanning wavelength while synchronously detecting the spectrometer output with a Ge detector and lockin amplifier. It can be seen from the figure that a wavelength range of 1.624 to 1.648 μm (6158-6068 cm^{-1}) was achieved in this instance. In other cases, both slightly shorter and longer wavelengths have been achieved. It may be seen that the spectral range of the figure includes several lines, notably R6, of the $2\nu_3$ overtone band which was described in Section 3. However, not all wavelengths in this range were attainable.

Higher resolution spectral scans over a smaller region were conducted by placing a Fabry-Perot interferometer between the spectrometer output and the Ge detector. The interferometer consists of a piezoelectrically scanned Fabry-Perot device (Burleigh Model RC-110) driven by a ramp generator (Burleigh Model RC-42). The lockin amplifier output was then plotted on a chart recorder while holding the dual cavity grating fixed or the detector output was viewed on an oscilloscope screen while scanning the cavity grating. Figure 32 is an example of the chart recorder output. For this figure, the Fabry-Perot mirror separation was 0.013" yielding a interferometer free spectral range of 41 Angstroms. That is to say that the wavelength separation between the major peaks in the figure is 41 Angstroms. The slits of the spectrometer were adjusted

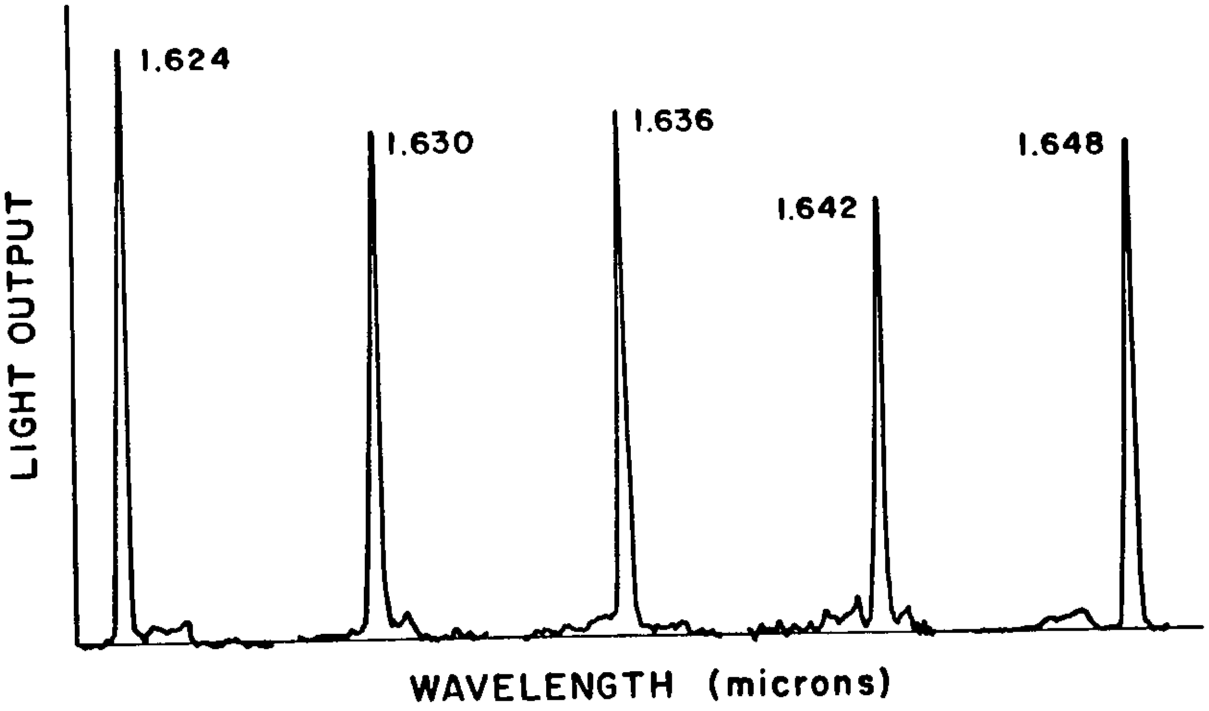

Figure 31. An example of the tuning range accessible by the dual diode external cavity.

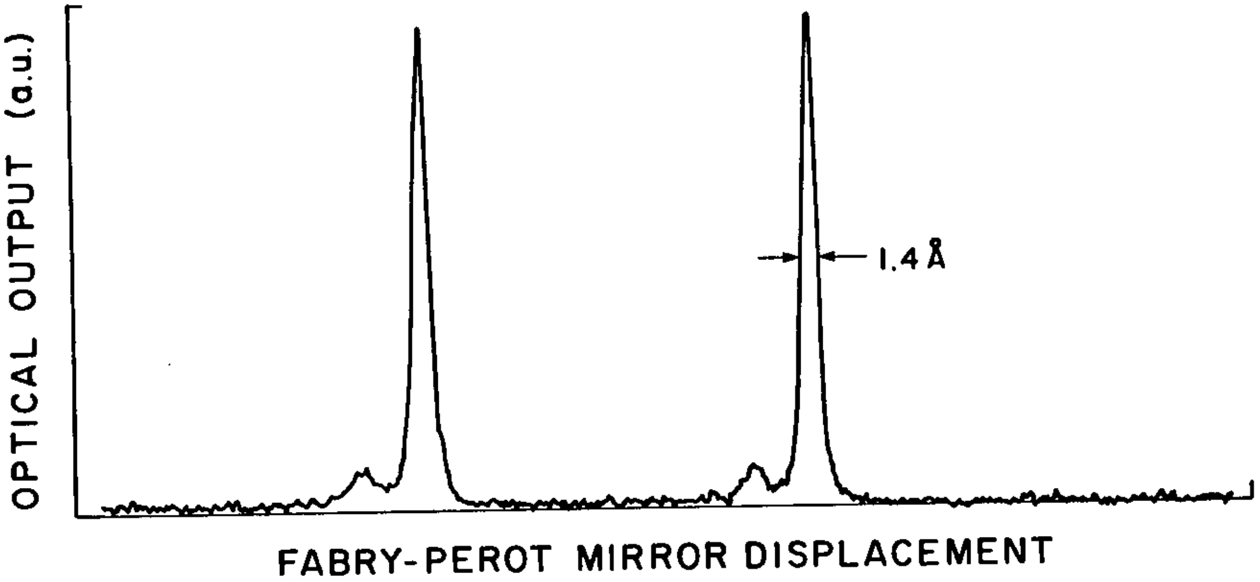

Figure 32. Optical output vs. Fabry-Perot mirror displacement for the dual diode external cavity.

to match this spectral range. From the figure, the calculated linewidth (FWHM) is 1.4 Angstroms. When the output was viewed on an oscilloscope and the grating was rotated, it was seen that for some positions of the grating the residual diode laser cavity modes, as determined by blocking the grating feed back while observing the spectrum, would appear. This was the cause of the inability mentioned above to achieve all wavelengths encompassed by the range of Figure 31. The source of such residual laser cavity modes is residual reflectivity which indicates that a more efficient AR coating would be required for more continuous tuning. It was also observed that tuning tended to be less efficient with usage over several days indicating possible degradation of the coatings.

Automatic tuning of the source wavelength to a methane absorption line was demonstrated in a 30 cm long cell filled with methane at atmospheric pressure. The cavity was tuned following the seven step procedure outlined above so that maximum absorption was attained for one diode while at the same time negligible absorption occurred for the other diode. The transmittance through the methane cell was recorded on magnetic tape as the wavelength controller rotated the grating over a range near maximum absorption seeking the minimum cell transmittance. Figure 33 shows the recorded data. In the figure, it can be seen that the dual diode laser output scans through a minimum in transmission and then retraces its steps through the minimum again. What has not been shown is the final high resolution scan, step 7, in the procedure described above.

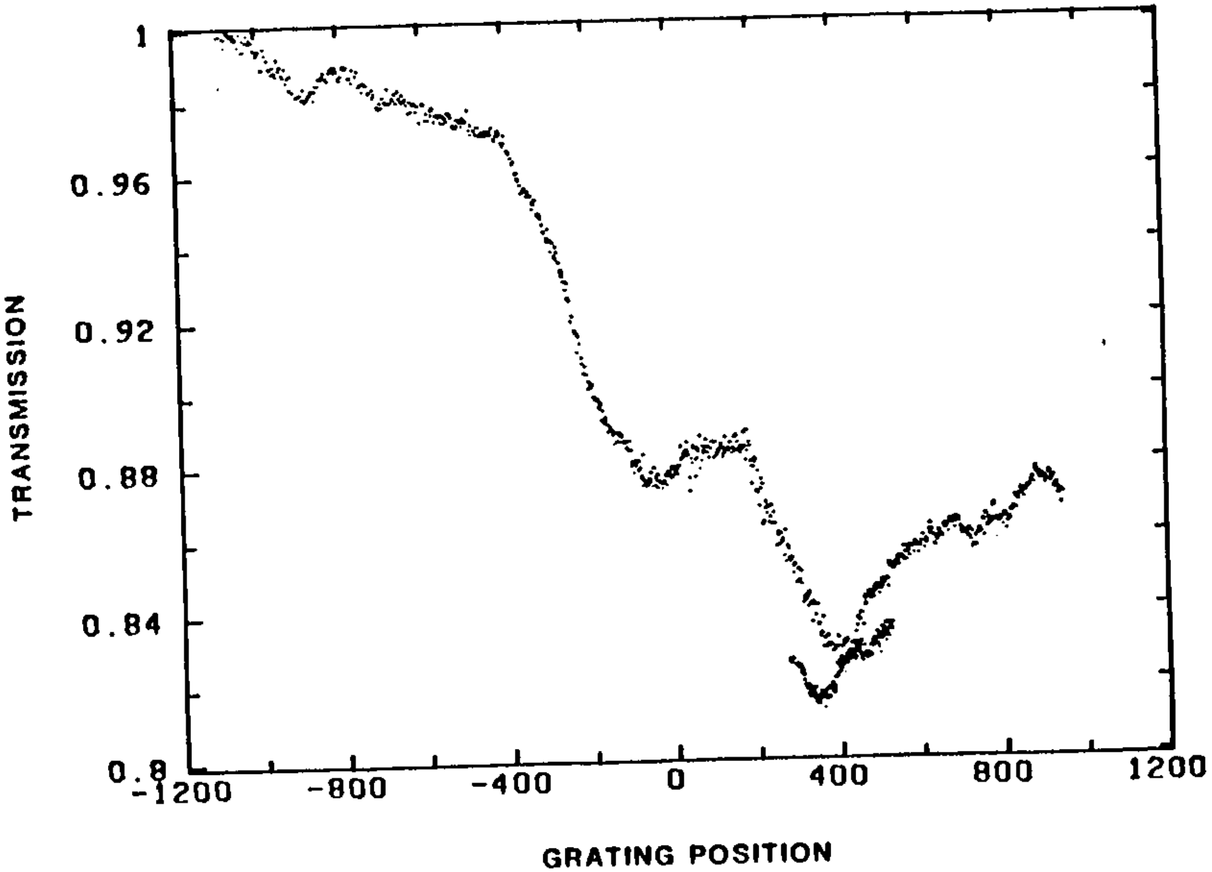

Figure 33. An example of the absorption as a function of wavelength measured by the dual diode laser cavity wavelength controller.

8. PERFORMANCE TESTS

(i) Lifetime Test

The setup used for lifetime testing is illustrated in Figure 34. The lifetime tests conducted involved continuous operation of the lasers over extended periods; sometimes for more than a week. For example the laser designated D16 was driven with 6 ampere, 160 nanosecond duration current pulses at a pulse repetition rate of 400 Hz for 63 hours and 50 minutes. The current was then increased to 9 amperes and the laser operated for 123 hours and 10 minutes. The total number of pulses in this test was therefore 2.7×10^8. The laser output power was recorded on the chart recorder throughout this test and found to vary less than 15% during each segment of the test. No trend to degraded operation was observed even at the end of the test run.

(ii) Output Power

The optical output from several lasers was measured with a calibrated Judson J16 Germanium photodetector. Essentially the same experimental setup was used as for the lifetime tests (Figure 34). The output power varied substantially from laser to laser but when devices were selected on the basis of lasing threshold those with thresholds less than about 2 amps were all observed to emit well in excess of 100 mW when driven with pulses of 7 amps peak current. Typical output power with 10 amp current pulses was 200 mW. Measurement of the output power when the lasers were mounted in the external off-axis parabolic mirror grating tuned cavity proved to be extremely difficult other than in a relative sense. It is estimated from qualitative observation of the intensity of the emission that 40% of the total output power could be concentrated into the single

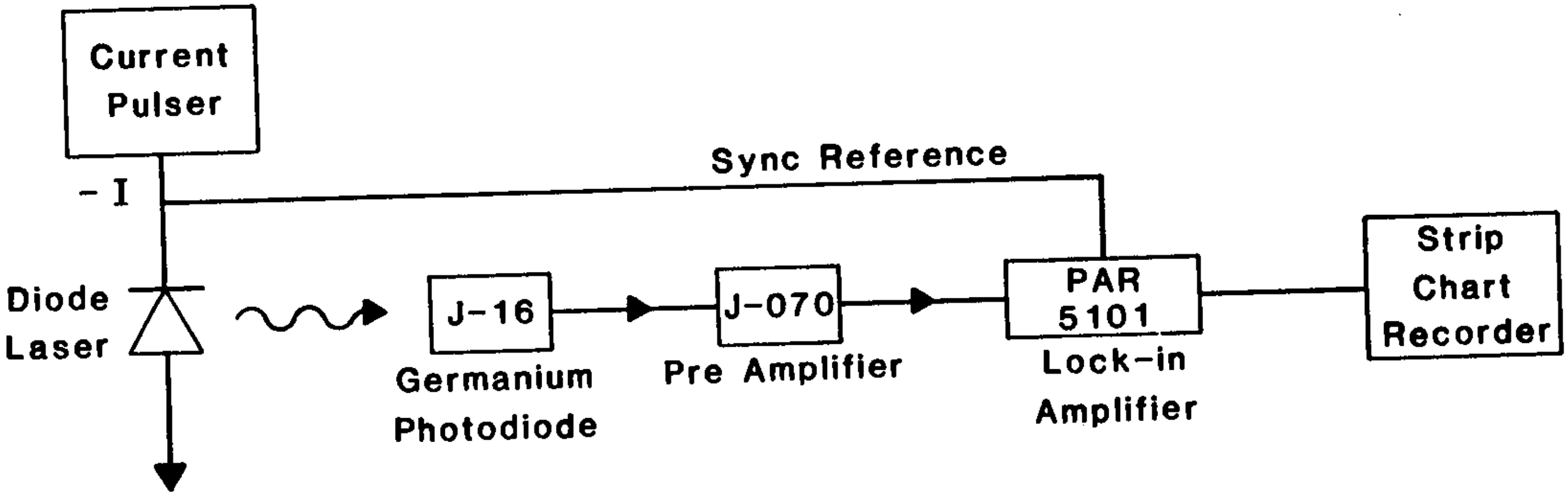

Figure 34. Experimental setup for lifetime testing of diode lasers.

line of the tuned cavity. This indicates that the on-line power would be as great as 80 mW when a selected laser was operated at a drive current of 10 amps.

(iii) Pulse Width and Repetition Rate

The width of the optical pulses can be inferred from the width of the drive current pulse. The timing circuit of the dual diode pulser displayed in Figure 29 allows the current pulse width to be varied from 100 to 300 nanoseconds FWHM. The optical pulse width is at least as short as the current pulse and is therefore adjustable from below 100 nsec to 300 nsec.

The pulse repetition rate is also controlled by the timing circuit shown in Figure 29. It is continuously variable from 100 Hz to 10 kHz. Since the pulses are directed alternately to the two diode lasers in the cavity this means that each laser may be fired at a rate variable from 50 Hz to 5 kHz.

(iv) Methane Absorption Measurements.

The setup used for making absorption measurements is illustrated in Figure 35. Part of the light from the dual diode laser cavity was split off and directed to a detector. The remainder of the light passed through the gas cell containing the gas of interest and fell on an identical detector. The outputs of the two detectors were then ratioed to normalize the power measurement against pulse to pulse laser power variations. Measurement of the methane absorption coefficient was accomplished by first filling the gas cell with 100% methane and tuning the laser cavity to an absorption maximum and the power transmitted through the cell measured. The gas cell was then

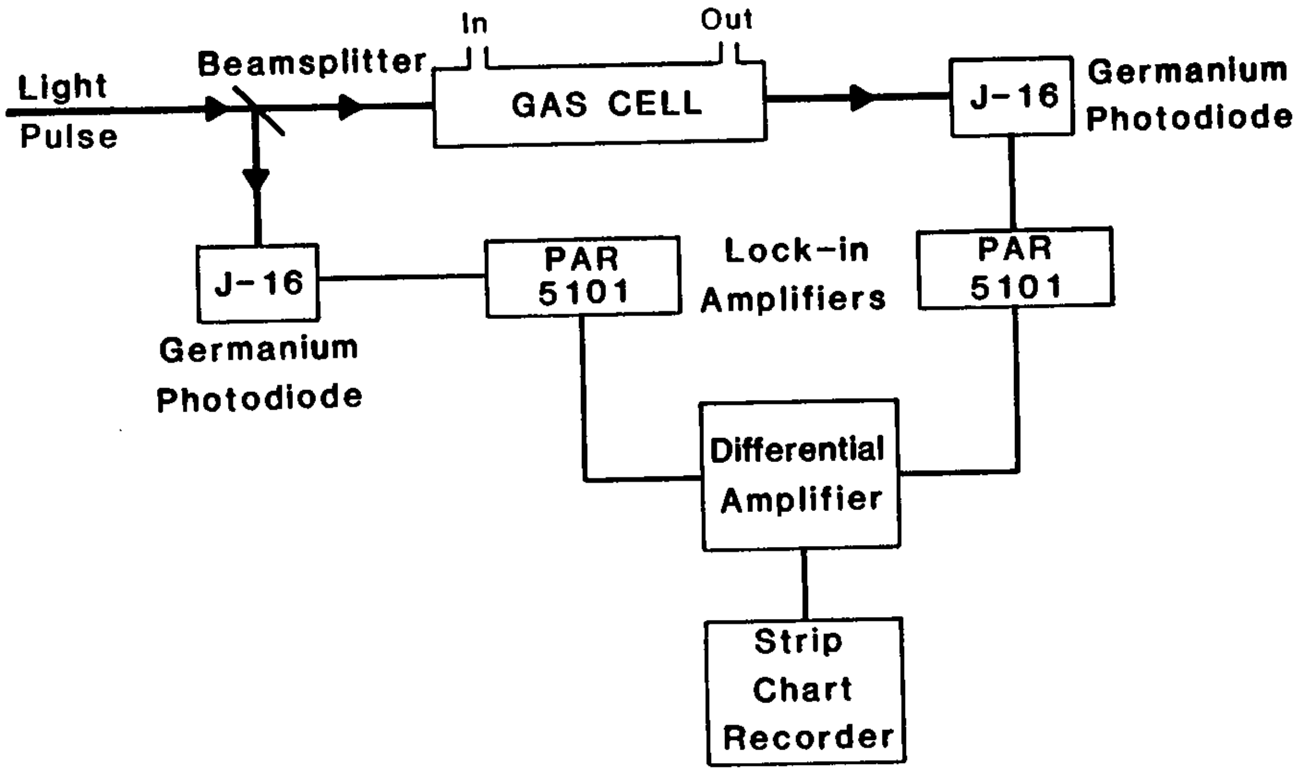

Figure 35. Experimental set-up for making absorption measurements.

filled with pure, dry nitrogen and the power measurement repeated. Methane (100%) was then reintroduced into the cell and the power again measured. The ratio of the power transmitted through the methane filled cell to that transmitted through the cell filled with nitrogen was 0.44 as recorded in Figure 36. Although greater attenuation was observed with some realizations of the dual diode laser cavity this was the best documented result achieved. Assuming exponential attenuation of the laser light in the gas and noting that the length of the cell was 31.5 cm an absorption coefficient of 0.026 (cm atm)$^{-1}$ was calculated. When the laser cavity was tuned off a methane absorption line the absorption coefficient was calculated to be less than 0.002 (cm atm)$^{-1}$. The difference between the on-line and off-line absorption coefficients is therefore 0.024 (cm atm)$^{-1}$.

The absorption coefficents of other atmospheric constituents could be measured in the same way. However time did not permit further evaluation of the system.

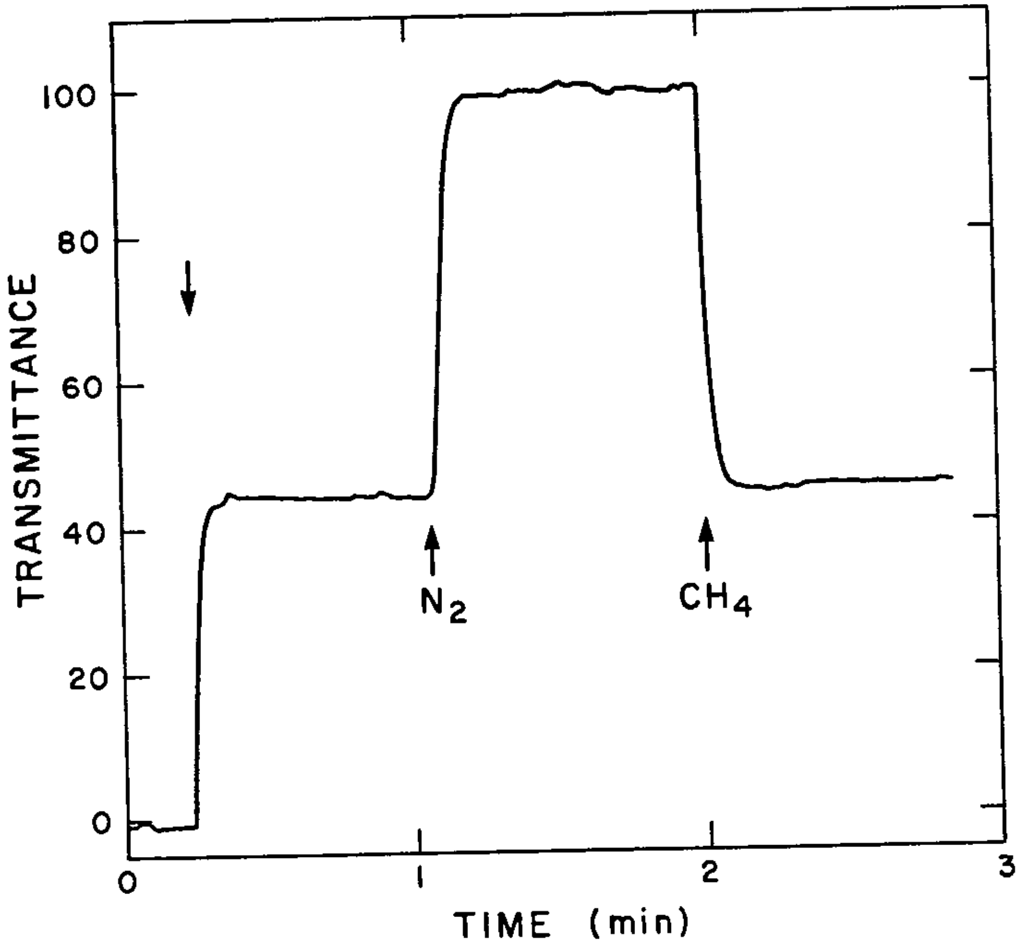

Figure 36. Transmittance versus time. The downward pointing arrow indicates the time at which the laser light was allowed to pass through the methane filled gas cell. The other arrows indicate the time that the cell was filled with nitrogen and methane for the second time.

9. CONCLUSION AND RECOMMENDATIONS

A dual wavelength light source for remote DIAL measurement of methane has been constructed, performance tested, and operation of its automatic tuning feature demonstrated. The light source has several novel features including use of two diode lasers in a single external cavity, a motor-micrometer controlled diffraction grating as a tuning element, and an off-axis, diamond machined aluminum, parabolic mirror to couple the diode lasers and diffraction grating.

The dual diode external cavity source was designed for use in a differential absorption system. The available techniques for remote optical detection were examined in Section 2 where it was shown that a DIAL system is well suited to the conditions in coal mines. The spectroscopy of methane and other coal gas constituents was reviewed in Section 3. The spectral region around 1.65 μm was found to be nearly ideal for a diode laser DIAL system both because of the sparcity of spectral features of the other gases and because of the overlap with the emission spectrum of diode lasers which operate at ambient temperatures. In particular InGaAS lasers emitting at 1.65 μm were available.

The properties of broad area diode lasers of the type used in this dual diode source were discussed in Section 4. It was noted there that the linewidth of the laser emission was several times broader than the width of the absorption lines in the methane spectrum; a fact implying that insufficient absorption of the laser light would occur as discussed in Section 3 thus indicating a need to narrow the laser linewidth.

The question of sensitivity and noise was discussed in detail in Section 5. It was shown there that the Federal regulations for methane measurement could be met with a signal to noise ratio of 300:1 and that this SNR could be achieved by signal averaging provided the laser line could be narrowed to approximately 0.2 cm^{-1} as discussed in Section 3. The optical design of the off-axis external cavity was detailed in Section 6. It included analysis of the laser/grating coupling system with a ray-tracing program and generation of spot patterns in the plane of the laser. The off-axis parabolic mirror was shown to he aberration free.

The individual components of the dual wavelength source, the complete assembly (Figure 17) and the mode of operation were described in Section 7. The diamond machined mirror (Figure 18) was tested and the machined surface showed acceptably low scattering losses. A motor driven micrometer with optical encoded shaft position readout controls the position of the diffraction grating tuning element and allows precise tuning of the lasing wavelength to an absorption line under microprocessor control. The tuning range of the system was demonstrated to be more than 24 nm centered at 1.636 μm. The mode of operation of the system is to scan the wavelength of the laser over its tuning range in relatively course steps searching for a maximum of absorption in a reference cell containing methane. It then returns to the position of maximum absorption and repeats the scan in finer steps to precisely locate the optimum wavelength for making methane measurements.

The perfomance tests on the dual diode laser cavity are described in Section 8. These were tests to measure laser lifetimes, output power and the absorption of the laser light in methane. The results of these tests and some operating parameters of the dual diode laser cavity will now be compared to the design values and the overall performance of the system evaluated.

The system design called for the dual wavelength light source to have the following operating parameters:

- Output Power Level - greater than 50 mW peak power with less than 25% pulse to pulse variation.

- Pulse Width - less than 300 nsec; 200 nsec nominal.

- Pulse Repetition Rate - greater than 100 Hz; 500 Hz nominal.

- Laser Lifetime - 10^8 pulses at a prf greater than 100 Hz with less than 25% power degradation.

- Methane Absorption Coefficient - greater than 0.1 $(\text{cm atm})^{-1}$ on-line; less than 0.01 $(\text{cm atm})^{-1}$ off-line.

- Other Species Absorption Coefficients - less than 5.5×10^{-3} $(\text{cm atm})^{-1}$ in both H_2O and CO_2.

All of the above design goals were to be satisfied by the dual wavelength light source or it was to be shown that any failing parameter would not be crucial to the performance of a remote methane measurement system.

The results of the laser lifetime tests reported in Section 8(i) clearly show that the design lifetime of 10^8 pulses with less than 25% degradation in output power was achieved. The pulse width and repetition rate also meet the design requirements of 200 nsec and 500 Hz as reference to Section 8(iii) reveals. In fact the pulses can be made as short as 100 nsec in duration and the repetition rate can be as great as 5 kHz.

As discussed in Section 8(ii) the output power levels achieved with the individual lasers selected for use in this study were all at least 200 mW when the lasers were driven with 10 amp current pulses. Approximately 40% of the power emitted by the lasers could be concentrated in a single line when the lasers were mounted in the grating tuned cavity. The on-line peak power which was achieved with the dual diode light source was therefore approximately 80 mW which exceeds the minimum design value by 60%.

The methane absorption coefficient measurements were described in Section 8(iv). The value 0.026 $(\text{cm atm})^{-1}$ attained for the on-line absorption coefficient was well below the design goal of 0.1 $(\text{cm atm})^{-1}$. The reason for this discrepancy can be traced to the failure to achieve the emitting linewidth of 0.05 nm with the grating tuned cavity. The observed linewidth of 0.14 nm (see Section 7) is about 3 times broader than the lines in the absorption spectrum of methane around 1.65 μm and the laser light is therefore not efficiently absorbed. The value of 0.002 $(\text{cm atm})^{-1}$ which was determined for the off-line coefficient is a factor of five better than the design goal.

Time and resources did not permit measurement of the absorption coefficients in water vapor or carbon dioxide. These are certainly important constituents of the mine atmosphere. However measurement of these absorption coefficients was given a low priority since the spectroscopy of both species is well understood and their absorption lines in the 1.65 μm region of the spectrum are tabulated in the AFCRL compilation[65]. The strongest water line near the prominent methane features which were used in this project is 2000 times weaker than the methane lines. Similarly the strongest CO_2 line is 150 times weaker than the methane lines. This indicates that the absorption coefficients of both water and carbon dioxide should be less than 2×10^{-4} and the design requirement satisfied.

It may be said then that the dual wavelength light source has met all design requirements save that of the on-line methane absorption coefficient. To see whether this is a serious defect it is necessary to refer to some of the calculations presented in

Section 5 and Appendix D. It was shown there that the signal to noise ratio which was required to satisfy Federal Regulations was 300:1 if the absorption coefficient was 0.15 $(\mathrm{cm\ atm})^{-1}$. If the absorption coefficient is instead 0.024 $(\mathrm{cm\ atm})^{-1}$ the required SNR is 1875:1 and the signal to noise must be improved by a factor of 530 by signal averaging. This implies averaging over 280,000 pulses. At the 5 kHz maximum prf which can be obtained with the drive current pulser this would entail averaging for some 56 seconds. This is considerably longer than ideal for practical measurement of methane concentrations at the working face of a coal mine. As a result we believe that the dual wavelength light source is not suitable for use in an instrument to remotely measure methane in coal mines. It may therefore be asserted that the dual wavelength light source has met all the design goals except for the low on-line methane absorption coefficient and that this failure significantly detracts from the utility of the light source.

Although the construction and performance testing of the dual wavelength light source described in this report represents a significant accomplishment in the development of mine safety instumentation and the design could be modified to meet the methane absorption coefficient design goal by increasing the focal length of the parabolic mirror and the size of the diffraction grating (see Equation 21) it is not recommended that further effort be expended on improving this design. This is because the increased size of the source implied by an increase in the size of the mirror partially defeats the purpose of using diode lasers and because the rapidly changing technology of semiconductor lasers has resulted in more promising types of lasers and line narrowing techniques. For example, phased array diode lasers are capable of producing high power optical pulses comparable to those produced by the broad area lasers used in this study and have a narrower emission spectrum and better optical beam quality[92]. Cleaved-coupled-cavity (C^3) lasers have the potential of narrowing the emission of a multiple emitter phased array so that it matches the width of an absorption line[198]. It is true that this type of laser has not yet been fabricated in InGaAs or other material suitable for 1.65 μm or longer wavelength emission but the techniques should be applicable to such materials. It is recommended that these new developments be thoroughly evaluated prior to further developmental work on remote coal mine methanometers.

References

1. R. L. Marovelli and J. M. Karhnak, "The mechanization of mining," *Sci. Am.*, vol. 247, pp. 91-102, Sept. 1982.
2. *Federal Coal Mine Health and Safety Act of 1969.*
3. S. B. Eynon, "Leak detection-status & needs," *GRI Workshop*, Feb. 1983.
4. G. Schnakenberg, "Gas detection instrumentation... what's new and what's to come," *Coal Age*, pp. 84-92, Mar. 1975.
5. W. D. Egan, "General performance specifications for an instrument to remotely measure methane in a coal mine," Bethlehem Steel Corporation Homer Research Laboratories Internal Report, File #1006-3a, 15 May 1978.
6. *The Story of Coal,* Bethlehem Steel Corporation.
7. W. D. Egan, "Remote measurement of methane in coal mines," Report BX-41-78010 IR, Dec. 10 1979. Bethlehem Steel Corporation Homer Research Laboratories Internal Report, File #10066-3a
8. R. L. Byer, "Remote measurement of methane in a coal mine environment," Report from Stanford University Edward L. Ginzton Laboratory of Physics to Bethlehem Steel Corporation Homer Research Laboratories, Aug. 1978.
9. H. R. Wittman, "An Erbium laser target illuminator pumped by GaAs LEDs," *U.S. Army, Project No. 1T061102B23D*, 1970. MC Management Structure Code #501B.11.0310
10. "Electrical Equipment, Lamps, Methane Detectors; Tests for Permissibility; Fees," *Title 30, Sub-Chapter D, Part 18*, U.S. Dept. of Commerce, Mine and Safety Administration, July 1980.

11. M. A. Pollack, R. E. Nahory, J. C. DeWinter, and A. A. Ballman, "Liquid phase epitaxial $In_{1-x}Ga_xAs_yP_{1-y}$ lattice matched to <100> InP over the complete wavelength wange $0.92 \leq \lambda \leq 1.65$ μm," *Appl. Phys. Lett.*, vol. 33, pp. 314-316, 15 Aug. 1978.

12. J. J. Hsieh, "Zn-diffused, stripe-geometry, double-heterostructure GaInAsP diode lasers," *IEEE J. Quantum Electron.*, vol. QE-15, pp. 694-697, Aug. 1979.

13. S. Arai, Y. Suematsu, and Y. Itaya, "1.11-1.67 μm (100) GaInAsP/InP injection lasers prepared by liquid phase epitaxy," *IEEE J. Quantum Electron.*, vol. QE-16, pp. 197-205, Feb. 1980.

14. B. I. Miller, J. H. McFee, R. J. Martin, and P. K. Tien, "Room-temperature operation of lattice-matched $InP/Ga_{0.47}In_{0.53}As/InP$," *Appl. Phys. Lett.*, vol. 33, pp. 44-47, 1 July 1978.

15. G. H. Olsen, T. J. Zamerowski, and N. J. DiGiuseppe, "1.5-1.7 μm V.P.E. InGaAsP/InP C.W. lasers," *Elect. Lett.*, vol. 16, pp. 516-517, 19 June 1980.

16. W. T. Tsang, "$Al_{0.48}In_{0.52}As/Ga_{0.47}In_{0.53}As/Al_{0.48}In_{0.52}As$ double-heterostructure lasers grown by molecular-beam epitaxy with lasing wavelength at 1.65μm," *J. Appl. Phys.*, vol. 52, pp. 3861-3865, June 1981.

17. R. K. DeFreez, R. A. Elliott, J. S. Blakemore, B. I. Miller, J. H. McFee, and R. J. Martin, "High-output room-temperature pulsed operation for broad contact $InP/In_{0.53}Ga_{0.47}As/InP$ lasers grown by molecular beam epitaxy," *J. Appl. Phys.*, vol. 54, pp. 2177-2182, May 1983.

18. J. S. Blakemore and R. K. DeFreez, "Methane detection research," , Oct. 1981. Report to Bethlehem Steel Corporation Homer Research Laboratories from Oregon Graduate Center

19. G. Fiocco and L. D. Smullin, *Nature*, vol. 199, pp. 1275-1276, 1963.

20. H. Kildal and R. L. Byer, "Comparison of laser methods for the remote detection of atmospheric pollutants," *IEEE Proc.*, vol. 59, pp. 1644-1663, Dec. 1971.

21. R. L. Byer, "Review: remote air pollution measurement," *Opt. Quan. Electron.*, vol. 7, pp. 147-177, 1975.

22. K. Petri, A. Salik, and J. Cooney, "Variable-wavelength solar-blind raman lidar for remote measurement of atmospheric water-vapor concentration and temperature," *Appl. Opt.*, vol. 21, pp. 1212-1218, 1 Apr. 1982.

23. D. A. Leonard, "Remote raman measurement techniques," *Opt. Eng.*, vol. 20, pp. 91-94, Jan./Feb. 1981.

24. J. A. Cooney, "Uses of raman scattering for remote sensing of atmospheric properties of meteorological significance," *Opt. Eng.*, vol. 22, pp. 292-301, May/June 1983.

25. W. D. Egan, "Technical concerns-bumines raman scattering technique for remote methane gas measurement," HRL File Memo, File 1006-3a, 10 July 1981.

26. R. L. Byer and M. Garbuny, "Pollutant detection by absorption using mie scattering and topographic targets as retroreflectors," *Appl. Opt.*, vol. 12, pp. 1496-1505, July 1973.

27. M. J. Kavaya, R. T. Menzies, D. A. Haner, U. P. Oppenheim, and P. H. Flamant, "Target reflectance measurements for calibration of lidar atmospheric backscatter data," *Appl. Opt.*, vol. 22, pp. 2619-2628, 1 Sep. 1983.

28. W. B. Grant, "Effect of differential spectral reflectance on DIAL measurements using topographic targets," *Appl. Opt.*, vol. 21, pp. 2390-2394, 1 July 1982.

29. R. M. Schotland, *Proc. 4th Symposium on Remote Sensing of the Environment*, Ann

Arbor, Michigan, Apr. 1966.

30. B. Marthinsson, J. Johansson, and S. T. Eng, "Air pollution monitoring with a computer-controlled CO_2-laser long-path absorption system," *Opt. Quan. Electron.*, vol. 12, pp. 327-334, 1980.

31. S. Lundqvist, C. Falt, U. Persson, B. Marthinsson, and S. T. Eng, "Air pollution monitoring with a Q-switched CO_2-laser lidar using heterodyne detection," *Appl. Opt.*, vol. 20, pp. 2534-2538, 15 July 1981.

32. N. Menyuk, D. K. Killinger, and W. E. DeFeo, "Laser remote sensing of hydrazine, MMH, and UDMH using a differential-absorption CO_2 LIDAR," *Appl. Opt.*, vol. 21, pp. 2275-2286, 15 June 1982.

33. D. K. Killinger, N. Menyuk, and W. E. DeFeo, "Experimental comparison of heterodyne and direct detection for pulsed differential absorption CO_2 lidar," *Appl. Opt.*, vol. 22, pp. 682-689, 1 Mar. 1983.

34. T. Kobayasi, M. Hirama, and H. Inaba, "Remote monitoring of NO_2 molecules by differential absorption using optical fiber link," *Appl. Opt.*, vol. 20, pp. 3279-3280, 1 Oct. 1981.

35. M. Endemann and R. L. Byer, "Simultaneous remote measurements of atmospheric temperature and humidity using a continuously tunable IR lidar," *Appl. Opt.*, vol. 20, pp. 3211-3217, 15 Sep. 1981.

36. K. Fredriksson, B. Galle, K. Nystrom, and S. Svanberg, "Lidar system applied in atmospheric pollution monitoring," *Appl. Opt.*, vol. 18, pp. 2998-3003, 1 Sep. 1979.

37. K. Fredriksson, B. Galle, K. Nystrom, and S. Svanberg, "Mobile lidar system for environmental probing," *Appl. Opt.*, vol. 20, pp. 4181-4189, 15 Dec. 1981.

38. M. Alden, H. Edner, and S. Svanberg, "Laser monitoring of atmospheric NO using ultraviolet differential-absorption techniques," *Opt. Lett.*, vol. 7, pp. 543-545, Nov. 1982.

39. W. A. McClenny and G. M. Russwurm, "Laser-based long path monitoring of ambient gases- analysis of two systems," *Atmos. Envir.*, vol. 12, pp. 1443-1453, 1978.

40. J. Reid, J. Shewchun, B. K. Garside, and E. A. Ballik, "High sensitivity pollution detection employing tunable diode lasers," *Appl. Opt.*, vol. 17, pp. 300-307, 15 Jan. 1978.

41. D. T. Cassidy and J. Reid, "Atmospheric pressure monitoring of trace gases using tunable diode lasers," *Appl. Opt.*, vol. 21, pp. 1185-1190, 1 Apr. 1982.

42. C. R. Webster and W. B. Grant, "Laboratory simulation of tunable diode laser remote measurement of atmospheric gases using topographic targets," *Appl. Opt.*, vol. 22, pp. 1952-1954, 1 July 1983.

43. E. D. Hinkley, "Laser spectroscopic instrumentation and techniques: long-path monitoring by resonance absorption," *Opt. Quan. Electron.*, vol. 8, pp. 155-167, 1976.

44. W. B. Grant and R. T. Menzies, "A survey of laser and selected optical systems for remote measurement of pollutant gas concentrations," *J. Air Poll. Control Assoc.*, vol. 33, pp. 187-194, Mar. 1983.

45. B. N. Edwards and D. E. Burch, "Absorption of 3.39-micron helium-neon laser emission by methane in the atmosphere," *J. Opt. Soc. Am.*, vol. 55, pp. 174-177, Feb. 1965.

46. K. O. White and S. A. Schleusener, "Coincidence of Er:YAG laser emission with methane absorption at 1645.1 nm," *Appl. Phys. Lett.*, vol. 21, pp. 419-420, 1 Nov. 1972.

47. E. R. Murray, J. E. van der Laan, and J. G. Hawley, "Remote measurement of HCl, CH_4, and N_2O using a single-ended chemical-laser lidar system," *Appl. Opt.*, vol. 15, pp. 3140-3148, Dec. 1976.

48. E. R. Murray, "Remote measurement of gases using discretely tunable infrared lasers," *Opt. Eng.*, vol. 16, pp. 284-290, May/June 1977.

49. E. R. Murray, "Remote measurement of gases using differential-absorption LIDAR," *Opt. Eng.*, vol. 17, pp. 30-38, Jan./Feb. 1978.

50. R. A. Baumgartner and R. L. Byer, "Continuously tunable IR lidar with applications to remote measurements of SO_2 and CH_4," *Appl. Opt.*, vol. 17, pp. 3555-3561, 15 Nov. 1978.

51. W. B. Grant and E. D. Hinkley, "Laser system for natural gas detection-phase I: laboratory feasibility studies," Report for Gas Research Institute, Jet Propulsion Lab., Pasadena, Calif., 21 July 1982.

52. W. B. Grant, "Helium-Neon laser remote sensing of methane leaks," *GRI Workshop*, Feb. 1983.

53. W. B. Grant and C. R. Webster, "Measurement of gases using CW lasers, differential absorption, and topographic targets," *Technical Digest of the Optical Society of America Topical Meeting on Optical Techniques for Remote Probing of the Atmosphere*, Incline Village, Nevada, Jan. 1983. Paper TuC13

54. A. Rosengreen and L. L. Altpeter, "Portable remote sensing system (DIAL) for leak detection of natural gases," *GRI Workshop*, Feb. 1983.

55. K. Chan, H. Ito, and H. Inaba, "Optical remote monitoring of CH_4 gas using low-loss optical fiber link and InGaAsP light-emitting diode in 1.33-μm region," *Appl. Phys. Lett.*, vol. 43, pp. 634-636, 1 Oct. 1983.

56. K. O. White and W. R. Watkins, "Erbium laser as a remote sensor of methane," *Appl. Opt.*, vol. 14, pp. 2812-2813, Dec. 1975.

57. W. R. Watkins and K. O. White, "Wedge absorption remote sensor," *Rev. Sci. Instrum.*, vol. 52, pp. 1682-1684, Nov. 1981.

58. W. D. Egan, R. T. Boos, R. K. DeFreez, and R. L. Byer, "Remote differential absorption and scattering measurement of methane near a coal mine working face," *Technical Digest of the Conference on Lasers and Electro-Optics*, Baltimore, MD, May 1983. Paper ThK3

59. W. D. Egan, R. Boos, R. K. DeFreez, and R. L. Byer, *Remote Measurement of Concentration of a Gas Specie by Resonance Absorption*, 7 Dec. 1982. U.S. Patent # 4,362,388

60. R. K. DeFreez, "Remote DIAL Measurements of Methane in Coal Mines," *Technical Digest of the Optical Society of America Topical Meeting on Optical Remote Sensing of the Atmosphere*, Incline Village, Nevada, January, 1985. Invited Paper ThB2

61. R. K. DeFreez and R. A. Elliott, "Laser diode source for methane detection in coal gas," *Technical Digest of the Conference on Lasers and Electro-Optics*, Baltimore, MD, May 1983. Paper ThK2

62. R. K. DeFreez and R. A. Elliott, "External grating-tuned dual-diode-laser source for remote detection of coal gas methane," *(A) J. Opt. Soc. Am.*, vol. 73, p. 1854, Dec. 1983.

63. G. H. B. Thompson, *Physics of Semiconductor Laser Devices,* John Wiley & Sons, New York, N.Y., 1980.

64. R. S. Eng, J. F. Butler, and K. J. Linden, "Tunable diode laser spectroscopy: an invited review," *Opt. Eng.*, vol. 19, pp. 945-960, Nov./Dec. 1980.

65. R. A. McClatchey, W. S. Benedict, S. A. Clough, D. E. Burch, R. F. Calfee, K. Fox, L. S. Rothman, and J. S. Garing, *AFCRL Atmospheric Absorption Line Parameters Compilation,* Air Force Cambridge Research Laboratories, Bedford, Mass., 1973.

66. L. S. Rothman, "AFGL atmospheric absorption line parameters compilation: 1980 version," *Appl. Opt.*, vol. 20, pp. 791-795, 1 Mar. 1981.

67. G. Herzberg, *Molecular Spectra and Molecular Structure: II. Infrared and Raman Spectra of Polyatomic Molecules,* D. Van Nostrand Co., Inc., Princeton, N.J., 1968.

68. Optical Society of America, *Handbook of Optics,* McGraw-Hill, 1978.

69. *Handbook of Physics and Chemistry,* CRC Press, 1980-1981. 51st ed.

70. E. J. McCartney, *Absorption and Emission by Atmospheric Gases: The Physical Processes,* John Wiley and Sons, New York, N.Y., 1983.

71. A. G. Kim, *The composition of coalbed gas,* U. S. Bureau of Mines, 1973. Report of Investigations 7762

72. N Kobayashi and Y. Horikoshi, "Liquid phase epitaxial growth of $InAs_{1-x-y}P_xSb_y$ on an InAs Substrate," *Jpn. Jnl. Appl. Phys.*, vol. 20, pp. 2301-2305, Dec. 1981.

73. L. M. Dolginov, A. E. Drakin, L. V. Druzhinina, P. G. Eliseev, M. G. Milvidsky, V. A. Skripkin, and B. N. Sverdlov, "Low threshold heterojunction AlGaAsSb/GaSb lasers in the wavelength range of 1.5-1.8 μm," *IEEE J. Quantum Electron.*, vol. QE-17, pp. 593-597, May 1981.

74. N. Kobayashi, Y. Horikoshi, and C. Uemura, "Room temperature operation of the InGaAsSb/AlGaAsSb DH laser at 1.8 μm wavelength," *Jpn. J. Appl. Phys.*, vol. 19, pp. L30-L32, Jan. 1980.

75. K. Fox, G. W. Halsey, and D. E. Jennings, "High resolution spectrum and analysis of $2\nu_3$ of $^{13}CH_4$ at 1.67 μm," *J. Mol. Spectrosc.*, vol. 83, pp. 213-222, 1980.

76. B. Bobin, "Interpretation de la bande harmonique $2\nu_3$ du methane $^{12}CH_4$ (De 5,890 A 6,107 cm^{-1})," *J. Physique*, vol. 33, pp. 345-352, Apr. 1972.

77. D. J. Brassington, R. C. Felton, B. W. Jolliffe, B. R. Marx, J. T. M. Moncrieff, W. R. C Rowley, and P. T. Woods, "Errors in spectroscopic measurements of SO_2 due to nonexponential absorption of laser radiation, with application to the remote monitoring of atmospheric pollutants," *Appl. Opt.*, vol. 23, pp. 469-475, 1 Feb. 1984.

78. D. E. Burch and D. Williams, "Total absorptance of carbon monoxide and methane in the infrared," *Appl. Opt.*, vol. 1, pp. 587-594, Sep. 1962.

79. D. E. Burch, E. B. Singleton, and D. Williams, "Absorption line broadening in the infraredlp," *Appl. Opt.*, vol. 1, pp. 359-363, May 1962.

80. A. Anderson, An-Ti Chai, and D. Williams, "Self-broadening effects in the infrared bands of gases," *J. Opt. Soc. Am.*, vol. 57, pp. 240-246, Feb. 1967.

81. R. L. Moon, G. A. Antypas, and L. W. James, "Bandgap and lattice constant of GaInAsP as a function of alloy composition," *J. Electron. Mater.*, vol. 3, pp. 635-645, 1974.

82. J. J. Hsieh, "Room-temperature operation of GaInAsP/InP double-heterostructure diode lasers emitting at 1.1 μm," *Appl. Phys. Lett.*, vol. 28, pp. 283-285, 1 Mar. 1976.

83. G. H. Olsen, "InGaAsP laser diodes," *Opt. Eng.*, vol. 20, pp. 440-445, May/June 1981.

84. K. J. Bachmann and J. L. Shay, "An InGaAs detector for the 1.0-1.7-μm wavelength range," *Appl. Phys. Lett.*, vol. 32, pp. 446-448, 1 Apr. 1978.

85. C. E. Hurwitz, "Detectors for the 1.1 to 1.6 μm wavelength region," *Opt. Eng.*, vol. 20, pp. 658-664, July/Aug. 1981.

86. T. P. Pearsall, M. Piskorski, A. Brochet, and J. Chevrier, "A $Ga_{0.47}In_{0.53}As$/InP heterophotodiode with reduced dark current," *IEEE J. Quantum Electron.*, vol. QE-17, pp. 255-259, Feb. 1981.

87. T. Izawa, N. Shibata, and A. Takeda, "Optical attenuation in pure and doped fused silica in the IR wavelength region," *Appl. Phys. Lett.*, vol. 31, pp. 33-35, 1 July 1977.

88. J. C. Gammel, H. Ohno, and J. M. Ballantyne, "High-speed photoconductive detectors using GaInAs," *IEEE J. Quantum Electron.*, vol. QE-17, pp. 269-272, Feb. 1981.

89. T. P. Pearsall, "$Ga_{0.47}In_{0.53}As$: a ternary semiconductor for photodetector applications," *IEEE J. Quantum Electron.*, vol. QE-16, pp. 709-719, July 1980.

90. T. P. Pearsall and M. Papuchon, "The $Ga_{0.47}In_{0.53}As$ homojunction photodiode - a new avalanche photodetector in the near infrared between 1.0 and 1.6 μm," *Appl. Phys. Lett.*, vol. 33, pp. 640-642, 1 Oct. 1978.

91. J. Shah, R. E. Nahory, R. F. Leheny, J. Degani, and A. E. DiGiovanni, "Hot-carrier relaxation in p-$In_{0.53}Ga_{0.47}As$," *Appl. Phys. Lett.*, vol. 40, pp. 505-507, 15 Mar. 1982.

92. D. R. Scifres, C. Lindstrom, R. D. Burnham, W. Streifer, and T. L. Paoli, "Phase-

locked (GaAl)As laser diode emitting 2.6 W CW from a single mirror," *Electron. Lett.*, vol. 19, pp. 169-171, 3 Mar. 1983.

93. T. R. Chen, K. L. Yu, B. Chang, A. Hasson, S. Margalit, and A. Yariv, "Phase-locked InGaAsP laser array with diffraction coupling," *Appl. Phys. Lett.*, vol. 43, pp. 136-137, 15 July 1983.

94. B. I. Miller and J. H. McFee, "Growth of $Ga_yIn_{1-y}As/InP$ heterostructures by molecular beam epitaxy," *J. Electrochem. Soc.*, vol. 125, pp. 1310-1317, Aug. 1978.

95. H. C. Casey and M. B. Panish, *Heterostructure Lasers: Part A: Fundamental Principles,* Academic Press, New York, N.Y., 1978.

96. D. Marcuse, *Theory of Dielectric Optical Waveguides,* Academic Press, New York, 1974.

97. H. Kressel and J. K. Butler, *Semiconductor Lasers and Heterojuction LEDs,* Academic Press, London, 1977.

98. D. Botez, "InGaAsP/InP double-heterostructure lasers: simple expressions for wave confinement, beamwidth, and threshold current over wide ranges in wavelength (1.1-1.65 μm)," *IEEE J. Quantum Electron.*, vol. QE-17, pp. 178-186, Feb. 1981.

99. J. Buus, "Analytical approximation for the reflectivity of DH lasers," *IEEE J. Quantum Electron.*, vol. QE-17, pp. 2256-2257, Dec. 1981.

100. D. Botez, "Effective refractive index and first-order-mode cutoff conditions in InGaAsP/InP DH laser structures (λ = 1.2-1.6 μm)," *IEEE J. Quantum Electron.*, vol. QE-18, pp. 865-870, May 1982.

101. H. C. Casey and M. B. Panish, *Heterostructure Lasers: Part B: Materials and Operating Characteristics,* Academic Press, New York, N.Y., 1978.

102. T. Ikegami, "Reflectivity of mode at facet and oscillation mode in double-heterostructure injection lasers," *IEEE J. Quantum Electron.*, vol. QE-8, pp. 470-476, June 1972.

103. M. A. A. Pudensi and L. G. Ferreira, "Method to calculate the reflection and transmission of guided waves," *J. Opt. Soc. Am.*, vol. 72, pp. 126-130, Jan. 1982.

104. J. K. Butler and H. Kressel, "Design curves for double-heterojunction laser diodes," *RCA Rev.*, vol. 38, pp. 543-558, Dec. 1977.

105. H. C. Casey, M. B. Panish, and J. L. Merz, "Beam divergence of the emission from double-heterostructure injection lasers," *J. Appl. Phys.*, vol. 44, pp. 5470-5475, Dec. 1973.

106. D. Botez and M. Ettenberg, "Beamwidth approximations for the fundamental mode in symmetric double-heterojunction lasers," *IEEE J. Quantum Electron.*, vol. QE-14, pp. 827-830, Nov. 1978.

107. T. Yamamoto, K. Sakai, and S. Akiba, "10,000-h continuous CW operation of $In_{1-x}Ga_xAs_yP_{1-y}$/InP DH lasers at room temperature," *IEEE J. Quantum Electron.*, vol. QE-15, pp. 684-687, Aug. 1979.

108. K. Wakita, H. Takaoka, M. Seki, and M. Fukuda, "Transmission electron microscope observation of dark defects appearing in InGaAsP/InP double heterostructure lasers aged at accelerated operation," *Appl. Phys. Lett.*, vol. 40, pp. 525-527, 15 Mar. 1982.

109. M. Fukuda, K. Takahei, G. Iwane, and T. Ikegami, "Facet degradation and passivation of InGaAsP/InP lasers," *Appl. Phys. Lett.*, vol. 41, pp. 18-21, 1 July 1982.

110. M. Morimoto, H. Imai, K. Hori, M. Takusagawa, and M. Fukuda, "Facet degradation of InGaAsP/InP double-heterostructure lasers," *Appl. Phys. Lett.*, vol. 37, pp.

1082-1084, 15 Dec. 1980.

111. H. Temkin, S. Mahajan, M. A. DiGiuseppe, and A. G. Dentai, "Optically induced catastrophic degradation in InGaAsP/InP layers," *Appl. Phys. Lett.*, vol. 40, pp. 562-565, 1 Apr. 1982.

112. "Portable Methane Detectors," *Title 30, Sub-Chapter D, Part 22,* U.S. Dept. of Commerce, Mine and Safety Administration, July 1980.

113. *American National Standard for the Safe Use of Lasers,* American National Standards Institute, Inc., New York, N.Y., 1980.

114. *Title 21, Chapter 21, Subchapter J: Radiological Health,* 40 No. 148, pp. 32252-32266, Federal Register, 31 July 1975.

115. A. Yariv, *Introduction to Optical Electronics,* Holt, Rinehart and Winston, New York, N.Y., 1976.

116. R. H. Hamstra and P. Wendland, "Noise and frequency response of silicon photodiode operational amplifier combination," *Appl. Opt.*, vol. 11, pp. 1539-1547, July 1972.

117. *Germanium photodiode application note #501,* Judson Infrared Inc., 1981.

118. D. N. Payne and W. A. Gambling, "Zero dispersion in optical fibers," *Elect. Lett.*, vol. 11, pp. 176-178, 1975.

119. H. Ando, H. Kanbe, T. Kimura, T. Yamaoka, and T. Kaneda, "Characteristics of germanium avalanche photodiodes in the wavelength region of 1-1.6 μm," *IEEE J. Quantum Electron.*, vol. QE-14, pp. 804-809, Nov. 1978.

120. T. Mikawa, S. Kagawa, T. Kaneda, T. Sakurai, H. Ando, and O. Mikami, "A low-noise n^+np germanium avalanche photodiode," *IEEE J. Quantum Electron.*, vol.

QE-17, pp. 210-216, Feb. 1981.

121. R. F. Leheny, R. E. Nahory, and M. A. Pollack, "$In_{0.53}Ga_{0.47}As$ p-i-n photodiodes for long-wavelength fibre-optic systems," *Elect. Lett.*, vol. 15, pp. 713-715, 25 Oct. 1979.

122. J. C. Campbell, A. G. Dentai, C. A. Burrus, and J. F. Ferguson, "InP/InGaAs heterojunction phototransistors," *IEEE J. Quantum Electron.*, vol. QE-17, pp. 264-269, Feb. 1981.

123. V. Diadiuk, S. H. Groves, C. E. Hurwitz, and G. W. Iseler, "Low dark-current, high gain GaInAs/InP avalanche photodetectors," *IEEE J. Quantum Electron.*, vol. QE-17, pp. 260-264, Feb. 1981.

124. T. P. Lee, C. A. Burrus, and A. G. Dentai, "InGaAs/InP p-i-n photodiodes for lightwave communications at the 0.95-1.65 μm wavelength," *IEEE J. Quantum Electron.*, vol. QE-17, pp. 232-238, Feb. 1981.

125. K. Kasahara, J. Hayashi, K. Makita, K. Taguchi, A. Suzuki, H. Nomura, and S. Matuahita, "Monolithically integrated $In_{0.53}Ga_{0.47}As$ -pin/InP-misfet photoreceiver," *Electron. Lett.*, vol. 20, pp. 314-315, 12 Apr. 1984.

126. C. Y. Chen, B. L. Kasper, and H. M. Cox, "High-sensitivity $Ga_{0.47}In_{0.53}As$ photoconductive detectors prepared by vapor phase epitaxy," *Appl. Phys. Lett.*, vol. 44, pp. 1142-1144, 15 June 1984.

127. *Technical data sheet for detector model QD,* Lasertron Corporation, Burlington, MA.

128. K. Neelakantan and S. Dattagupta, "Analysis of signal-to-noise enhancement of box-car averagers," *Pramana*, vol. 11, pp. 295-306, Sep. 1978.

129. A. G. Kjelaas, P. E. Nordal, and A. Bjerkestrand, "Scintillation and multiwavelength coherence effects in a long-path laser absorption spectrometer," *Appl. Opt.*, vol. 17, pp. 277-284, 15 Jan. 1978.

130. N. Menyuk and D. K. Killinger, "Temporal correlation measurements of pulsed dual CO_2 Lidar returns," *Opt. Lett.*, vol. 6, pp. 301-303, June 1981.

131. J. C. Petheram, "Differential backscatter from the atmospheric aerosol: the implications for IR differential absorption lidar," *Appl. Opt.*, vol. 20, pp. 3941-3946, 15 Nov. 1981.

132. J. L. Bufton, T. Itabe, and D. A. Grolemund, "Dual-wavelength correlation measurements with an airborne pulsed carbon dioxide lidar system," *Opt. Lett.*, vol. 7, pp. 584-586, Dec. 1982.

133. S. F. Clifford and L. Lading, "Monostatic diffraction-limited LIDARs: the impact of optical refractive turbulence," *Appl. Opt.*, vol. 22, pp. 1696-1701, 1 June 1983.

134. D. K. Killinger and N. Menyuk, "Effect of turbulence-induced correlation on laser remote sensing errors," *Appl. Phys. Lett.*, vol. 38, pp. 968-970, 15 June 1981.

135. D. K. Killinger and N. Menyuk, "Remote probing of the atmosphere using a CO_2 DIAL system," *IEEE J. Quantum Electron.*, vol. QE-17, pp. 1917-1929, Sep. 1981.

136. N. Menyuk, D. K. Killinger, and C. R. Menyuk, "Limitations of signal averaging due to temporal correlation in laser remote-sensing measurements," *Appl. Opt.*, vol. 21, pp. 3377-3383, 15 Sep. 1982.

137. N. Menyuk and D. K. Killinger, "Assessment of relative error sources in IR DIAL measurement accuracy," *Appl. Opt.*, vol. 22, pp. 2690-2698, 1 Sep. 1983.

138. R. C. Harney, "Laser prf considerations in differential absorption lidar applications," *Appl. Opt.*, vol. 22, pp. 3747-3750, 1 Dec. 1983.

139. P. A. Pincus, R. A. Elliott, and J. R. Kerr, "Conditional fading statistics of scintillation," *J. Opt. Soc. Am.*, vol. 68, pp. 756-760, June 1978.

140. R. Ludeke and E. P. Harris, "Tunable GaAs laser in an external dispersive cavity," *Appl. Phys. Lett.*, vol. 20, pp. 499-500, 15 June 1972.

141. J. A. Rossi, S. R. Chinn, and H. Heckscher, "High-power narrow-linewidth operation of GaAs diode lasers," *Appl. Phys. Lett.*, vol. 23, pp. 25-27, 1 July 1973.

142. D. Akkerman, A. P. Bogatov, P. G. Eliseev, Z. Raab, and B. N. Sverdlov, "Injection laser with a diffraction grating in its resonator," *Sov. J. Quant. Electron.*, vol. 4, pp. 626-628, Nov. 1974.

143. H. Heckscher and J. A. Rossi, "Flashlight-size external cavity semiconductor laser with narrow-linewidth tunable output," *Appl. Opt.*, vol. 14, pp. 94-96, Jan. 1975.

144. E. M. Philipp-Rutz, "Spatially coherent radiation from an array of GaAs lasers," *Appl. Phys. Lett.*, vol. 26, pp. 475-477, 15 Apr. 1975.

145. C. Voumard, "External-cavity-controlled 32-MHz narrow-band CW GaAlAs-diode lasers," *Opt. Lett.*, vol. 1, pp. 61-63, Aug. 1977.

146. H. Sato, K. Itoh, M. Fukai, and N. Suzuki, "Single longitudinal mode control of semiconductor lasers by rectangular conical diffractor system for wavelength-division-multiplexing transmission," *IEEE J. Quantum Electron.*, vol. QE-18, pp. 328-332, Mar. 1982.

147. H. Sato, H. Asakura, M. Fukai, and N. Suzuki, "Design of nondispersion optical feedback system using diffraction grating for semiconductor laser multiple longitudinal modes control," *IEEE J. Quantum Electron.*, vol. QE-18, pp. 155-157, Feb. 1982.

148. R. Wyatt and W. J. Devlin, "10 kHz linewidth 1.5 μm InGaAsP external cavity laser with 55nm tuning range," *Elect. Lett.*, vol. 19, pp. 110-111, 3 Feb. 1983.

149. J. R. Andrews, "Single mode operation of a current pulsed GaAlAs laser with dispersive external feedback," *Appl. Phys. Lett.*, vol. 44, pp. 5-7, 1 Jan. 1984.

150. P. D. Wright, J. J. Coleman, N. Holonyak, M. J. Ludowise, and G. E. Stillman, "Homogeneous or inhomogeneous line broadening in a semiconductor laser: observations on $In_{1-x}Ga_xP_{1-z}As_z$ double heterojunctions in an external grating cavity," *Appl. Phys. Lett.*, vol. 29, pp. 18-20, 1 July 1976.

151. T. Kanada and K. Nawata, "Injection laser characteristics due to reflected optical power," *IEEE J. Quantum Electron.*, vol. QE-15, pp. 559-565, July 1979.

152. R. Lang and K. Kobayashi, "External optical feedback effects on semiconductor injection laser properties," *IEEE J. Quantum Electron.*, vol. QE-16, pp. 347-355, Mar. 1980.

153. L. A. Glasser, "A Linearized Theory for the diode laser in an external cavity," *IEEE J. Quantum Electron.*, vol. QE-16, pp. 525-531, May 1980.

154. Y. Mitsuhashi, T. Morikawa, J. Shimada, K. Sakurai, and S. Mitsutsuka, "Polarization-rotated optical feedback in self-coupled optical pickup," *Opt. Comm.*, vol. 34, pp. 309-310, Sep. 1980.

155. S. Saito and Y. Yamamoto, "Direct observation of Lorentzian lineshape of semiconductor laser and linewidth reduction with external grating feedback," *Elect. Lett.*, vol. 17, pp. 325-327, 30 Apr. 1981.

156. M. Fleming and A. Mooradian, "Spectral characteristics of external-cavity controlled semiconductor lasers," *IEEE J. Quantum Electron.*, vol. 17, pp. 44-59, Jan. 1981.

157. L. Goldberg, H. F. Taylor, A. Dandridge, J. F. Weller, and R. O. Miles, "Spectral characteristics of semiconductor lasers with optical feedback," *IEEE J. Quantum Electron.*, vol. QE-18, pp. 555-563, Apr. 1982.

158. R. P. Salathe, "Diode lasers coupled to external resonators," *Appl. Phys.*, vol. 20, pp. 1-18, 1979.

159. T. Yabuzaki, A. Ibaragi, H. Hori, M. Kitano, and T. Ogawa, "Frequency-locking of a GaAlAs Laser to a doppler-free spectrum of the Cs—D_2 line," *Japan. Jnl. Appl. Phys.*, vol. 20, pp. 451-453, June 1981.

160. S. Yamaguchi and M. Suzuki, "Frequency locking of an InGaAsP semiconductor laser to the first overtone vibration-rotation lines of hydrogen fluoride," *Appl. Phys. Lett.*, vol. 41, pp. 1034-1036, 1 Dec. 1982.

161. E. Mohn, "Properties of a GaAs laser coupled to an external cavity," *1968 Symposium on GaAs,* pp. 101-109, 1968.

162. E. Hecht and A. Zajac, *Optics,* Addison-Wesley, Reading, MA, 1976.

163. V. N. Smiley, "Conditions for zero reflectance of thin dielectric films on laser materials," *J. Opt. Soc. Am.*, vol. 58, pp. 1469-1475, Nov. 1968.

164. A. Yariv, "Coupled-mode theory for guided-wave optics," *IEEE J. Quantum Electron.*, vol. QE-9, pp. 919-933, Sep. 1973.

165. R. G. Hunsperger, A. Yariv, and A. Lee, "Parallel end-butt coupling for optical integrated circuits," *Appl. Opt.*, vol. 16, pp. 1026-1032, Apr. 1977.

166. C. T. Mueller, C. T. Sullivan, W. S. C. Chang, D. G. Hall, J. D. Zino, and R. R. Rice, "An analysis of the coupling of an injection laser diode to a planar $LiNbO_3$ waveguide," *IEEE J. Quantum Electron.*, vol. QE-16, pp. 363-372, Mar. 1980.

167. W. L. Emkey, "Optical coupling between single-mode semiconductor lasers and strip waveguides," *Jour. Lightw. Tech.*, vol. LT-1, pp. 436-443, June 1983.

168. M. Born and E. Wolf, *Principles of Optics,* Pergamon Press, New York, N.Y., 1975. Fifth Edition

169. W. G. Driscoll, Ed., *Handbook of Optics,* McGraw-Hill, New York, 1978.

170. W. G. Fastie, "A small plane grating monochromator," *J. Opt. Soc. Am.*, vol. 42, pp. 641-647, Sep. 1952.

171. A. S. Filler, "Stigmatic Ebert-type plane grating mounting," *J. Opt. Soc. Am.*, vol. 54, 1964.

172. W. T. Welford, "Stigmatic Ebert-type plane grating mounting," *J. Opt. Soc. Am.*, vol. 53, p. 766, 1963.

173. V. L. Chupp and P. C. Grantz, "Coma cancelling monochromator with no slit mismatch," *Appl. Opt.*, vol. 8, pp. 925-929, May 1969.

174. M. A. Gil and J. M. Simon, "New plane grating monochromator with off-axis parabolical mirrors," *Appl. Opt.*, vol. 22, pp. 152-158, 1 Jan. 1983.

175. J. M. Lerner and A. Thevenon, "Optimizing grating-based systems," *Lasers and Applications*, pp. 89-93, Jan. 1984.

176. *A Designers Guide to Diamond Machined Optics,* Pneumo Precision, Inc., Keene, N. H., Apr. 1983.

177. C. B. Swan, "Improved performance of silicon avalanche oscillators mounted on diamond heat sinks," *IEEE Proc.*, pp. 1617-1618, 1967.

178. R. Berman, *Diamonds as heat sinks-a review,* D. Drukker & Zn., Amsterdam, 1970.

179. E. A. Burgemeister, "Thermal resistance at metal/diamond interfaces in relation

to the mounting of microwave diodes," *J. Phys. D: Appl. Phys.*, vol. 10, pp. 1923-1929, 1977.

180. E. A. Burgemeister, "Thermal conductivity of natural diamond between 320 and 450 K," *Physica*, vol. 93B, pp. 165-179, 1978.

181. E. A. Burgemeister, "Thermal conductivity measurements by means of radiation thermometry ," *Proceedings SPIE*, vol. 197, pp. 305-310, Soc. Photo. Intrum. Eng., 1979.

182. J. A. Amick, G. L. Schnable, and J. L. Vossen, "Deposition techniques for dielectric films on semiconductor devices," *J. Vac. Sci. Technol.*, vol. 14, pp. 1053-1063, Sep./Oct. 1977.

183. H. A. Macleod and A. F. Turner, "New thin-film coating processes," *Opt. Spect.*, pp. 67-68, Sep. 1981.

184. O. A. Weinreich, "Antireflection films on GaAs electroluminescent diodes," *J. Electrochem. Soc.*, vol. 110, pp. 1124-1126, Nov. 1963.

185. T. Yamamoto and K. Kawamura, "SiO evaporation on a GaAs electroluminescent diode," *Proc. IEEE*, vol. 54, pp. 1967-1968, Dec. 1966.

186. H. D. Edmonds, C. DePalma, and E. P. Harris, "Preparation and properties of SiO antireflection coatings for GaAs injection lasers with external resonators," *Appl. Opt.*, vol. 10, pp. 1591-1596, July 1971.

187. M. Ettenberg, H. S. Sommers, H. Kressel, and H. F. Lockwood, "Control of facet damage in GaAs laser diodes," *Appl. Phys. Lett.*, vol. 18, pp. 571-573, 15 June 1971.

188. G. Eisenstein and L. W. Stulz, "High quality antireflection coatings on laser facets by sputtered silicon nitride," *Appl. Opt.*, vol. 23, pp. 161-164, 1 Jan 1984.

189. G. Hass, "Preparation, structure, and applications of thin films of silicon monoxide and titanium dioxide," *Jour. Am. Ceram. Soc.*, vol. 33, pp. 353-360, Dec. 1950.

190. G. Hass and C. D. Salzberg, "Optical properties of silicon monoxide in the wavelength region from 0.24 to 14.0 microns," *J. Opt. Soc. Am.*, vol. 44, pp. 181-187, Mar. 1954.

191. G. Hass, "Filmed surfaces for reflecting optics," *J. Opt. Soc. Am.*, vol. 45, pp. 945-952, Nov. 1955.

192. A. P. Bradford, G. Hass, M. McFarland, and E. Ritter, "Effect of ultraviolet irradiation on the optical properties of silicon oxide films," *Appl. Opt.*, vol. 4, pp. 971-976, Aug. 1965.

193. V. N. Smiley, "Mismatch of single layer antireflection coatings on laser materials," *Appl. Opt.*, vol. 7, pp. 986-987, May 1968.

194. G. Eisenstein, "Theoretical design of single-layer antireflection coatings on laser facets," *B. L. T. J.*, vol. 63, pp. 357-364, Feb. 1984.

195. R. W. Hoffman, "The Mechanical Properties of Thin Films," in *The Use of Thin Films in Physical Investigations*, ed. J. C. Anderson, pp. 261-281, Academic Press, New York, N. Y., 1966.

196. J. R. Vig, "UV/Ozone Cleaning of Surfaces: A Review," in *Surface Contamination*, ed. K. L. Mittal, vol. 1, pp. 235-254, Plenum Press, New York, N. Y..

197. W.W. Balwanz, "Plasma Cleaning of Surfaces," in *Surface Contamination*, ed. K. L. Mittal, vol. 1, pp. 255-270, Plenum Press, New York, N. Y..

198. R. K. DeFreez, T. L. Paoli, M. Bernstein, and R. D. Burnham, "CW operation of a cleaved-coupled-cavity array of phased-locked GaAlAs lasers," *Electron. Lett.*, vol. 21, pp. 241-242, 14 Mar. 1985.

199. E. M. Pugh and G. H. Winslow, *The Analysis of Physical Measurements,* Addison-Wesley, Reading, MA, 1966.

APPENDIX A

This appendix lists the computer source program used to generate data for plots of optical transmission versus wavenumber, for a specified methane concentration, and for a specified spectral resolution. Plots for the P, Q, and R branches of the $2\nu_3$ methane absorption so generated are shown in Figures 3 through 5 in Section 3.

This program is a modification of a listing presented in an AFCRL document[65].

```
LEVEL 2.3.0 (JUNE 78)                    OS/360  FORTRAN H EXTENDED                    DATE 83.226/17.36.32        PAGE   1

REQUESTED OPTIONS:

OPTIONS IN EFFECT: NAME(MAIN) OPTIMIZE(2) LINECOUNT(60) SIZE(MAX) AUTODBL(NONE)
                   SOURCE EBCDIC NOLIST NODECK OBJECT MAP NOFORMAT GOSTMT NOXREF NOALC NOANSF TERM IBM FLAG(I)
                  C                                                                                  MXT00010
                         PROGRAM MXTRNS                                                              MXT00020
      ISN 0002           IMPLICIT REAL*8 (A-H,O-Z)                                                   MXT00030
      ISN 0003           DIMENSION GNU(5000), S(5000), ALPHA(5000), COP(5000)                        MXT00040
      ISN 0004           DIMENSION OPD(5000), FMI(5000), TRANS(5000)                                 MXT00050
      ISN 0005           DEFINE FILE 1(20000,80,E,I11)                                               MXT00060
      ISN 0006           DEFINE FILE 7(5000,110,L,I22)                                               MXT00070
      ISN 0007           DEFINE FILE 8(5009,110,E,I22)                                               MXT00080
      ISN 0008           DEFINE FILE 9(5000,110,E,I22)                                               MXT00090
      ISN 0009           DEFINE FILE 10(5000,110,E,I22)                                              MXT00100
      ISN 0010           DEFINE FILE 11(5000,110,E,I22)                                              MXT00110
      ISN 0011           DEFINE FILE 12(5000,110,E,I22)                                              MXT00120
      ISN 0012           DEFINE FILE 13(5000,110,E,I22)                                              MXT00130
      ISN 0013           DEFINE FILE 14(5000,110,E,I22)                                              MXT00140
      ISN 0014           DEFINE FILE 15(5000,110,E,I22)                                              MXT00150
      ISN 0015           REAL*8  LAMBDA                                                              MXT00160
      ISN 0016           INTEGER*4  CNTR                                                             MXT00170
      ISN 0017           NAMELIST/NAM1/P,T/NAM2/W/NAM3/V1,V2,DV,BOUND,A,DELV/NAM4/II                 MXT00180
      ISN 0018           NAMELIST/NAM5/V1,V2,A                                                       MXT00190
                  C                                                                                  MXT00200
                  C                                                                                  MXT00210
                  C                                                                                  MXT00220
                  C                                                                                  MXT00230
                  C                                                                                  MXT00240
                  C      PROGRAM BY RICK DEFREEZ                                                     MXT00250
                  C                                                                                  MXT00260
                  C                                                                                  MXT00270
                  C      THIS PROGRAMS GENERATES A TRANSMITTANCE SPECTRUM WITH OUTPUT                MXT00280
                  C      RESULTS PRINTED EVERY DELV WAVENUMBERS BETWEEN THE INITIAL                  MXT00290
                  C      FREQUENCY, V1, AND THE FINAL FREQUENCY,V2.                                  MXT00300
                  C      CALCULATIONS ARE PERFORMED FOR A UNIFORM CONSTANT PRESSURE, CON-            MXT00310
                  C      STANT TEMPERATURE PATH CONTAINING THE MOLECULAR SPECIES IN THE              MXT00320
                  C      REFERENCED FILE IN ARBITRARY AMOUNTS.  MOLECULAR ABUNDANCES MUST            MXT00330
                  C      BE SPECIFIED IN THE UNITS: (MOLECULES/CM**2).  MONOCHROMATIC                MXT00340
                  C      CALCULATIONS ARE MADE AT DV FREQUENCY INTERVALS AND A TRIANGULAR            MXT00350
                  C      SLIT FUNCTION OF HALF-WIDTH, A, IS CONVOLVED WITH THE MONO-                 MXT00360
                  C      CHROMATIC RESULTS.                                                          MXT00370
      ISN 0019    14     DEPTH=.0001                                                                 MXT00380
      ISN 0020           PI=3.141592653                                                              MXT00390
      ISN 0021           SUM=0.0                                                                     MXT00400
      ISN 0022           IV=1                                                                        MXT00410
                  C      READ INPUT PARAMETERS (P=PRESSURE IN MBARS , T=TEMPERATURE IN               MXT00420
                  C      K).  V1 AND V2 ARE THE FREQUENCY LIMITS FOR WHICH OUTPUT RESULTS            MXT00430
                  C      ARE REQUIRED.  DV IS MONOCHROMATIC FREQUENCY INCREMENT.  BOUND              MXT00440
                  C      IS THE FREQUENCY FORM ANY LINE CENTER BEYOND WHICH THE LINE                 MXT00450
                  C      WILL BE NEGLECTED.  A IS THE HALF-WIDTH OF A TRIANGULAR SLIT                MXT00460
                  C      FUNCTION.  DELV IS THE FREQUENCY INCREMENT OF CONVOLVED OUTPUT              MXT00470
                  C      TRANSMITTANCE RESULTS.                                                      MXT00480
                  C                                                                                  MXT00490
      ISN 0023           IF(II.EQ.1) GO TO 44                                                        MXT00500
      ISN 0025           CNTR=7                                                                      MXT00510
      ISN 0026           WRITE (6,1009)                                                              MXT00520
      ISN 0027           READ(5,NAM1)                                                                MXT00530
      ISN 0028           WRITE (6,NAM1)
```

```
LEVEL 2.3.0 (JUNE 78)          MAIN          OS/360  FORTRAN H EXTENDED          DATE 80.224/17.36.32          PAGE   2

  ISN 0029              WRITE(6,1010)                                                           MXT00540
  ISN 0030              READ(5,NAM2)                                                            MXT00550
  ISN 0031              WRITE(6,NAM2)                                                           MXT00560
  ISN 0032              WRITE(6,1020)                                                           MXT00570
  ISN 0033              READ(5,NAM3)                                                            MXT00580
  ISN 0034              WRITE(6,NAM3)                                                           MXT00590
  ISN 0035              GO TO 24                                                                MXT00600
  ISN 0036        44    CNTR=CNTR+1                                                             MXT00610
  ISN 0037              WRITE(6,2400)                                                           MXT00620
  ISN 0038              READ(5,NAM5)                                                            MXT00630
  ISN 0039              WRITE(6,NAM5)                                                           MXT00640
                  C                                                                             MXT00650
                  C                                                                             MXT00660
                  C                                                                             MXT00670
                  C     IF (A*2/DV+1.GT.5000) CALCULATION CANNOT BE DONE.                       MXT00680
                  C     IF THERE ARE READ MORE THAN 5000 LINES IN A FREQUENCY RANGE OF          MXT00690
                  C     2(A+BOUND) CALCULATION CANNOT BE DONE.                                  MXT00700
                  C                                                                             MXT00710
                  C                                                                             MXT00720
                  C                                                                             MXT00730
  ISN 0040        24    VBOT=V1-A-BOUND                                                         MXT00740
  ISN 0041              VTOP=V2+A+BOUND                                                         MXT00750
  ISN 0042              I=1                                                                     MXT00760
  ISN 0043              DO 9 K=1,20000                                                          MXT00780
  ISN 0044                READ(1'K,95) GNU(I), S(I), ALPHA(I), EDP(I)                           MXT00790
  ISN 0045                IF (GNU(I).LT.VBOT) GO TO 9                                           MXT00800
  ISN 0047                PATH =S(I)*W/(PI*.06*P/1013.0)                                        MXT00810
  ISN 0048                IF (PATH.LT.DEPTH) GO TO 9                                            MXT00820
  ISN 0050                IF (GNU(I).GT.VTOP) GO TO 11                                          MXT00830
  ISN 0052                I=I+1                                                                 MXT00840
  ISN 0053         9    CONTINUE                                                                MXT00850
  ISN 0054        11    II=I                                                                    MXT00860
  ISN 0055              WRITE(6,97) VBOT,VTOP,GNU(II),II                                        MXT00870
  ISN 0056              I5=1                                                                    MXT00880
  ISN 0057              V2P=GNU(II)-BOUND-A                                                     MXT00890
  ISN 0058              I5=1                                                                    MXT00900
  ISN 0059              PO=1013.00                                                              MXT00910
  ISN 0060              TO=296.00                                                               MXT00920
  ISN 0061              CS1=(TO-T)/(TO*T*.5986)                                                 MXT00930
                  C                                                                             MXT00940
                  C     ROTATIONAL PARTITION FUNCTION IS DEFINED BELOW.                         MXT00950
                  C                                                                             MXT00960
  ISN 0062              CS2=(TO/T)**1.5                                                         MXT00970
  ISN 0063              CA=((TO/T)**.5)*(P/PO)                                                  MXT00980
                  C                                                                             MXT00990
                  C     TEMPERATURE DEPENDENCE OF ALL LINE INTENSITIES COMPUTED HERE            MXT01000
                  C                                                                             MXT01010
  ISN 0064              DO 23 I=1,II                                                            MXT01020
  ISN 0065                S(I)=S(I)*CS2*DEXP(-EDP(I)*CS1)                                       MXT01030
  ISN 0066                ALPHA(I)=ALPHA(I)*CA                                                  MXT01040
  ISN 0067        23    CONTINUE                                                                MXT01050
  ISN 0068              V=V1-A                                                                  MXT01060
  ISN 0069        25    CAV1=0.0                                                                MXT01070
  ISN 0070              SUM1=0.0                                                                MXT01080
                  C                                                                             MXT01090
                  C     DETERMINE INDICES (I5 AND I6) INDICATING WHICH SPECTRAL LINES           MXT01100
                  C     ARE TO BE USED IN THE CALCULATION AT FREQUENCY V.                       MXT01110
                  C                                                                             MXT01120
```

```
ISN 0071            DO 33 I=I5,I1                                                MXT01130
ISN 0072              IF(V-BOUND-GNU(I))29,29,33                                 MXT01140
ISN 0073       33   CONTINUE                                                     MXT01150
ISN 0074            GO TO 34                                                     MXT01160
ISN 0075       29   I5=I                                                         MXT01170
ISN 0076            GO TO 35                                                     MXT01180
ISN 0077       34   I5=I1                                                        MXT01190
ISN 0078            GO TO 49                                                     MXT01200
ISN 0079       35   DO 39 J=I5,I1                                                MXT01210
ISN 0080              IF(V+BOUND-GNU(J)) 37,37,39                                MXT01220
ISN 0081       37     I6=J-1                                                     MXT01230
ISN 0082              GO TO 43                                                   MXT01240
ISN 0083       39   CONTINUE                                                     MXT01250
ISN 0084            I6=I1                                                        MXT01260
              C                                                                  MXT01270
              C     COMPUTE THE OPTICAL DEPTH AND TRANSMITTANCE AT FREQUENCY V.  MXT01280
              C                                                                  MXT01290
ISN 0085       43   DO 45 I=I5,I6                                                MXT01300
ISN 0086              Z=DABS(V-GNU(I))                                           MXT01310
ISN 0087              SUM1=S(I)*ALPHA(I)/(Z**2+ALPHA(I)**2)                      MXT01320
ISN 0088              CAV1=CAV1+SUM1                                             MXT01330
ISN 0089        45  CONTINUE                                                     MXT01340
ISN 0090            CAV=CAV1*W                                                   MXT01350
ISN 0091            OPD(IV)=CAV*0.3183                                           MXT01360
ISN 0092            GO TO 51                                                     MXT01370
ISN 0093        49  OPD(IV)=0.0                                                  MXT01380
ISN 0094        51  OPD(IV)=DEXP(-OPD(IV))                                       MXT01390
ISN 0095            IF((V+DV).GT.V2P) GO TO 53                                   MXT01400
ISN 0097            IF(V.GE.V2+A) GO TO 53                                       MXT01410
ISN 0099            IF(IV.GE.5000) GO TO 53                                      MXT01420
ISN 0101            IV=IV+1                                                      MXT01430
ISN 0102            V=V+DV                                                       MXT01440
ISN 0103            GO TO 25                                                     MXT01450
              C                                                                  MXT01460
              C     AT THIS POINT, CYCLE BACK TO STATEMENT 25 AND COMPUTE THE    MXT01470
              C     MONOCHROMATIC TRANSMITTANCE AT V+DV.                         MXT01480
              C     IF STATEMENT 53 IS REACHED, ALL POSSIBLE MONOCHROMATIC TRANS- MXT01490
              C     MITTANCE VALUES HAVE BEEN COMPUTED, AND THE SLIT FUNCTION CON- MXT01500
              C     VOLUTION WILL NOW BE PERFORMED IN LOOP 57                    MXT01510
              C                                                                  MXT01520
              C                                                                  MXT01530
ISN 0104       53   FREQ=V1                                                      MXT01540
ISN 0105            FINAL=V1+5000.*DV-A-DELV                                     MXT01550
ISN 0106            V=V1-A                                                       MXT01560
ISN 0107            JFNU=1                                                       MXT01570
ISN 0108            L=DELV/DV+.01                                                MXT01580
ISN 0109            IA=1                                                         MXT01590
ISN 0110       55   SUM=0.0                                                      MXT01600
ISN 0111            DO 57 I=IA,IV                                                MXT01610
ISN 0112              SUM=SUM+(A-DABS(V-FREQ))*OPD(I)                            MXT01620
ISN 0113              V=V+DV                                                     MXT01630
ISN 0114              IF(V-(FREQ+A)) 57,59,59                                    MXT01640
ISN 0115       57   CONTINUE                                                     MXT01650
ISN 0116       59   TRANS(JFNU)=SUM*DV/(A*A)                                     MXT01660
ISN 0117            FNU(JFNU)=FREQ                                               MXT01670
ISN 0118            IF(FREQ.GT.V2) GO TO 61                                      MXT01680
ISN 0120            IF(FREQ.GT.V2P) GO TO 61                                     MXT01690
ISN 0122            IF(FREQ.GE.FINAL) GO TO 61                                   MXT01700
```

```
LEVEL 2.3.0 (JUNE 78)           MAIN          OS/360  FORTRAN H EXTENDED           DATE 80.224/17.36.32       PAGE   4

                                                                                           MXT01710
  ISN 0124          FREQ=FREQ+DELV                                                         MXT01720
  ISN 0125          IF(JFNU.GE.5000) GO TO 61                                              MXT01730
  ISN 0127          JFNU=JFNU+1                                                            MXT01740
  ISN 0128          IA=IA+L                                                                MXT01750
  ISN 0129          V=FREQ-A                                                               MXT01760
  ISN 0130          GO TO 55                                                               MXT01770
              C                                                                            MXT01780
              C     CONVOLVED TRANSMITTANCE RESULTS NOW PRINTED OUT                        MXT01790
              C                                                                            MXT01800
  ISN 0131     61   WRITE(CNTR*2,2002)W                                                    MXT01810
  ISN 0132          WRITE(CNTR*3,2003)P,T                                                  MXT01820
  ISN 0133          WRITE(CNTR*4,2004)V1,V2                                                MXT01830
  ISN 0134          WRITE(CNTR*5,2005)A,BOUND                                              MXT01840
  ISN 0135          WRITE(CNTR*6,2006)DV,DELV                                              MXT01850
  ISN 0136          JFNUA=JFNU+5                                                           MXT01860
  ISN 0137          DO 64 J=7,JFNUA                                                        MXT01870
  ISN 0138            LAMBDA=1.0E4/FNU(J-6)                                                MXT01880
  ISN 0139            WRITE(CNTR*J,105) FNU(J-6),LAMBDA,TRANS(J-6)                         MXT01890
  ISN 0140     64   CONTINUE                                                               MXT01900
  ISN 0141          IF(FREQ.GE.V2) GO TO 75                                                MXT01910
  ISN 0143          IF(JFNU.GE.5000) GO TO 65                                              MXT01920
  ISN 0145          IF(FREQ.GE.FINAL) GO TO 63                                             MXT01930
  ISN 0147          GO TO 75                                                               MXT01940
  ISN 0148     63   V1=FINAL+DELV                                                          MXT01950
  ISN 0149          IS=1                                                                   MXT01960
  ISN 0150          IV=1                                                                   MXT01970
  ISN 0151          JFNU=1                                                                 MXT01980
  ISN 0152          V=V1-A                                                                 MXT01990
  ISN 0153          GO TO 25                                                               MXT02000
  ISN 0154     65   IA=IA+L                                                                MXT02010
              C                                                                            MXT02020
              C     IF STATEMENT 65 IS REACHED, ADDITIONAL MONOCHROMATIC CALCULATIONS      MXT02030
              C     ARE REQUIRED TO SATISFY THE TOTAL FREQUENCY RANGE OVER WHICH           MXT02040
              C     CONVOLVED RESULTS ARE REQUIRED                                         MXT02050
              C                                                                            MXT02060
  ISN 0155          JFNU=1                                                                 MXT02070
  ISN 0156          V=FREQ-A                                                               MXT02080
  ISN 0157          GO TO 55                                                               MXT02090
  ISN 0158     75   WRITE (6,1200)                                                         MXT02100
  ISN 0159          READ(5,NAM4)                                                           MXT02110
  ISN 0160          IF(II.EQ.1) GO TO 14                                                   MXT02120
  ISN 0162          CALL EXIT                                                              MXT02130
  ISN 0163          STOP                                                                   MXT02140
  ISN 0164     95   FORMAT(F10.3,E10.3,F5.3,F10.1)                                         MXT02150
  ISN 0165     97   FORMAT(1X,'VBOT=',F12.3,'VTOP=',F12.3,'GNU=',F12.3,'II=',I8)           MXT02160
  ISN 0166    105   FORMAT(F10.3,F10.5,E12.5)                                              MXT02170
  ISN 0167   1000   FORMAT(' INPUT P,T: E12.5,F7.2  NAM1')                                 MXT02180
  ISN 0168   1010   FORMAT(1X,'INPUT CONCENTRATION IN MOLECULES/CM**2:F10.3  NAM2')        MXT02190
  ISN 0169   1020   FORMAT(1X,'INPUT F10.3:V1,V2,DV,BOUND,A,DELV   NAM3')                  MXT02200
  ISN 0170   1200   FORMAT(1X,'DO YOU WISH TO TRY NEW FREQUENCY BOUNDS AND A NEW           MXT02210
                   CBANDWIDTH? NAM4  II=1 FOR YES')                                        MXT02220
  ISN 0171   2002   FORMAT(40X,'CONCENTRATION=',E10.3)                                     MXT02230
  ISN 0172   2003   FORMAT(40X,'PRESSURE=',E12.5,5X,'TEMP=',F7.2)                          MXT02240
  ISN 0173   2004   FORMAT(40X,'NU LOW=',F10.3,5X,'NU HIGH=',F10.3)                        MXT02250
  ISN 0174   2005   FORMAT(40X,'BANDWIDTH=',F10.3,5X,'BOUND=',F10.1)                       MXT02260
  ISN 0175   2006   FORMAT(40X,'DV=',F10.3,5X,'DELV=',F10.3)                               MXT02270
  ISN 0176   2400   FORMAT (1X,'INPUT V1,V2,A   NAM5')                                     MXT02280
  ISN 0177          END
```

APPENDIX B

This appendix presents a safety calculation for a 1.6 μm collimated repetitively pulsed diode laser. It is based on the "American National Standard for the Safe Use of Lasers"[113]. The explanation below is paraphrased from Section B.3.1.2 of that document. The calculation presented is similar to Example 4 therein.

To determine the maximum safe exposure for a repetitively pulsed laser, the wavelength, PRF, duration of a single pulse, and duration of a complete exposure must be known. This determination requires two analyses and a conclusion, Steps 1 and 2 and Step 3, respectively, in the following calculation.

The calculation determines the intrabeam direct-viewing exposure for a $In_{0.53}Ga_{0.47}As/InP$ ($\lambda \approx 1.6\ \mu m$) laser of pulse duration (τ) equal to 100 ns and PRF = 10 kHz. Since the 1.6 μm wavelength light will not cause a natural eye aversion response, as a visible-wavelength laser would, a 1 second exposure duration (T) is assumed.

Step 1. Individual Pulse Limitation

This step requires the calculation of the maximum exposure based on the limitation that a single-pulse exposure shall not exceed the single pulse maximum permissible exposure (MPE) (ANSI Sections 8.5.1.1 and 8.5.1.5) multiplied by a correction factor (F_1) of ANSI Figure 12. From that figure, F = 0.06 for a PRF = 10 kHz. The maximum exposure for an individual pulse is given by

$$H_i = F_1(\mathrm{MPE}) = (0.06)(10^{-2}\ \mathrm{Jcm}^{-2}) = 6.0\mathrm{X}10^{-4}\ \mathrm{Jcm}^{-2}. \tag{B.1}$$

On this basis, the maximum exposure for a train of pulses is given by

$$H = H_i(\mathrm{PRF})T = (6.0\mathrm{X}10^{-4})(10^{3}\ \mathrm{Hz})(1\ \mathrm{Sec}) = 6\mathrm{X}10^{-1}\ \mathrm{Jcm}^{-2}. \tag{B.2}$$

Step 2. Average Power Limitation

The average power limitation requires the calculation of the total radiant exposure for the total pulse duration. From ANSI Figure 6, for T = 1 Sec the maximum exposure is given by

$$H = 5.6X10^{-1}\ Jcm^{-2}. \tag{B.3}$$

Step 3. Conclusion

Comparing the results of Step 1 and Step 2, the more restrictive limitation applies. Step 2 is more restrictive and hence applicable. This implies that the maximum single pulse exposure is given by

$$H_i = 5.6X10^{-5}\ Jcm^{-2}. \tag{B.4}$$

This result then gives a peak power density for each pulse

$$D_p = \frac{H_i}{\tau} = \frac{5.5X10^{-5}\ Jcm^{-2}}{10^{-7}\ Sec} = 550\ Wcm^{-2}. \tag{B.5}$$

Assuming a 1 mm laser beam diameter (ANSI Section 3.2.3.3), the resulting peak power is

$$P_p = D_p \pi \frac{D^2}{4} = 4.3\ W \tag{B.6}$$

where D is the beam diameter. This power value is the upper limit to exempt laser status.

APPENDIX C

Standard expressions [115] for, and numerical values of, the various detection noise sources of Section 5 are presented in this appendix. Here it is assumed that the detection system views, in addition to signal backscattered from coal dust, a Lambertian blackbody wall. The wall is assumed to be at temperature of 20°C. The optical power received by the detection system is given by

$$P_{r,BB} = W_{\Delta\lambda} A \Omega_o \Delta\lambda \epsilon \tag{C.1}$$

where $W_{\Delta\lambda}$ is the spectral blackbody radiance, A is the area of the sources seen, Ω_o is the solid angle of the receiver optics subtended at the source, $\Delta\lambda$ is the spectral bandwidth of the receiving system ($\approx$10 nm), and ϵ is the source emittance which is assumed to be $\frac{1}{\pi}$. This implies

$$P_{r,BB} = 1\text{x}10^{-13}\text{watts} \tag{C.2}$$

where numerical values typical to the HRL methane detection system have been used. The calculated optical power yields the following background averaged squared noise current:

$$\overline{i_B^2} = \frac{3e^2\, P_{r,BB}\, \eta\, \Delta\nu}{h\nu} = 3\text{x}10^{-32}\, \Delta\nu\ \text{Amps}^2 \tag{C.3}$$

where e is the electronic charge, η is the detector efficiency ($\approx$0.5), $\Delta\nu$ is the detection system electronic bandwidth in Hz, $h\nu$ is the laser photon energy, and where 100% optical efficiency has been assumed. An implicit assumption of no artificial light sources in the detector field of view has also been made.

The averaged squared detector dark current for photodiodes, which are typically used in the near infrared, is given by

$$\overline{i_D^2} = 2e\, i_d\, \Delta\nu = 3x10^{-19}\, i_d\, \Delta\nu \text{ Amps}^2 \tag{C.4}$$

where i_d is the detector dark current in Amps.

The averaged squared signal shot current is given by

$$\overline{i_{SN}^2} = \frac{3e^2\, P_r\, \eta\, \Delta\nu}{h\nu} = 3x10^{-28}\, \Delta\nu \text{ Amps}^2 \tag{C.5}$$

where a returned optical power, $P_r = 10^{-9}$ watts is assumed.

The averaged squared load and amplifier current noise for a voltage amplifying circuit is given by

$$\overline{i_A^2} = \frac{4K_B\, T_e\, \Delta\nu}{R_L} \tag{C.6}$$

where R_L is the load resistance, K_B is the Boltzmann constant, and the equivalent temperature is given by

$$T_e \approx (F)(290^\circ K) \tag{C.7}$$

where F is the noise figure of the amplifier. A typical value of good amplifiers is $F = 1.3$; $T_e \approx 380^\circ K$. R_L is limited by the system time constant, τ, through the relation

$$\tau = R_L C \tag{C.8}$$

where C is the total amplifier input capacitance. This implies

$$R_L = \frac{1}{2\Delta\nu C} \;. \tag{C.9}$$

Thus the averaged squared noise current is given by

$$\overline{i_A^2} = 8K_BT_eC(\Delta\nu)^2 \tag{C.10}$$

where C is in units of farads. Substitution of a typical capacitance value, $C = 10^{-11}$ F, for a small area Ge photodiode at zero bias gives

$$\overline{i_A^2} = 4x10^{-31}(\Delta\nu)^2\text{Amps}^2 \tag{C.11}$$

APPENDIX D

The relationship between the DIAL measurement accuracy and the measurement precision of voltage is presented in this appendix. This relationship is derived from the fundamental DIAL expression, Equation 5.

The derivation proceeds in two steps. In the first step, Equation 5 is inverted to solve for the gas concentration implicit in the absorption coefficient. In the second step, error propagation analysis is applied to the inverted Equation, D.17.

The fundamental expression, Equation 5, is given by

$$P_r(R)=\left(\frac{\beta\Delta R}{4\pi}\right)KP_o\left(\frac{A}{R^2}\right)e^{-2\int_0^R\alpha(r)dr} \tag{D.1}$$

where β = Mie backscatter coefficient, ΔR = sample depth, R = distance to the sample volume center, P_o = power transmitted, P_r = power returned, K = optical system efficiency, A = receiver area, and α = methane absorption coefficient.

As explained in Section 5, the geometrically range resolved DIAL process requires two light pulses each returning light from two locations, at R_1 and R_2, respectively. In what follows, pulse #1 refers to the on absorption line pulse in the DIAL process. Pulse #2 refers to the off line pulse. Also, $R_2-R_1=\Delta R$. For pulse #1:

$$P_{r,on}(R_2)=\frac{\beta_{Mie}(R_2)}{4\pi}K_2A_2P_{o,1}\frac{\Delta R}{R_2^2}\exp\left(-2\bar{\alpha}_{ABS,on,2}R_2\right) \tag{D.2}$$

$$P_{r,on}(R_1)=\frac{\beta_{Mie}(R_1)}{4\pi}K_1A_1P_{o,1}\frac{\Delta R}{R_1^2}\exp\left(-2\bar{\alpha}_{ABS,on,1}R_1\right). \tag{D.3}$$

For pulse #2:

$$P_{r,off}(R_2) = \frac{\beta_{Mie}(R_2)}{4\pi} K_2 A_2 P_{o,2} \frac{\Delta R}{R_2^2} \exp\left(-2\bar{\alpha}_{ABS,off,2} R_2\right) \tag{D.4}$$

$$P_{r,off}(R_1) = \frac{\beta_{Mie}(R_1)}{4\pi} K_1 A_1 P_{o,2} \frac{\Delta R}{R_1^2} \exp\left(-2\bar{\alpha}_{ABS,off,2} R_1\right). \tag{D.5}$$

In Equations D.2 through D.5 the superscript bar indicates the average absorption coefficient over the given range R. Also, $\alpha = \alpha_{ABS}$ as explained in Section 5.

Writing the light powers of the above equations as voltages through the use of square law detectors, the following definitions are made:

$$N_{on} \equiv \ln\left[\frac{V_{r,on}(R_2)}{V_{r,on}(R_1)}\right] \tag{D.6}$$

and

$$N_{off} \equiv \ln\left[\frac{V_{r,off}(R_2)}{V_{r,off}(R_1)}\right] \tag{D.7}$$

As a first step toward inversion of Equations D.2 through D.5, substitution of those equations into D.6 and D.7 and subtraction gives:

$$N_{on} - N_{off} = -2\bar{\alpha}_{ABS,on,2}R_2 + 2\bar{\alpha}_{ABS,on,1}R_1 + 2\bar{\alpha}_{ABS,off,2}R_2 - 2\bar{\alpha}_{ABS,off,1}R_1. \tag{D.8}$$

It is convenient to introduce the following definitions:

$$\bar{\alpha}_{ABS,on,2}R_2 \equiv \bar{\alpha}_{ABS,on,1}R_1 + \bar{\alpha}_{ABS,on}(R_2 - R_1) \tag{D.9}$$

and

$$\bar{\alpha}_{ABS,off,2}R_2 \equiv \bar{\alpha}_{ABS,off,1}R_1 + \bar{\alpha}_{ABS,off}(R_2 - R_1). \tag{D.10}$$

Here $\overline{\alpha}_{ABS,on}$ is the average value of $\alpha_{ABS,on}$ on $\left[R_1,R_2\right]$, and likewise for the off component.

The inversion is then nearly complete with the following observation:

$$N_{on}-N_{off} = 2(R_1-R_2)(\overline{\alpha}_{ABS,on}-\overline{\alpha}_{ABS,off}) \tag{D.11}$$

The absorption coefficients may be written as a product of the average gas concentration and the absorption cross section as follows:

$$\overline{\alpha}_{ABS,on} = \overline{C}\sigma(\lambda_{on}) \tag{D.12}$$

and

$$\overline{\alpha}_{ABS,off} = \overline{C}\sigma(\lambda_{off}) \tag{D.13}$$

where σ is the absorption cross section at wavelength λ and $\overline{C}$ is the average gas concentration on $\left[R_1,R_2\right]$. The average gas concentration may then be written:

$$\overline{C} = \frac{N_{on}-N_{off}}{2(R_1-R_2)[\sigma(\lambda_{on})-\sigma(\lambda_{off})]} \tag{D.14}$$

The inversion of Equation D.1 for the gas concentration is complete with the exception that the two σ variables have yet to be expressed in terms of measurable parameters.

The variables σ_{on} and σ_{off} can be calculated from:

$$T_{on} = \exp\left[-\sigma(\lambda_{on})C'l\right] = \frac{V_{on,2}}{V_{on,1}} \tag{D.15}$$

$$T_{off} = \exp\left[-\sigma(\lambda_{off})C'l\right] = \frac{V_{off,2}}{V_{off,1}} \tag{D.16}$$

where C' is the known gas concentration in a reference cell, $l = r_2 - r_1$, the length of the reference cell, and V_{on} and V_{off} are reference detector voltages. The completed inversion of Equation D.1 is given by:

$$\overline{C} = \frac{C'(r_2-r_1)}{2(R_1-R_2)} \frac{\ln\left(\frac{V_{r,on}(R_2)}{V_{r,on}(R_1)}\right) - \ln\left(\frac{V_{r,off}(R_2)}{V_{r,off}(R_1)}\right)}{\ln\left(\frac{V_{on,1}}{V_{on,2}}\right) - \ln\left(\frac{V_{off,1}}{V_{off,2}}\right)}. \tag{D.17}$$

Error propagation analysis is now applied to the inverted Equation D.17. The analysis is carried out in terms of standard deviations of the various measured voltages and the calculated methane concentration.

The standard deviation in the concentration for uncorrelated voltage fluctuations is given by[199]:

$$\sigma_{\overline{C}} = \left[\sum_{i=1}^{8}\left(\frac{\partial \overline{C}}{\partial V_i} V_i \frac{\sigma_{V_i}}{V_i}\right)^2\right]^{1/2} \tag{D.18}$$

where σ_x represents the standard deviation in x. The partial derivative factors in D.18 may be written:

$$\left|\frac{\partial \overline{C}}{\partial V_i}\right| = \left|\kappa \frac{1}{V_i}\right| \tag{D.19}$$

where κ is given by:

$$\kappa = \pm \frac{C'(r_2-r_1)}{2(R_1-R_2)} \frac{1}{\ln\left(\frac{V_{on,1}}{V_{on,2}}\right) - \ln\left(\frac{V_{off,1}}{V_{off,2}}\right)} \tag{D.20}$$

for the returned signal voltages, V_r, and

$$\left|\frac{\partial C}{\partial V_i}\right| = \left|\kappa' \frac{1}{V_i}\right| \tag{D.21}$$

where κ' is given by:

$$\kappa' = \pm\frac{C'(r_2-r_1)}{2(R_1-R_2)}\,\frac{\ln\left(\frac{V_{r,on}(R_2)}{V_{r,on}(R_1)}\right)-\ln\left(\frac{V_{r,off}(R_2)}{V_{r,off}(R_1)}\right)}{\left[\ln\left(\frac{V_{on,1}}{V_{on,2}}\right)-\ln\left(\frac{V_{off,1}}{V_{off,2}}\right)\right]^2} \tag{D.22}$$

for the references voltages.

The assumption is made that equal signal to noise ratios can be achieved for each measured return voltage. That is, assume:

$$\left(\frac{\sigma_V}{V}\right)_i=\left(\frac{\sigma_V}{V}\right)_j\equiv\frac{\sigma_V}{V} \tag{D.23}$$

for all i and j for the returned signals. Also it is assumed that the reference signal to noise ratios are much greater than the returned signal ratios due to the larger optical power available to the reference detectors. If the reference cell gas concentration is adjusted to obtain the absorption typically found in the remote sample volume (ie. population distribution of absorbing molecules and pressure broadened linewidths are the same)[135], the following approximations can be made:

$$\ln\left[\frac{V_{r,on}(R_2)}{V_{r,on}(R_1)}\right]\approx\ln\left[\frac{V_{on,1}}{V_{on,2}}\right]\ \text{and}\ \ln\left[\frac{V_{r,}\mathrm{off}(R_2)}{V_{r,off}(R_1)}\right]\approx\ln\left[\frac{V_{off,1}}{V_{off,2}}\right] \tag{D.24}$$

Equation D.24 implies $\kappa \approx \kappa'$.

Substitution of D.23 into D.18 then gives:

$$\sigma_{\overline{C}} = \frac{2\sigma_V |\kappa|}{V} \tag{D.25}$$

where the κ' term is removed because of the large reference signal to noise ratios. Substitution of Equation D.20 into Equation D.25 divided by Equation D.17 yields:

$$\frac{\sigma_{\overline{C}}}{\overline{C}} = 2\frac{\sigma_V}{V} \left| \ln\left(\frac{V_{r,on}(R_2)}{V_{r,on}(R_1)}\right) - \ln\left(\frac{V_{r,off}(R_2)}{V_{r,off}(R_1)}\right) \right| \tag{D.26}$$

Since the absorption cross section is small in the off line portion of the DIAL process, simplifications can be made to Equation D.26. Specifically, the small amount of absorption implies:

$$\frac{V_{r,off}(R_2)}{V_{r,off}(R_1)} \approx 1 \tag{D.27}$$

Finally, substitution of Equation D.27 into Equation D.26 gives a simple expression for the maximum allowable normalized standard deviation in the measured voltages as a function of the required gas concentration measurement accuracy and the amount of absorption in the sample volume during the on line portion of the DIAL process:

$$\frac{\sigma_V}{V} = \frac{1}{2}\,\frac{\sigma_{\overline{C}}}{\overline{C}} \left| \ln\left(\frac{V_{r,on}(R_2)}{V_{r,on}(R_1)}\right) \right|. \tag{D.28}$$

APPENDIX E

This appendix presents a derivation of the spectral bandwidth for the off-axis parabolic mirror/grating diode laser cavity used in this project. This derivation uses, as was mentioned in Section 6.2., coupled mode theory as its basis.

Figure E.1 shows schematically an external grating diode laser cavity. The spatial dependence perpendicular to the diode active region of the laser waveguide circulating mode and the optical mode incident on the laser facet may be written, respectively, as:

$$\Psi_L(z=0) = A \exp\left[\frac{-x^2}{\omega_o^2}\right] \tag{E.1}$$

and

$$\Psi_I(z=0) = A' \exp\left[\frac{-(x-a)^2}{(\beta\omega_o)^2}\right] \tag{E.2}$$

where ω_o is the spotsize of the waveguide circulating mode in the diode laser, β is the ratio of the spotsize of the incident wave to that of the guided wave, a is the relative displacement in the x direction of the two spots, and A and A′ are proportionality constants.

The coupling efficiency between the guided and incident modes is given by[166, 167]

$$\eta = \frac{\left|\int_{-\infty}^{\infty} \Psi_L \Psi_I^*\right|^2}{\int_{-\infty}^{\infty} \Psi_L \Psi_L^* dx \int_{-\infty}^{\infty} \Psi_I \Psi_I^* dx}. \tag{E.3}$$

This implies by substitution that η may be written as

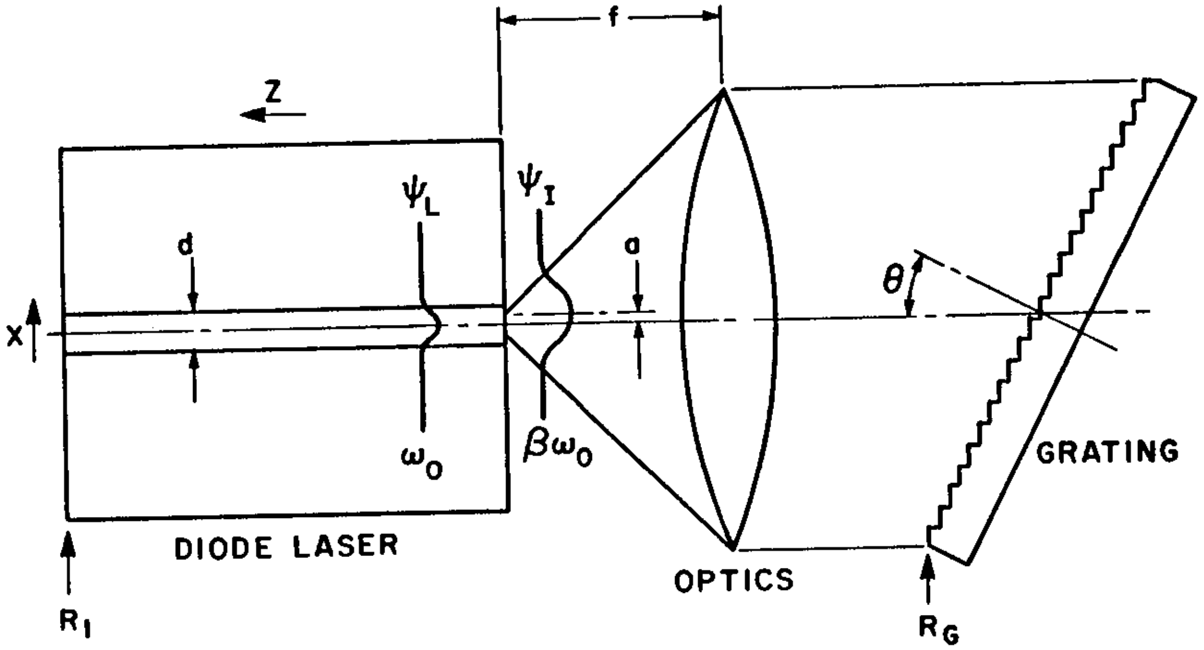

Figure 37. Schematic representation of the dual diode laser cavity showing the diode laser circulating guided wave and the grating returned optical mode.

Evaluation of the integrals in Equation E.4 leads to the following expression for η

$$\eta(a,\beta) = \frac{2\beta}{\beta^2+1} \exp\left[\frac{-2a^2}{\omega_o^2\left(\beta^2+1\right)}\right] \tag{E.5}$$

In Figure E.1, $2a = f\Delta\theta$ where f is the focal length of the focussing optics and where $\Delta\theta$ is the full width angular deviation of the grating fedback light from the center wavelength. Substitution of Equation E.5 into the fundamental dispersion relation for a Littrow mounted grating[185]

$$\Delta\theta = \frac{2\tan(\theta)\,\Delta\lambda}{\lambda} \tag{E.6}$$

yields

$$\eta = \frac{2\beta}{\beta^2+1} \exp\left[\frac{-2\left(f\tan(\theta)\,\Delta\lambda\right)^2}{\lambda^2\omega_o^2\left(\beta^2+1\right)}\right] \tag{E.7}$$

It is known that[64]

$$I_{th} \propto \alpha + \frac{1}{2L}\ln\left(\frac{1}{R_1 R_G}\right) \tag{E.8}$$

where I_{th} is the laser threshold current, α represents the laser internal losses including the loss associated with the current required to achieve zero gain, and L is the laser length, R_1 is the laser output facet power reflectivity and R_G is the effective grating reflectivity.

R_G may be expressed as:

$$R_G = R_m^2\,\epsilon\,\eta \tag{E.9}$$

where R_m is the mirror reflectivity ≈ 0.95, and ϵ is the Littrow mount grating efficiency

R_G may be expressed as:

$$R_G = R_m^2 \epsilon \eta \tag{E.9}$$

where R_m is the mirror reflectivity ≈ 0.95, and ϵ is the Littrow mount grating efficiency ≈ 0.70. Both R_m and ϵ are nearly independent of wavelength on the scale of the present discussion. Let the following definitions be made:

$$I_o \equiv I_{th}(\lambda=\lambda_o) \tag{E.10}$$

$$I_{\Delta\lambda} \equiv I_{th}\left(\lambda=\lambda_o \pm \frac{\Delta\lambda}{2}\right) \tag{E.11}$$

$$Z_{\Delta\lambda} \equiv \frac{I_o}{I_{\Delta\lambda}} \tag{E.12}$$

which implies that

$$Z_{\Delta\lambda} = \frac{\alpha + \frac{1}{2L}\ln\left(\frac{1}{R_1 R_m^2 \epsilon \eta_o}\right)}{\alpha + \frac{1}{2L}\ln\left(\frac{1}{R_1 R_m^2 \epsilon \eta_{\Delta\lambda}}\right)} \tag{E.13}$$

where η_o is $\eta(\lambda_o)$ and $\eta_{\Delta\lambda}$ is $\eta(\lambda=\lambda_o \pm \frac{\Delta\lambda}{2})$.

Let R' be the current overdrive:

$$R' = \frac{I}{I_o} \tag{E.14}$$

where I is the diode laser drive current. Then if $R' > \frac{1}{Z_{\Delta\lambda}}$ the laser oscillator modes at $\lambda_o \pm \frac{\Delta\lambda}{2}$ will be above lasing threshold and, conversely, if $R' < \frac{1}{Z_{\Delta\lambda}}$ those modes will be below threshold.

The optical power emitted into a mode near $\lambda_o \pm \frac{\Delta\lambda}{2}$ is then given by

$$P_{\Delta\lambda} = \eta_D \left[\frac{I}{I_{th}} - \frac{1}{Z_{\Delta\lambda}} \right] I_{th} \qquad \text{(E.15)}$$

where η_D is the laser external differential quantum efficiency and where the term in brackets must be non-negative to be meaningful. In the case that $Z_{\Delta\lambda}=1$ (ie. $R_{\Delta\lambda}=R_o$ or $\Delta\lambda=0$) it may be seen that Equation E.15 reduces to the standard formula for output versus drive current:

$$P = \eta_D (I - I_{th}) \qquad \text{(E.16)}$$

Substitution yields:

$$P_{\Delta\lambda} = \eta_D (R' - \frac{1}{Z_{\Delta\lambda}}) I_{th} \qquad \text{(E.17)}$$

To find the spectral width (FWHM), $\Delta\lambda_{\frac{1}{2}}$, of the optical power, let

$$P(Z_{\Delta\lambda_{\frac{1}{2}}}) = \frac{1}{2} P(Z_{\Delta\lambda}=1) \qquad \text{(E.18)}$$

Define

$$Z_{\Delta\lambda_{\frac{1}{2}}} = Z' \qquad \text{(E.19)}$$

Substitution of Equation E.19 into Equation E.18 and evaluation gives:

$$Z' = \frac{2}{R'+1} \qquad \text{(E.20)}$$

and

$$\eta_{\Delta\lambda_{\frac{1}{2}}} = \frac{1}{\mathrm{R_1 R_m^2}\epsilon}\exp\left[-2\mathrm{L}\left[\left(\alpha+\frac{1}{2\mathrm{L}}\ln\left(\frac{1}{\mathrm{R_1R_m^2}\epsilon\eta_o}\right)\right)\frac{\mathrm{R'}+1}{2}-\alpha\right]\right]. \tag{E.21}$$

Setting the right sides Equations E.21 and E.7 equal then allows for solution for $\Delta\lambda_{\frac{1}{2}}$.

$$\Delta\lambda_{\frac{1}{2}} = \frac{\lambda\omega_o\left(\beta^2+1\right)^{\frac{1}{2}}}{\mathrm{f}\tan(\theta)}\left[\left(\mathrm{L}\alpha+\frac{1}{2}\ln\left(\frac{1}{\mathrm{R_1R_m^2}\epsilon\eta_o}\right)\right)\frac{\mathrm{R'}+1}{2}-\mathrm{L}\alpha-\frac{\gamma}{2}\right]^{\frac{1}{2}} \tag{E.22}$$

where γ is given by

$$\gamma = \ln\left(\frac{\beta^2+1}{2\beta\mathrm{R_1R_m^2}\epsilon}\right) \tag{E.23}$$

Several numerical values are needed for the evaluation of Equation E.22. ω_o is calculated with use of the fundamental eigenvalue equation [95] for TM modes in a symmetric waveguide:

$$\tan\left(\frac{\kappa\mathrm{d}}{2}\right)=\frac{\mathrm{n_2^2}\Gamma}{\mathrm{n_1^2}\kappa} \tag{E.24}$$

where κ is the complex waveguide propagation constant, d is the active region thickness, n_2 is the active region index of refraction, where Γ is given by

$$\Gamma^2 = \chi^2-\mathrm{n_1^2k_o^2} \tag{E.25}$$

and where n_1 is the waveguide cladding layer index of refraction, χ is $\frac{2\pi}{\lambda}$ in the waveguide, and k_o is given by

$$\mathrm{k_o} = 2\frac{\pi}{\lambda_o} \tag{E.26}$$

where λ_o is the free-space lasing wavelength. Numerical solution of the transcendental equation E.24 gives $\omega_o = 0.2\mu m$. A diffraction-limited spotsize for the off-axis parabolic mirror used in the present project may be calculated to be $\approx 0.9\mu m$. Thus, β is ≈ 4.5.

Numerical values for the various parameters of Equation E.22 are as follows:

$\lambda = 1.65\mu m$,

$\omega_o = 0.2\mu m$,

$\beta = 4.5$,

$f = 35mm$,

$\tan(\theta) = 0.56$,

$L = 400\mu m$,

$R_1 = 0.26$,

$R_m = 0.95$,

$\epsilon = 0.70$,

$\eta_o = \frac{2\beta}{\left(\beta^2+1\right)} = 0.42$,

$\gamma = 2.6$,

$\alpha \approx 100\ cm^{-1}$,

and

$R' = 2$ to 3.

Substitution into Equation E.22 gives a numerical value

$\Delta\lambda_{\frac{1}{2}} = 1.0$ to 1.5 Angstroms.

APPENDIX F

This appendix is a source listing of the Basic language source program CAVITY. The program is a ray-trace and spot diagram tool for the external grating off-axis parabolic mirror diode laser cavity. The uses of the program are explained in Section 6.

```
 1  DEFINE FILE #4='X', ASC SEP          PAGE 0001


 1  DEFINE FILE #4='X', ASC SEP
 2  DEFINE FILE #5='Y', ASC SEP
 3  DEFINE FILE #6='Z', ASC SEP
 4  DIM M(100)
 5  B$='YES'
 6  K=3.1415926536/180
 8  Q=0
 9  DEFINE FILE #3='IMAGE', ASC SEP
10  DEFINE FILE #1='RATRAS', ASC SEP
11  DEFINE FILE #2='SPOTSZ'
12  PRINT 'INPUT TILT OF LASER TO Z AXIS <90DEGREES'
13  INPUT H3
14  PRINT 'INPUT MAX. ANGLE SEPARATION OF RAYS (DEGREES) PER. AND'
15  PRINT ' PARALLEL TO ACTIVE REGION'
16  INPUT H4,H5
18  PRINT ' DO YOU WANT RAYS DRAWN'
19  INPUT A$
20  PRINT 'DO YOU WISH RANDOM RAYS FOR 100 RAYS'
21  INPUT D$
22  PRINT 'DO YOU WISH WIDEST RAYS DRAWN'
23  INPUT G$
24  IF D$<>'YES' THEN 70
25  DEFINE FILE #7='SPOTSTAT', ASC SEP
26  PRINT 'INPUT NUMBER OF PREVIOUS SPOTSTAT POINTS TO BE BYPASSED'
27  U9=20.61
 8  U8=28.88
29  INPUT R
30  REM CONSTANTS FOR GAUSSIAN IMPROVEMENT ROUTINE-ABRAMOWITZ
31  REM AND STEGUN PAGE 953 CORRECTED
32  A(0)=.98746
33  A(2)=.0039439
34  A(4)=7.474E-05
35  A(6)=-5.102E-07
36  A(8)=1.141E-07
37  P1=3.14159
40  GOTO 105
70  PRINT 'DO YOU WISH AUTOMATIC ANGLE READING FOR START PT.'
71  INPUT F$
72  IF F$<>'YES' THEN 105
73  PRINT 'INPUT NUMBER OF ANGLES TO BE READ'
74  INPUT J
105  PRINT 'INPUT PARABOLA FOCAL LENGTH IN MM.'
106  INPUT F
107  REM G1 IS GAUSSIAN VARIABLE COUNTER
108  G1=1
112  PRINT 'INPUT Z COORDINATE OF GRATING'
113  INPUT Z9
114  L=0
115  PRINT 'INPUT Y0,Z0 START PTS. WITH FOCUS AT (0,0,F)'
116  INPUT Y0,Z0
  5  PRINT 'INPUT X COORDINATE OF LASER FACET'
  6  INPUT W7
130  X0=TAN(K*(-H3))*(Z0-F)+W7
131  IF D$='YES' THEN 191
150  IF B$<>'YES' THEN 205
180  REM
```

```
  1  DEFINE FILE #4='X', ASC SEP          PAGE 0002


181  REM
182  REM FIND LINE 1
183  REM E0 IS END VALUE OF T
184  REM A8,B8,C8 ARE DIRECTION COSINES FOR LINE 1
189  IF F$<>'YES' THEN 201
190  GOTO 193
191  GOSUB 5000
192  GOTO 204
193  READ H1,H2
194  GOTO 204
201  PRINT 'INPUT INITIAL RAY DIVERGENCE FROM FACET NORMAL'
202  PRINT 'PERPENDICULAR, PARALLEL TO ACT. REGION DEGREES'
203  INPUT H1,H2
204  GOSUB 3500
205  A=A8
206  B=B8
207  C=C8
208  X=X0
209  Y=Y0
210  Z=Z0
211  GOSUB 4000
212  E0=E
213  A0=A8
214  B0=B8
215  C0=C8
[illegible]7  IF A$<>'YES' THEN 240
220  FOR T0=0,E0,E0/100
225  U=X+T0*A
226  V=Y+T0*B
227  W=Z+T0*C
228  GOSUB 6000
235  NEXT T0
240  U=X+E0*A
241  V=Y+E0*B
242  W=Z+E0*C
298  REM
299  REM
300  REM FIND LINE 2
301  REM E1 IS END VALUE OF T
302  REM A1,B1,C1 ARE DIRECTION COSINES
310  X=U
311  Y=V
312  Z=W
320  S0=2*SQR(F*Z+F^2)
322  N1=X/S0
323  N2=Y/S0
324  N3=-2*F/S0
330  A=A8
331  B=B8
332  C=C8
[illegible]  GOSUB 4500
342  A1=A9
344  B1=B9
346  C1=C9
348  E1=(Z9-Z)/C1
355  IF A$<>'YES' THEN 390
```

```
1  DEFINE FILE #4='X', ASC SEP          PAGE 0003

360  FOR T1=0,E1,E1/100
370  U=X+T1*A1
371  V=Y+T1*B1
372  W=Z+T1*C1
373  GOSUB 6000
380  NEXT T1
390  U=X+E1*A1
391  V=Y+E1*B1
392  W=Z+E1*C1
498  REM
499  REM
500  REM FIND LINE 3
501  REM E2 IS END VALUE OF T
502  REM A2,B2,C2 ARE DIRECTION COSINES
510  X=U
511  Y=V
512  Z=W
520  A=A1
521  B=B1
522  C=-C1
525  GOSUB 4000
530  X2=X
536  E2=E
540  IF A$<>'YES' THEN 580
550  FOR T2=0,E2,E2/100
 .0  U=X+T2*A
561  V=Y+T2*B
562  W=Z+T2*C
563  GOSUB 6000
570  NEXT T2
580  U=X+E2*A
581  V=Y+E2*B
582  W=Z+E2*C
698  REM
699  REM
700  REM FIND LINE 4
701  REM E3 IS END VALUE FOR T
702  REM A3,B3,C3 ARE DIRECTION COSINES
710  X=U
711  Y=V
712  Z=W
730  S0=2*SQR(F*Z+F^2)
740  N1=X/S0
741  N2=Y/S0
742  N3=-2*F/S0
750  GOSUB 4500
760  A3=A9
761  B3=B9
762  C3=C9
765  E3=(TAN(K*(-N3))*(Z-F)-X)/(A3-TAN(K*(-N3))*C3)
 .7  IF A$<>'YES' THEN 800
,70  FOR T3=0,E3,E3/100
780  U=X+T3*A3
781  V=Y+T3*B3
782  W=Z+T3*C3
783  GOSUB 6000
```

```
  1  DEFINE FILE #4='X', ASC SEP          PAGE 0004


  .0  NEXT T3
 800  U=X+E3*A3
 801  V=Y+E3*B3
 802  W=Z+E3*C3
 897  REM
 898  REM FINAL PTS IN LASER FACET PLANE
 899  REM
 900  X4=U
 901  Y4=V
 902  Z4=W
 999  IF D$='YES' THEN 1010
1000  PRINT X0,Y0,Z0
1001  PRINT X4,Y4,Z4
1002  PRINT
1010  WRITE #2,X0,Y0,Z0,A0,B0,C0
1011  WRITE #2,X4,Y4,Z4
1020  WRITE #3,1000*(Z4-F)/COS(K*H3),Y4*1000
1022  IF D$='YES' THEN 191
1030  IF F$='YES' THEN 6500
1050  PRINT ' DO YOU WISH NEW ANGLES'
1051  INPUT B$
1060  PRINT ' DO YOU WISH NEW STARTING PT.'
1061  INPUT C$
1070  IF B$='YES' THEN  IF C$='YES' THEN 115
1080  IF B$='YES' THEN  IF C$<>'YES' THEN 201
1  2  IF C$='YES' THEN 115
1500  IF A$<>'YES' THEN 9999
1507  GOSUB 6000
1520  REM
1521  REM
1522  REM CALCULATE LINES FOR WIDEST RAYS IN X,Z PLANE
1523  REM STARTING AT FOCUS,
1524  REM
1530  X0=0
1531  Y0=0
1532  Z0=F
1540  H1=H4
1541  IF Q>1.5 THEN 1700
1542  H2=H5
1550  GOSUB 3500
1555  X=X0
1556  Y=Y0
1557  Z=Z0
1558  A=A8
1559  B=B8
1560  C=C8
1570  GOSUB 4000
1585  FOR T4=0,E,E/100
1600  U=X+T4*A
1601  V=Y+T4*B
1602  W=Z+T4*C
1.  3  IF C$<>'YES' THEN 1610
1604  IF D$='YES' THEN 1610
1605  GOSUB 6000
1610  NEXT T4
1612  IF Q<.5 THEN 1620
```

```
613  X6=U
614  Y6=V
615  Z6=W
616  GOTO 1630
620  X5=U
621  Y5=V
622  Z5=W
630  H1=-H4
635  Q=Q+1
640  GOTO 1541
700  REM
701  REM
702  REM CALC. PTS ON PARABOLA BETWEEN EXTREME RAYS IN
703  REM XZ PLANE
704  REM
1710  FOR T=1.1*X5,.9*X6,(.9*X6-1.1*X5)/100
1720  W=T^2/(4*F)
725  U=T
1726  V=0
1727  GOSUB 6000
1730  NEXT T
1800  REM
1801  REM
1802  REM CALCULATE PTS. ON GRATING
1803  REM
1820  FOR T=X5,X6,(X6-X5)/100
1830  W=Z9
1831  V=0
1840  U=T
1841  GOSUB 6000
1850  NEXT T
1900  GOTO 7000
3490  REM
3491  REM
3492  REM
3493  REM MISC. ROUTINES
3494  REM
3495  REM
3496  REM
3498  REM
3499  REM
3500  REM CALCULATE INITIAL DIRECTION COSINES
3501  REM
3520  H3=H3*K
3530  H1=H1*K
3540  H2=H2*K
3550  A8=COS(H1)*COS(H2)*COS(H3)-SIN(H1)*SIN(H3)
3560  B8=COS(H1)*SIN(H2)
3570  C8=COS(H1)*COS(H2)*SIN(H3)+SIN(H1)*COS(H3)
3575  H1=H1/K
3580  H2=H2/K
3585  H3=H3/K
3600  RETURN
3998  REM
3999  REM
4000  REM FIND END PT. FOR T WHEN APPROACHING PARABOLA
```

```
   1  DEFINE FILE #4='X', ASC SEP          PAGE 0006

4001  REM
4002  IF A^2+B^2)F/10000 THEN 4010
4003  E=(X^2+Y^2)/(4*F*C)-Z*C
4004  GOTO 4060
4010  S0=A^2+B^2
4020  S1=2*F*C-B*Y-A*X
4030  S2=S1^2
4040  S3=S0*(X^2+Y^2-4*F*Z)
4050  E=(S1+SQR(S2-S3))/S0
4060  RETURN
4498  REM
4499  REM
4500  REM CALCULATE DIRECTION COSINES AFTER PARABOLA
4501  REM
4510  A9=(1-2*H1^2)*A-2*H1*H2*B-2*H1*H3*C
4520  B9=-2*H1*H2*A+(1-2*H2^2)*B-2*H2*H3*C
4530  C9=-2*H1*H3*A-2*H2*H3*B+(1-2*H3^2)*C
4600  RETURN
4998  REM
4999  REM
5000  REM ROUTINE TO GENERATE 100 GAUSSIAN RANDOM INIT ANGLES
5001  REM
5100  IF G1)100 THEN 1520
5300  U1=RND(J)
5310  U2=RND(J)
5320  U3=(-2*LOG(U1))^.5*COS(2*P1*U2)
5330  U4=(-2*LOG(U1))^.5*SIN(2*P1*U2)
5340  H1=0
5350  H2=0
5399  REM LOOP FOR IMPROVEMENT ROUTINE
5400  FOR K9=0,8,2
5410  H1=H1+A(K9)*U3^K9
5420  H2=H2+A(K9)*U4^K9
5430  NEXT K9
5440  H1=H1*U3*U8
5450  H2=H2*U4*U9
5454  REM CHECK IF INITIAL GAUSSIAN ANGLE FALLS ON MIRROR
5455  IF ABS(H1))ABS(H4) THEN 5300
5456  IF ABS(H2))ABS(H5) THEN 5300
5800  G1=G1+1
5900  RETURN
5998  REM
5999  REM
6000  REM ROUTINE FOR LINE DRAWING ITERATION
6002  REM
6003  WRITE #4,U
6004  WRITE #5,V
6005  WRITE #6,W
6006  L=L+1
6007  RETURN
6500  REM
6501  REM
6502  REM ROUTINE TO READ ANGLES AUTOMATICALLY
6503  REM
6510  J=J-1
6515  IF J=0 THEN 1100
```

```
   1  DEFINE FILE #4='X', ASC SEP          PAGE 0007


6 20  GOTO 193
7000  REM
7001  REM
7002  REM CREATE FILE WITH X,Z PTS. FOR GRAPHICS
7003  REM
7025  REWIND #4
7026  REWIND #5
7027  REWIND #6
7028  FOR T=1,L
7029  READ #4,U
7035  READ #6,W
7040  WRITE #1,W,U
7045  NEXT T
7099  IF D$<>'YES' THEN 9999
8000  REM
8001  REM
8002  REM ROUTINE TO CALCULATE THE STANDARD DEVIATION AND FULL
8003  REM WIDTH HALF MAXIMUM (FWHM) SIZE OF THE RETURNED SPOT IF
8004  REM RANDOM (GAUSSIAN DENSITY) INITIAL ANGLES ARE USED
8005  REM
8006  REM
8009  N=100
8010  REWIND #3
8020  S6=0
8021  S7=0
   2  S8=0
8023  S9=0
8030  FOR I=1,N
8040  READ #3,X,Y
8050  S6=S6+X
8060  S7=S7+X^2
8070  S8=S8+Y
8080  S9=S9+Y^2
8090  NEXT I
8099  REM CALCULATE STANDARD DEVIATION IN VARIATES X,Y
8100  X1=SQR(N*S7-S6^2)/N
8110  X2=SQR(N*S9-S8^2)/N
8120  REM CONVERT S.D. TO FWHM DIAMETERS ASSUMING GAUSSIAN DIST.
8130  X1=X1*2*SQR(-2*LOG(.5))
8140  X2=X2*2*SQR(-2*LOG(.5))
8150  PRINT ' FWHM SPOT SIZE PERP. TO JUNCTION IN MICRONS'
8160  PRINT X1
8170  PRINT ' FWHM SPOT SIZE PARALLEL TO JUNCTION IN MICRONS'
8180  PRINT X2
8190  FOR I=1,2*R
8191  IF R=0 THEN 8210
8200  READ #7,R9
8210  NEXT I
8250  WRITE #7,W7,X1
8260  WRITE #7,W7,X2
•  0  DATA -35,0,-25,0,-15,0,0,0,15,0,25,0,35,0
..01  DATA -35,-20,-25,-20,-15,-20,0,-20,15,-20,25,-20,35,-20
9502  DATA -35,20,-25,20,-15,20,0,20,15,20,25,20,35,20
9999  END
```